Stampa (in PDF) del frontespizio elettronico della tesi

URN	etd-02212022-164216
Author (university registration number)	BRUNI, REBECCA (588745)
email address	r.bruni2@studenti.unipi.it, rebecca.bruni1@gmail.com
Department	GEO/10
Course of study	SCIENZE DELLA TERRA
Supervisor	Dott. Saccorotti, Gilberto - tutor Prof. Boswell Keir, Derek - correlatore Prof. Sani, Federico - correlatore
Thesis type	Tesi di dottorato di ricerca
Thesis title	Analysis of the seismicity in the Mugello basin and nearby areas
Submission start date	21/02/2022

Dichiarazione del tutor

Attesto che la tesi è stata da me giudicata idonea alla discussione per l'esame di dottorato.

Firma leggibile del tutor

Saccorotti, Gilberto

Dichiarazione del candidato

Attesto che la stampa del frontespizio elettronico è conforme a quello creato in ETD.

Firma leggibile del candidato

BRUNI, REBECCA Rebecca Bruni

Consultability

By choice of the candidate, the ETD thesis will be freely available after 3 years from the date of the discussion for the following reason:

publication of the thesis or parts of it

The candidate's signature is not required.*

BRUNI, REBECCA Rebecca Bruni

For validation, pursuant to art. 1 paragraph 5 of the Regulations for electronic theses.

Legible signature of the tutor

Saccorotti, Gilberto

Abstract

Within the geodynamic context of the Northern Apennines (Italy), a relevant seismogenic area is the Mugello basin (North-Eastern Tuscany). The area has a well-documented record of seismicity; the two major historical earthquakes occurred in 1542 (Mw=6.0) and in 1919 (Mw=6.4). The proximity of the Mugello Basin to densely-urbanized areas and the potential impact of strong earthquakes on the cultural heritage in the nearby (~30km) city of Florence makes a better knowledge of the seismicity in that area an important target. Within this context, one unresolved issue concerns the exact location and geometry of the major seismogenic fault(s) that rupture with larger earthquakes. The present-day seismicity in the region is characterized by short-duration sequences, exhibiting a clear mainshock-aftershock behaviour. Their accurate study is particularly relevant since it may provide constraints on fault location, geometry and kinematics, which are necessary ingredients for seismic hazard assessment. To address these topics, I integrated all the available seismic catalogs for the area, obtaining more than 12000 earthquakes spanning the 2005-2019 time interval in a single catalog. Then, I participated to the installation of 9 temporary stations that complemented the permanent seismic recording network in the area in the period spanning 2019-2021. From integration of both archive (for the period 2005-2019) and newly-acquired (2019) sets of phase arrival times I obtained an improved seismic catalog, which have been inverted for hypocentral location using a specific velocity model. The subsequent relocation with a double-difference algorithm (HypoDD) of this data set allowed for accurate analyses of the most relevant seismic sequences which affected the study area in March 2008, September 2009, 2015-2017 and December 2019. These sequences are associated with the activation of adjacent segments of a larger NW-striking fault system. These results show that the present-day seismicity is driven by the fault system bordering the NE margin of the basin (Ronta fault system). The temporary network provided high-quality recordings of the 2019 sequence which, coupled to advanced detection methods (e.g. Matched Filter technique), permitted improving the catalog completeness by a factor greater than 3 in the number of locations, and a decrease of 1.2 in magnitude of completeness. Finally, the arrival times of local earthquakes from the merged catalog have been inverted to derive a 3D seismic velocity model for the Northern Apennines crust. The model broadly has seismic velocities within the range expected for continental crust, except for shallow high P-wave velocity lobes in the upper crust near to and striking parallel to the Apennines, which likely correspond with crystalline basement at the core of major anticlines associated with the Apennines thrust system. The images also show a distinctive, deeper increase of seismic velocity consistent with the base of the crust, which deepens from ~20-25 km to ~30 km beneath the Apennines, thus confirming local crustal thickening beneath the belt.

Nel contesto geodinamico dell'Appennino Settentrionale (Italia), un'area sismogenica rilevante è il bacino del Mugello (Toscana nord-orientale). L'area ha una storia sismica ben documentata; i due maggiori terremoti storici si sono verificati nel 1542 (Mw = 6.0) e nel 1919 (Mw = 6.4). La vicinanza del Bacino del Mugello ad aree densamente urbanizzate e il potenziale impatto di forti terremoti sul patrimonio culturale nella vicina (~ 30 km) città di Firenze rende una migliore conoscenza della sismicità in quest'area un obiettivo importante. Un problema irrisolto riguarda la posizione esatta e la geometria del sistema di faglie sismogeniche responsabili dei terremoti maggiori. La sismicità recente ed attuale è caratterizzata da sequenze di breve durata, che mostrano un chiaro comportamento di scossa principale (*mainshock*) e successive scosse di assestamento (*aftershocks*). Lo studio accurato di queste sequenze è particolarmente rilevante poiché contribuisce a definire la posizione, la geometria e la cinematica del sistema di faglie, tutti elementi necessari per la valutazione della pericolosità sismica. Per affrontare questi temi, in questo lavoro di tesi ho integrato tutti i cataloghi sismici disponibili per l'area di studio, raccogliendo in un unico catalogo i dati parametrici di più di 12000 terremoti nell'intervallo di tempo 2005-2019. Inoltre, ho partecipato all'installazione ed alla manutenzione di 9 stazioni sismiche temporanee che, per il periodo 2019-2021, hanno integrato la rete di monitoraggio sismico per l'area circostante il bacino del Mugello. Dall'integrazione dei tempi di arrivo delle fasi di archivio (per il periodo 2005-2019) e quelle di nuova acquisizione (2019) ho ottenuto un catalogo sismico aggiornato, che è stato localizzato utilizzando un modello di velocità specifico. La rilocalizzazione con l'algoritmo delle doppie differenze (HypoDD) di questo data set ha permesso di analizzare nel dettaglio le sequenze sismiche più rilevanti che hanno interessato l'area di studio nel marzo 2008, settembre 2009, 2015-2017 e dicembre 2019. Tali sequenze sono associate all'attivazione di segmenti adiacenti di un più ampio sistema di faglie orientato NO-SE. Questi risultati indicano che la sismicità attuale è associata al sistema di faglie che delimitano il margine Nord-Orientale del bacino (sistema di faglie di Ronta). La rete temporanea ha fornito registrazioni ad elevato rapporto segnale-rumore della sequenza del 2019, avvenuta al margine nord-occidentale del bacino. A questi dati è stato applicato un metodo di rilevazione avanzato (tecnica del Matched Filter), che ha portato a migliorare la completezza del catalogo di un fattore maggiore di 3 per il numero di terremoti, e un fattore 1.2 della magnitudo di completezza. Infine, i tempi di arrivo dei terremoti locali del dataset integrato sono stati invertiti per derivare un nuovo modello di velocità sismica 3D per la crosta dell'Appennino settentrionale. Il modello mostra velocità sismiche all'interno dell'intervallo previsto per la crosta continentale, ad eccezione di 2 anomalie positive nella velocità delle onde P, ubicate nella crosta superiore in corrispondenza della catena Appenninica, che probabilmente corrispondono al basamento cristallino al nucleo delle principali anticlinali associate al sistema di thrust Appenninico. Nella sua parte più profonda, il modello mostra un aumento della velocità coerente con la base della crosta, che si approfondisce da ~20-25 km a ~30 km sotto gli Appennini, confermando così l'ispessimento crostale al di sotto della catena già ipotizzato da studi precedenti.

Contents

Contents 3
Chapter 1 1
Introduction and Geological setting 1
1.1 Objectives of the thesis 1
1.2 Geological setting 2
1.3 Historical and instrumental seismicity of the Mugello area 5
Chapter 2 8
Archive data 8
2.1 Introduction 8
2.2 Data 9
2.2.1 The INGV Catalog 10
2.2.2 The RSTNO Catalog 12
2.3 Method 14
2.4 Results 15
2.5 Conclusions 18
Chapter 3 20
Temporary network, the 9M Mugello Temporary Seismic Deployment (MULTIPLY) network 20
3.1 Introduction 20
3.2 Site selection 20
3.2.1 Procedure of the scouting survey 21
3.3 Installation of seismic stations 23
3.3.1 Instrumental characteristics and data 25
3.3.2 Network performance 27
3.4 Conclusions 29
Chapter 4 30
Local Earthquake Tomography 30
4.1 Introduction 30
4.2 Starting 1D velocity model 30
4.2.1 Data 30
4.2.2 Method 33
4.2.3 Results 34
4.3 Local Earthquake Tomography (LET) 35
4.3.1 Data and input starting velocity model 36
4.3.2 Method 38

4.3.3 Results 40
4.4 3D Tomographic Inversion of real data 46
4.5 Interpretation 52
4.6 Conclusions 54
Chapter 5 55
Seismic Sequences 55
5.1 Introduction 55
5.2 Seismicity over the 2005-2021 time interval 56
5.2.1 The INGV Catalog 56
5.2.2 The seismic sequences from the integrated catalogs 58
5.2.3 Relocations, focal mechanisms and fault planes 59
5.3 Focus on the 2019 sequence 65
5.3.1 Improvement of catalog completeness using Matched Filter 70
5.3.2 Results 72
5.4 Conclusions 75
Chapter 6 77
Conclusions 77
Aknowledgments 79
Bibliography 80
Supplementary materials 88
1. Station datasheets 88
2. Space-Time evolution of the sequences 108

Chapter 1

Introduction and Geological setting

1.1 Objectives of the thesis

The region around the Mugello basin (Northern Tuscany) represents an important seismogenic area of the Northern Apennines. Large historical earthquakes have occurred, such as the Mw=6.0, 1542 and the Mw=6.4, 1919 events (Rovida et al., 2016). Its proximity to densely-urbanized areas and the potential impact of strong earthquakes on the cultural heritage in the nearby (~30km) city of Florence makes a better knowledge of the seismicity in the Mugello basin an important target. To this respect, one of the principal, still unresolved issues concerns the location, extent and geometry of the fault(s) responsible for the 1542 and 1919 earthquakes. Such determination is of paramount importance for a reliable estimate of the hazard associated with those faults.

The present-day seismicity in the region is characterized by a moderate number of earthquakes, occurring with a rate of a few events per month**.** Most of the energy release is associated with short-duration (tens of days) sequences, exhibiting a clear mainshock-aftershock behaviour. Thus far, such sequences have exhibited low magnitudes (lower than or equal to 4.5). Nonetheless their accurate study is particularly relevant since it is expected to constrain fault location, geometry and kinematics, which all are the necessary ingredients for seismic hazard assessment.

Following these arguments, the main objectives of this PhD thesis consist of:

(i) to compile all the available seismological data in order to derive an integrated earthquake catalog for the Mugello basin and wider Northern Apennines;

(ii) to increase the instrumental coverage of the study area through the installation of a temporary network, whose noise levels and quality of measurements are useful for the future expansion and improvement of the permanent monitoring system;

(iii) from this data set, to calculate a 1D seismic velocity model and then, a 3D velocity map of the crust in order to interpret crustal scale tectonic processes, and to be used in future applications for more accurate location of local seismic events;

(iv) to derive accurate earthquake locations to constrain the position, shape and type of slip of active faults that are responsible for the seismic sequences occurring over the time period considered (2005 - 2021), focusing especially on the December 2019 sequence.

The thesis is structured as follows. First, I present an overview of the geological and structural setting of the study area, with details on the historical and instrumental seismicity (this Chapter). Then, I proceed by integrating different datasets and catalogs from the seismicity which has been

affecting the area since 2005 (Chapter 2). In Chapter 3, I describe the installation and operation of the local seismic network deployed in the frame of a specific collaborative project. In December 2019, that network recorded the most significant sequence of the last decade. Chapter 4 is dedicated to a Local Earthquake Tomography, conducted using the integrated set of phase arrival times obtained in the previous two Chapters. Finally, the most relevant seismic sequences which affected the study area in March 2008, September 2009, 2015-2017 and December 2019 are analysed in detail, and constitute the object of Chapter 5.

1.2 Geological setting

The Northern Apennines fold-and-thrust belt have been developing since Late Cretaceous following the closure of the Ligurian-Piedmontese ocean, intervening between Europe and Adria plates (Marroni et al., 2017, and references therein). Subduction phases have been referred to different models and the following collision occurred since mid-late Eocene (Marroni et al. 2017).

Currently, the Northern Apennines chain is composed of a complex nappe pile in which the uppermost tectonic units are the ocean-derived Ligurian Units (Jurassic-Eocene), widely outcropping in the internal sectors of the Apennines, with their associate satellite basins (Epiligurian Units, Oligocene-Early Miocene in age; Ricci Lucchi, 1987; Boccaletti et al., 1990; Bortolotti et al., 2001; Fig. 1.1). The Ligurian units overthrust the Sub-Ligurian Units (Paleocene-Eocene), interpreted as deposited in the transitional zone between the ocean to a continental passive margin. These units in turn rest onto the Tuscan and Romagna Units (Triassic-Miocene) deposited on the thinned continental passive margin of the Adria Plate (Bonini et al, 2014, and references therein).

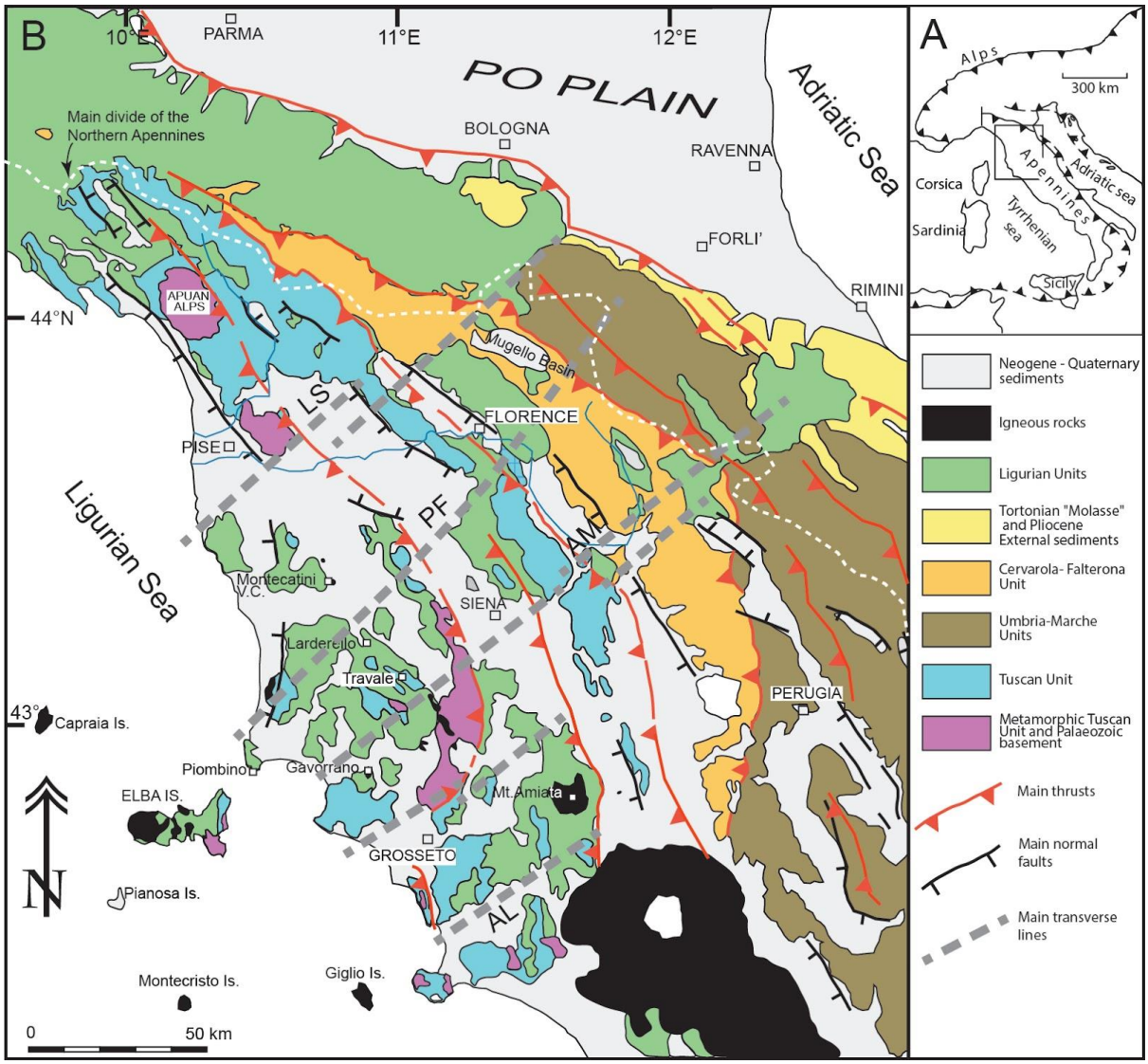


Figure 1.1: Geological and structural map of the Northern Apennines (Modified after Sani et al., 2016)

In the study area (Fig. 1.2), the Tuscan and Romagna Units are mainly composed of turbidite successions, accumulated in the foredeep basin developed at the leading edge of the advancing chain since the Oligocene. These thick (>2500 m up to 4000 m) turbidite successions are in general detached from their stratigraphic substratum represented by slope marls, and are arranged in a complex thrust system, which formed since the Early Miocene (Ricci Lucchi, 1986).

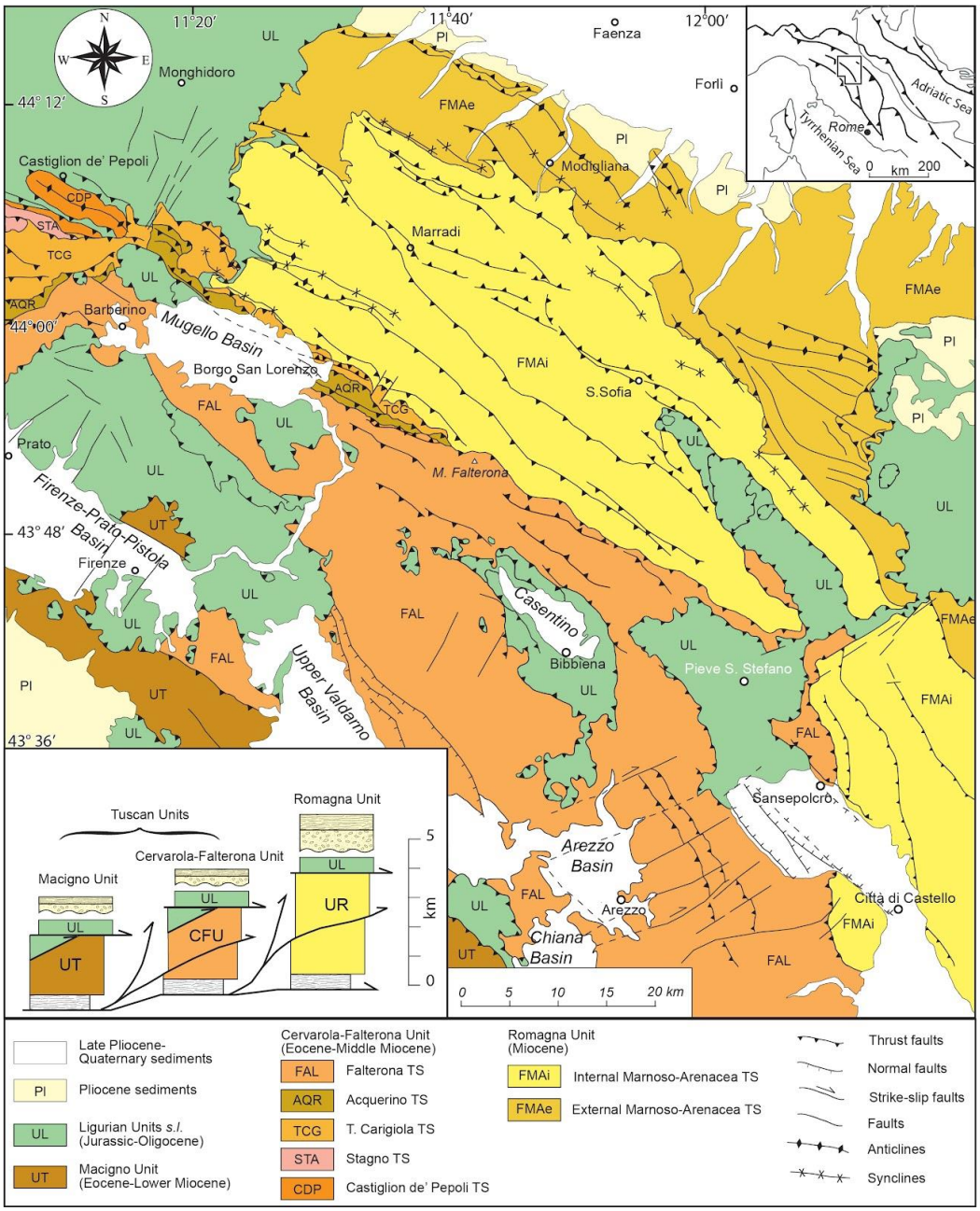


Figure 1.2: Schematic geology of the NE Apennines area (Figure from Sani et al. 2009, modified)

The polyphase compressional tectonics which gave rise to the current fold and thrust belt continued until recent times, as suggested by recent out-of-sequence thrusting and reactivation of older thrusts (Boccaletti and Sani, 1998, Finetti et al, 2005), and is still ongoing in the external sector of the chain (i.e., Po Plain) as the compressional seismic activity demonstrates (Maestrelli et al., 2017 and references therein). The interpretation of the late evolutionary stages of the internal sector of the chain is still a matter of debate. Most of the authors consider the Late Miocene-Late Pliocene basins as well as the continental Pleistocene basins (Mugello, Casentino and Sansepolcro basins) occurring along the Northern Apennines watershed, as grabens or half grabens, developed in an extensional regime since Neogene time (Martini and Sagri, 1993; Martini et al., 2001, and references therein). Other authors propose a more complex tectonic scenario based on the integration of stratigraphic and structural data carried out within the basin fill and along the substratum especially near the basin margins (Bonini and Sani, 2002; Bonini et al., 2014; Sani et al., 2016, and references therein).

According to this model, the Early Pleistocene evolution of the outermost belt of intermontane basins (Mugello, Casentino and Sansepolcro), was greatly affected by reactivations and activity of thrusts and back-thrusts constituting the chain. Therefore, since early Pleistocene these basins developed in a still compressional tectonic regime, and only since the Middle Pleistocene, the tectonic evolution of such basins was also conditioned by normal faults and major transversal lineaments that acted as tear or transfer faults (Sani et al., 2009; Bonini et al., 2016, and reference therein).

The belt of the outermost hinterland intermontane Tuscan basins, located near the main divide, is crucial for assessing the active tectonics and the related seismic hazard of the Northern Apennines. The seismicity affecting the area shows a high variability in terms of intensity, depth, and kinematics (Bonini et al., 2016). Along the main Apennine divide the stress field is currently extensional, with a roughly NE-SW-oriented minimum stress axis (σ3), as suggested by focal mechanisms (Pondrelli et al., 2002, 2006a; Chiarabba et al., 2005; 2015). Moreover, the occurrence of compressional focal mechanisms along the northeastern side of the Northern Apennines chain, as well as along the Romagna foothills, raises the question of the location of the boundary between extension and compression.

Strain maps derived from geodetic (GPS, InSAR) measurements show that the western and central parts of the northern Apennine belt exhibit a well-marked extension, with strain rates on the order of 50-80 10^{-9}/yr. Conversely, the northeast front of the Apennines is characterized by compressional tectonics, accounting for strain rates on the order of 25–50 10^{-9}/yr (Devoti et al., 2011). Due to such rapid transition of stress regimes, the Apennines chain are subjected to the largest strain gradients, which implies an accumulation of deformation (e.g., Devoti et al. 2011, 2018).

1.3 Historical and instrumental seismicity of the Mugello area

The study area (Fig. 1.3) is centered on the continental Mugello basin that is inferred to have developed in Early Pleistocene under a compressional regime and was later affected by normal faults as the compressional regime ceased around the Early-Middle Pleistocene transition (Sani et al., 2009). This area is characterized by a medium intensity seismicity with historical earthquakes with highest macroseismic magnitude of Mw = 6.02 (1542) and Mw = 6.38 (1919) (Rovida et al., 2021). A large SSW-dipping normal fault system, referred to as 'Ronta fault system', affects the pre-basin substratum mostly made of Miocene sandstones, and delimits the northeastern basin margin (Sani et al., 2009; Fig. 1.3). This fault system is ~25–30 km long and displays remarkable morphostructural evidence (Sani et al., 2009; Bonini et al., 2016). Fault-slip data indicate mainly dip-slip normal kinematics (average rake = −85°) and an average slip-rate of 0.16 to 0.37 mm/year has been estimated (Sani et al., 2009; Bonini et al., 2016).

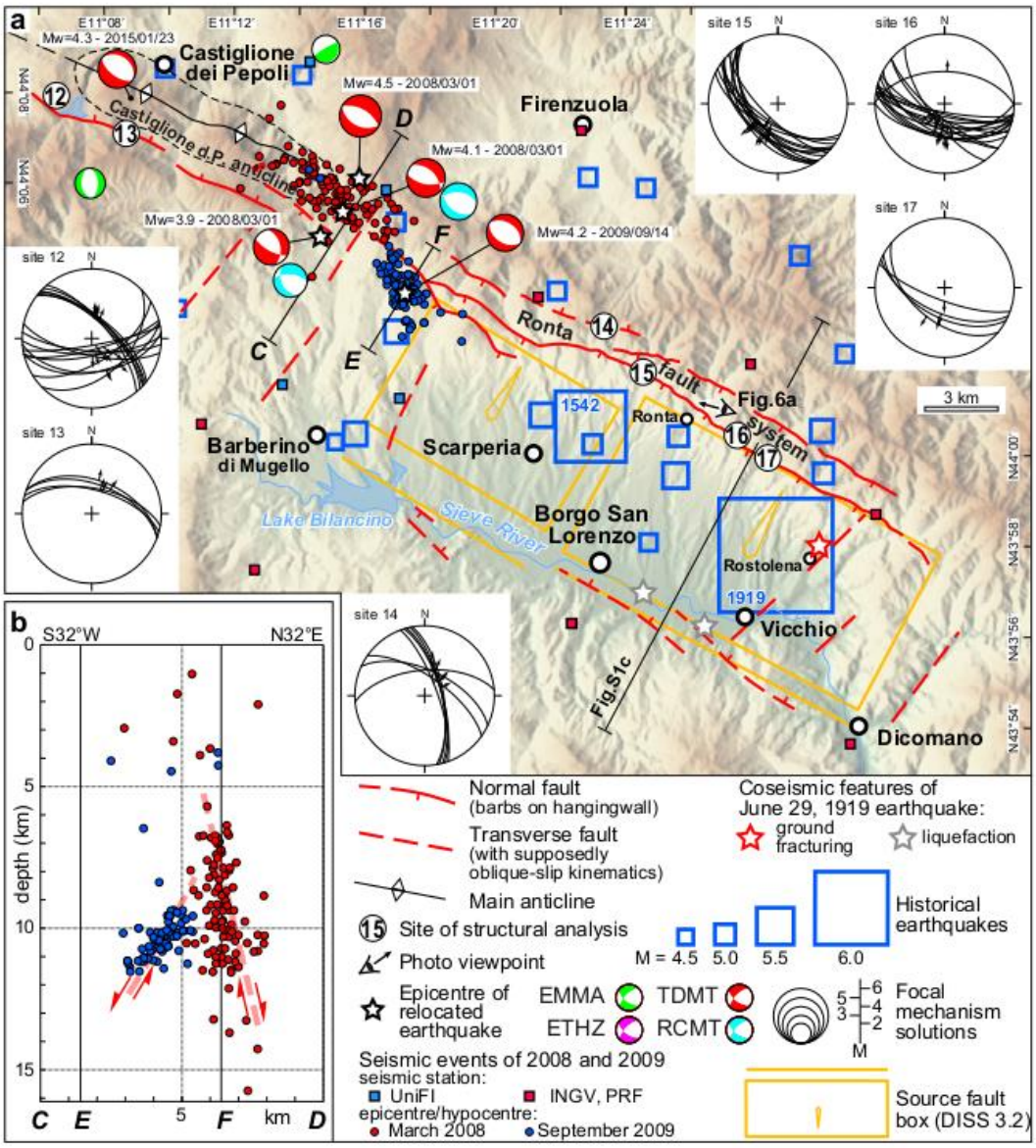


Figura 1.3: a) Major active faults and structural data of the Mugello basin region along with earthquake locations of the 2008 and 2009 seismic swarms, b) cross section through the 2008 and 2009 earthquake swarms with interpreted geometry and mode of fault slip (Figure from Bonini et al 2016).

The southwestern margin of the basin is affected by a system of NE-dipping antithetic normal faults, whose morphologic expression is scarcely pronounced (Benvenuti and Papini, 1997; Sani et al., 2009). However, it is believed to control the asymmetric location of the Sieve River on this side of the basin (Benvenuti and Papini, 1997), and previous studies locate along this margin the basin master fault (Martini and Sagri, 1993), which would be connected to the regional NE dipping low-angle Etrurian normal fault system (Boncio et al., 2000). The DISS Working Group (2018) catalogue follows this interpretation and subdivides the fault system into a north-western and southeastern segment, which should have caused the earthquakes of 1542 and 1919, respectively (Basili et al., 2008). Transverse faults at the north-western and south-eastern basin margins might represent other potentially active structures (Delle Donne, 2005).

During the seismic event of 1919, coseismic east–west-trending fractures affecting the ground surface were observed in the central-eastern part of the Mugello basin (Villa Ricci, near Rostolena;

Capacci, 1920). Moreover, liquefaction phenomena are reported nearby the Sieve River (Galli and Meloni, 1993). Unfortunately, the rough location of these deformation features does not allow identifying the source fault of that earthquake. The distribution of the sites with highest damage may suggest that a transverse fault may have also been activated by the 1919 event (Delle Donne, 2005; Sani et al., 2009). Based on length, lateral continuity, and its clear morphological evidence, the Ronta fault system could be considered the most likely source of the biggest earthquakes that hit the Mugello area, including the 1919 event.

Following that destructive earthquake, the area has been affected by a weak seismicity, except for short-duration seismicity bursts characterized by a typical mainshock-aftershock sequence, and maximum magnitudes between 4 and 4.5. The most recent of these sequences occurred in 2008 (Mw=4.5), 2009 (Mw=4.2), 2015 (Mw=4.3). This sequence, which occurred to the NW tip of the area of study and externally to the basin, was then followed by a minor sequence in 2017 located further NW of the 2015 cluster. The most recent sequence occurred in 2019 (Mw=4.5), at the NW margin of the basin. With the revision work described in Chapter 5, all these seismic sequences have been re-located, allowing a better definition of orientation and dip of the causative fault segments. Particular attention is dedicated to the 2019 sequence, which was also recorded by the local seismic network installed in the frame of this thesis.

Chapter 2

Archive data

2.1 Introduction

As for the rest of the italian territory, the region under study is monitored by the Italian National Seismic Network (INSN), managed by the Istituto Nazionale di Geofisica e Vulcanologia (INGV). A further network, named *Rete Sismica della Toscana Nord-Orientale* (RSTNO) is operated by the Fondazione PARSEC - Parco delle scienze e della cultura (http://www.csn.prato.it/). These two networks deliver separate earthquake catalogs, generated from different sets of phase arrivals. These catalogs are called the INGV catalog and the RSTNO catalog. In this chapter I describe the procedure used to generate a new updated and unified seismic catalog for the Mugello basin and surrounding areas, based on the integration of the two aforementioned data sources. This integration is expected to provide an increase of the number of phase arrivals, and a better azimuthal coverage of the target area, thus improving the quality of the earthquake locations. I accounted for the time period spanning the years 2005 – 2019, during which both catalogs exhibit the best completeness. I compiled data from all stations included in a box with limits latitude=[43.5°- 44.6°], longitude=[10.5° - 12.5°] (purple box in Fig. 2.1), and epicenters located within a smaller region with coordinate limits: latitude=[43.7°, 44.4°], longitude=[10.8°,12.2°].

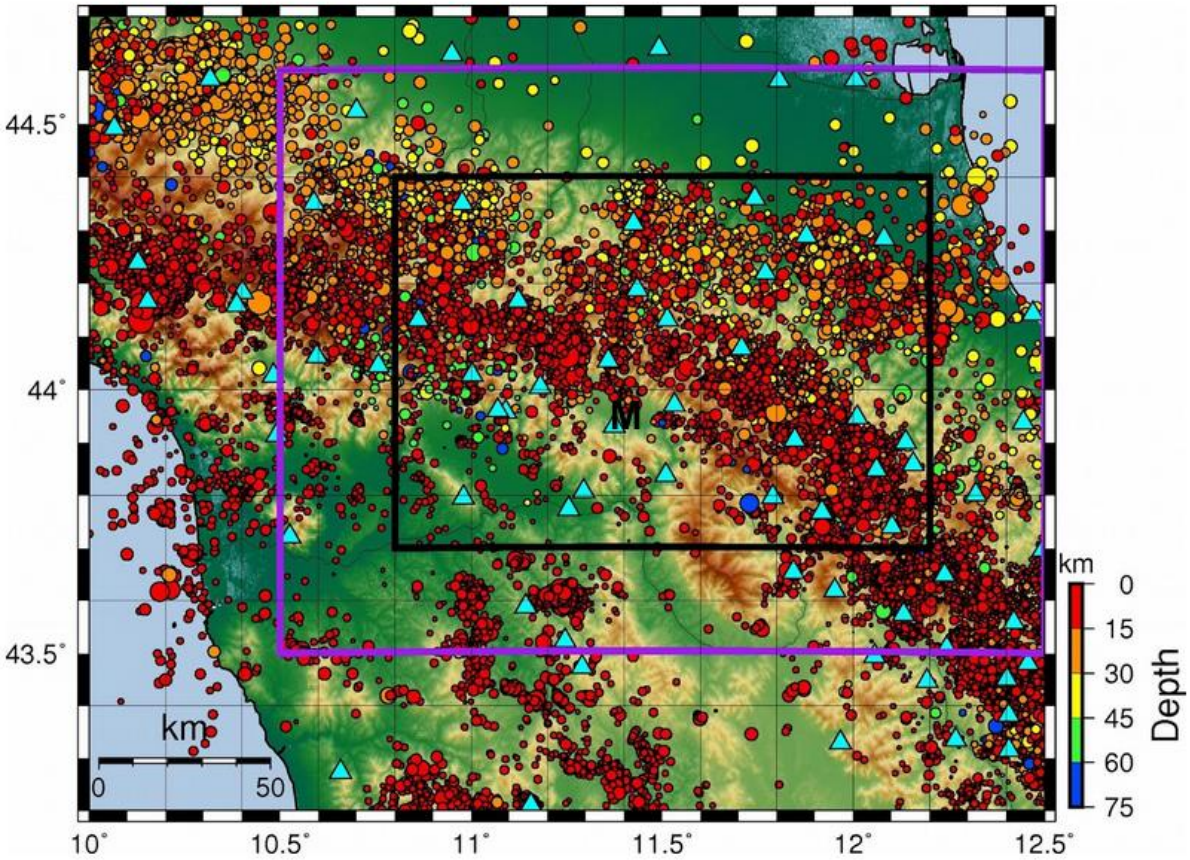


Figure 2.1: Seismicity for the 2005-2019 time span derived from the catalog of the INGV. The size of the dots is proportional to the magnitude (ranging from 0.1 to 5.0) of the events and their colour depends on the depth of the hypocenter. The triangle-shaped symbols represent the seismic stations of the INGV (ISIDe Working Group, 2007; INGV, 2006) in the area. The black box encloses the study area that contains the Mugello basin (M). The purple box includes the stations used for the study.

2.2 Data

For the two catalogs each event includes its date (year/month/day), time (hour/minute/second), geographic location (longitude, latitude), depth (in km), the P- and S-wave phase arrivals at each station and uncertainties of the picking. Below I describe the origin of the two catalogs, the error estimates of the locations in them, and then the procedure of how I merged them.

The parameters used to evaluate the accuracy and the precision of seismic location are the root mean squared travel time residual (RMS) in seconds, the number of phases used for locations (NPHS), the horizontal and vertical errors in km, and the azimuthal gap in degrees. The RMS is defined as $\sqrt{\frac{\sum_{i=1}^{n}(r_i)^2}{n}}$ where r is the residual (i.e., the difference between the observed and predicted arrival times for the i-th phase), and n is the number of observations. RMS is commonly used as a guide of an accurate hypocenter determination. The NPHS depends on the number of stations

concentrated in the epicentral area and on the quality of the signal registered in each station. This parameter is important because a large number of good and useful phases help to better constrain the hypocenter position. The azimuthal gap of an earthquake is the largest angle separating two adjacent seismic stations, both measured from the epicenter of the earthquake.

2.2.1 The INGV Catalog

At INGV, the seismic monitoring activity is conducted at the National Earthquake Observatory, located in Rome (https://www.ont.ingv.it/). There, earthquakes are initially located using an automatic procedure, and immediately relocated after manual picking in quasi-real time by an operator during the surveillance shift. Successively, the events are verified and relocated, using arrival times accurately revised by an expert seismologist. These revised locations are collected into a catalog, formatted according to the QuakeML standard (ISIDe Working Group, 2007). I accessed this catalog using a python script based on Obspy functions (Beyreuther et al. 2010; Megies et al. 2011; Krischer et al. 2015). Through these functions it was possible to select events and stations included in the areas of interest. For each earthquake, there may be different origins, i.e. pickings, locations and magnitude estimates. In the case that more than a single origin is present, the most reliable is that marked as Bulletin (i.e., it has been manually revised). Each origin has associated hypocentral coordinates, origin time, and the phase arrival times of P and/or S-waves at the stations which sensed the earthquake. Overall, the catalog within the region of interest is composed of 10094 earthquakes and 47 stations (Fig. 2.2). Figure 2.3 shows that 90% of the earthquakes have an RMS < 0.4 s, and the NPHS varies from 5 to 40. The longitude and latitude errors for 90% of the solutions is less than~1.6 km (Fig. 2.4). The depth errors for 90% of the events is less than 3.8 km (Fig. 2.4). The azimuthal gap of 62% of earthquakes is lower than 180 degrees, and for 90% is lower than 255 degrees (Fig. 2.4). The results are also shown in Table 2.2.

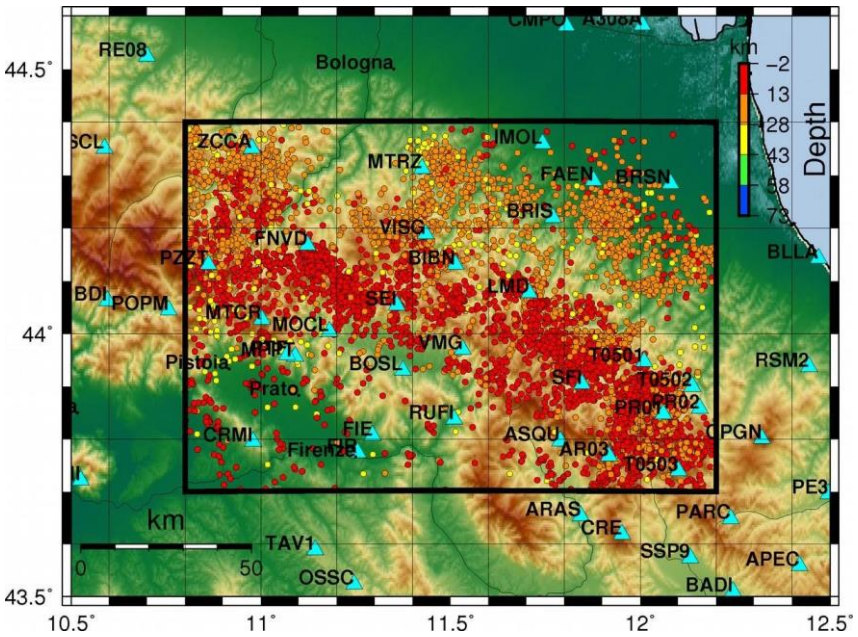


Figure 2.2: Map of INGV stations and earthquake catalog selected in my study. The INGV catalog is represented by 10094 earthquakes (dots colored by depth) and 47 stations (cyan triangles).

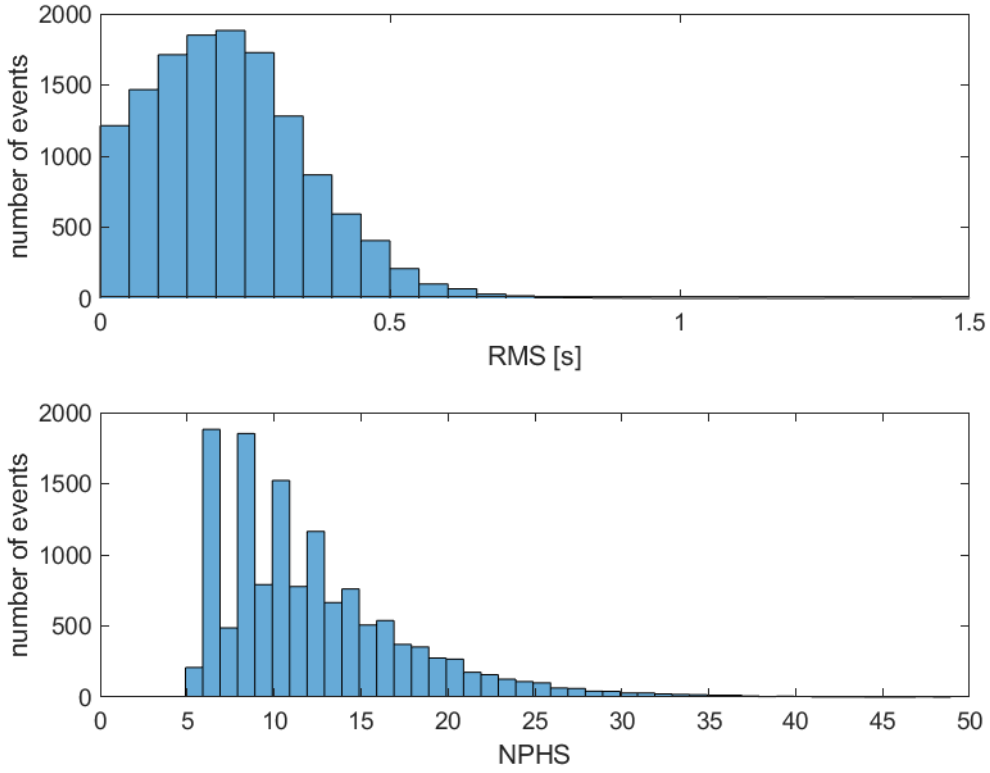


Figure 2.3: Histogram of the number of earthquakes versus the RMS (top) and the number of inverted phase arrival times (bottom) for the INGV catalog.

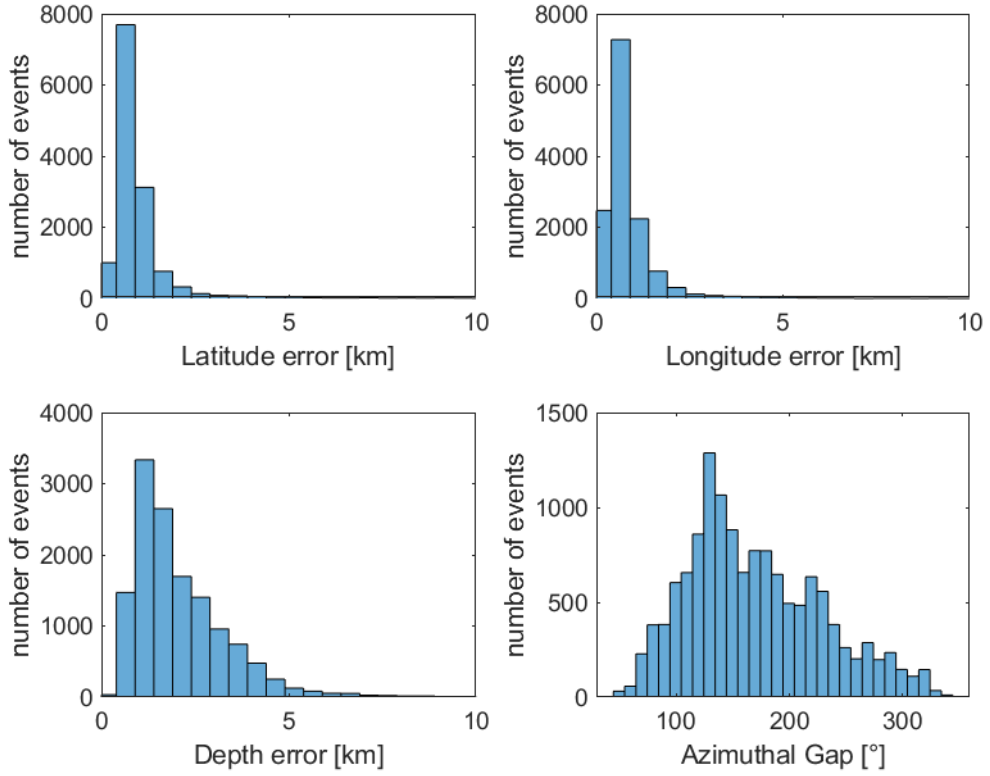


Figure 2.4: Histograms of location quality indicators of the INGV catalog. The top two panels show the two horizontal errors; the panels at the bottom illustrate the depth errors (left) and the azimuthal gap (right).

2.2.2 The RSTNO Catalog

The *Rete Sismometrica della Toscana Nord Orientale* (RSTNO), managed by the Istituto Geofisico Toscano (IGT), that is the geophysical and seismological section of the Fondazione PARSEC, monitors the seismicity of North-Eastern Tuscany. Although the RSTNO and INGV share data from several stations, locations are calculated independently. The seismic events recorded by the RSTNO are presented annually within the IGT bulletin. These locations are derived from phase arrival times picked manually by an expert seismologist, and inverted with the computer program HYPOELLIPSE (Lahr, 1989). From the Fondazione PARSEC I received the list of locations of the events detected from 2005 to 2019, and a list of phase readings in HYPO71 format. The uncertainties of the pickings are provided by a scale from 0 to 4 that corresponds to uncertainties in seconds. The pickings with weight 4 are not considered in the locations of the earthquakes. From 0 to 3 the errors in seconds associated are 0.01, 0.1, 0.5 and 1, respectively. In this case, the earthquakes were distributed over a larger area than the study one, so I ran a bash script to save only the events enclosed in the black area (Fig. 2.1). Instead, the stations of the RSTNO are all included in the purple area, so that no station selection was necessary. In the end, this catalog comprises 5741 earthquakes and 12 stations (Fig. 2.5). Figure 2.6 shows that 90% of the earthquakes have an RMS < 0.4 s, and for most of the earthquakes NPHS is 6. Given the low number of stations, the longitude and latitude errors are high with 90th percentiles of ~19 and ~13 km, respectively (Fig. 2.7). As for the depth errors, the 90th percentile is on the order of 15 km (Fig. 2.7). Furthermore, a large proportion of the earthquakes have an azimuthal gap higher than 180 degrees (Fig. 2.7). This is due to the few stations used for the locations and the concentration of them in a small area. These results are also shown in Table 2.2.

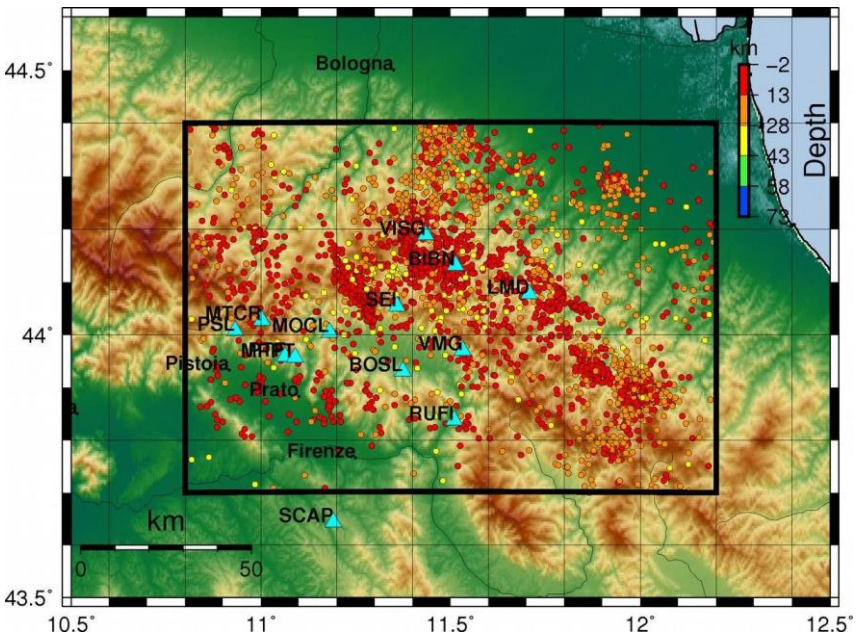


Figure 2.5: Map of Fondazione PARSEC stations and earthquake catalog. The catalog is represented by 5741 earthquakes (dots colored by depth) and 12 stations (cyan triangles).

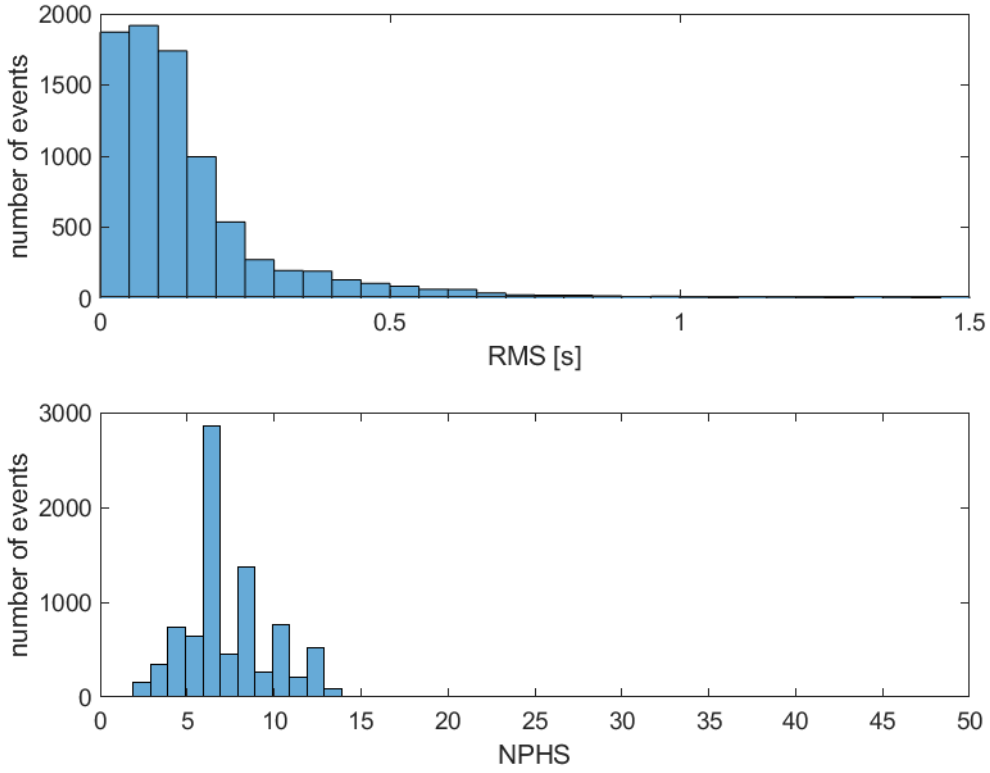


Figure 2.6: Histogram of the number of earthquakes versus the RMS (top) and the number of inverted phase arrival times (bottom) for the PARSEC catalog.

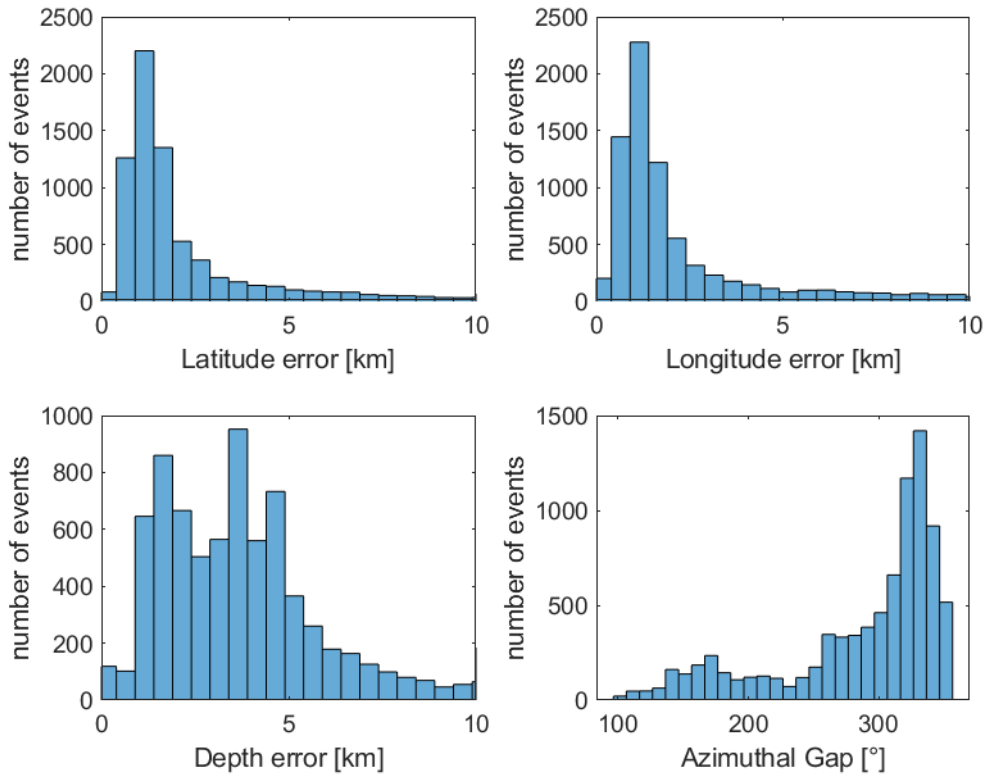


Figure 2.7: Histograms of location quality indicators of the PARSEC catalog. The top two panels show the two horizontal errors; the panels at the bottom illustrate the depth errors (left) and the azimuthal gap (right).

2.3 Method

To unify the two catalogs, I first relocated separately the two sets of phase arrival times.

I used a non-linear, probabilistic location procedure coded within the NonLinLoc (NLLoc) software package [Lomax et al., 2009]. This algorithm allows an efficient global search of the hypocentral parameters (spatial coordinates and origin time) obtaining an estimate of the posterior probability density function (pdf) of the hypocenter. The use of pdf for data and parameters in non-linear inverse problems was promoted by the original work of Tarantola and Vallette (1982). The NonLinLoc location algorithm is based upon this work, in which the *a posteriori* location errors depend not only on data uncertainties, which are directly expressed as the picking error in seconds, but also on model errors, i.e. uncertainties in the prediction of travel times as a consequence of an incomplete knowledge of the velocity model. These latter errors are implemented using the relationship: $C_{ij} = \sigma_T^2 \exp(-0.5(D^2_{ij})/ R^2)$, where C_{ij} is the element of the data covariance matrix associated with the i-th and j-th estimates of arrival time; D_{ij} is the distance in km between the i-th and the j-th stations; σ_T is a characteristic error (in seconds) in travel-time predictions; R is the correlation length of errors between stations, that is related to the length of lateral heterogeneities of the medium. In the present application, I used σ_T=0.1s, and R=1 km.

More specifically, I used the Octet Tree method implemented in NLLoc for exploring the spatial hypocentral parameters. In NLLoc theoretical travel times are calculated in reciprocal geometry using a finite-difference scheme (Podvin and Lecomte, 1990). The velocity model I used for the location is taken from Piccinini et al. (2014) and reported in Table 2.1. This model was derived from inversion of earthquake arrival times for best fitting 1D velocity model and earthquake source parameters for the Northern Apennines.

Top (km)	VP (km/s)	VS (km/s)
-2.00	5.030	2.779
1.00	5.620	3.105
3.00	5.730	3.166
5.00	5.760	3.182
9.00	5.820	3.215

11.00	5.880	3.249
15.00	6.110	3.376
19.00	6.410	3.541
30.00	7.770	4.293

Table 2.1: 1D velocity model proposed by Piccinini et al. (2014).

The output of NLLoc includes all the information about each earthquake, including the phases used for individual locations. Initially, this information exists for the catalog derived from the INGV and PARSEC networks separately. I then extracted the origin time of each event located by the 2 networks, combined these times into a single list, and sorted that list in chronological order. Then, I used a matlab script, which combined the phases of consecutive events whose origin times differed by less than 5 seconds. The INGV and PARSEC catalogs share a few common stations so in the case that two phases (P or S) of the same station are present, I chose the INGV phases picks. Finally, I located the earthquakes using this set of integrated phase arrival times derived from both networks. The resulting phase data was relocated again. Duplicated earthquakes were identified based on their geographic location and date/time of the earthquake and removed from the catalog. For the events common to both catalogs I prescribed the INGV computed magnitudes.

2.4 Results

The resulting catalog is composed of 12593 events located from a single set of arrival times that draws on all available information over the area of study for the period 2005-2019 (Fig. 2.8). The earthquakes are mainly clustered along the active fault systems running along the Northern Apennine mountain belt, and mostly range from the surface down to 25 km depth (Fig. 2.8), though a few extend down to depths larger than 60 km. From the cross-section B-B' one notes that the hypocenters in the Adriatic side of the Apennines span the 10 to 35 km depth interval, differently from the Thyrrenian side where most hypocenters rarely exceed 10 km (Fig. 2.9). The change in depth distribution has been noted previously (e.g. Amato et al., 1993; Frepoli and Amato, 1997), and interpreted as being originated by the change in tectonics across the Northern Apennines. In the Adriatic foredeep, which is characterized by compressional tectonics, earthquakes occur at depths which are larger than those encountered in the Tyrrhenian side, dominated by extensional stress regime.

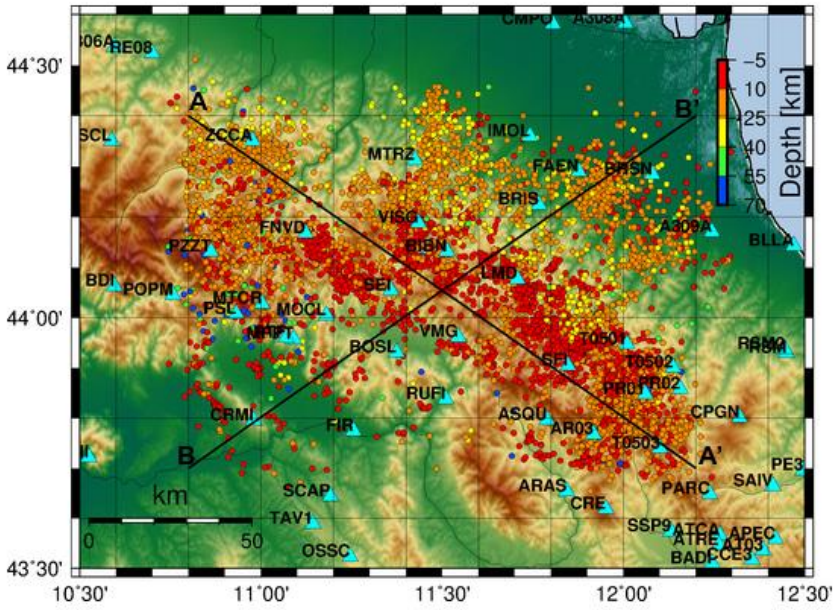


Figure 2.8: Map showing the fully merged and relocated earthquake catalog of the study region for the time period 2005 - 2019. The catalog was derived from the arrival times from the INGV and PARSEC networks, and it contains 12593 earthquakes spanning the time period 2005 - 2019. Positions of cross sections A-A' and B-B' are marked.

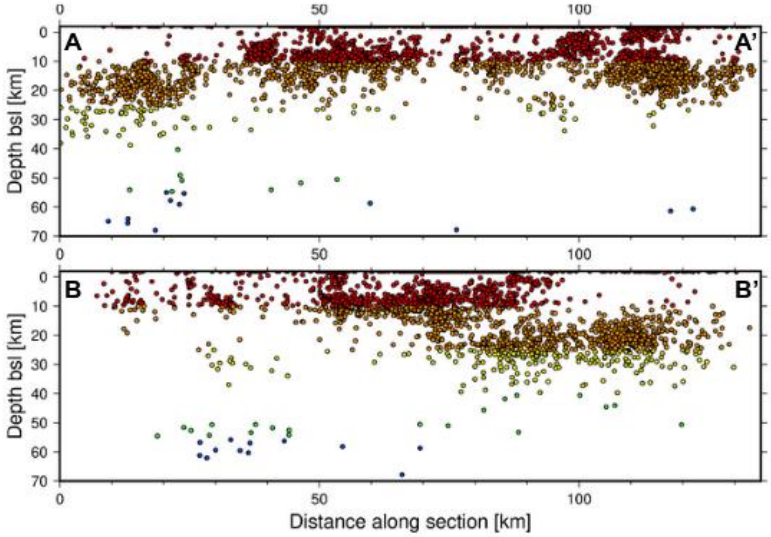


Figure 2.9: The cross-sections A-A' and B-B' of the merged catalog. Hypocentral depths mainly range from 5 to 25 km, though a few extend down to 60 km or more. The distance from which earthquakes are projected onto the cross section is 20 km.

I then analyzed the merged dataset in order to verify the distribution of the earthquakes and the quality of their locations. The top panel of Figure 2.10 shows that 90% of the earthquakes in the merged catalog have an RMS < 0.5 seconds, and the 90th percentile of NPHS is 24. The 90th percentiles of the location errors are ~1.5 km, ~1.4 km, and ~3.7 km for the longitude, latitude and depth coordinates, respectively (Fig. 2.11). 90% of the earthquakes have an azimuthal gap lower than 287 degrees (Fig. 2.11). Indications about the location performance and the improvement using the merged catalog are in Table 2.2, which reports the 90th percentiles of the quality indicators for the three

catalogs. Overall, the merged catalog has a larger number of phases and lower hypocenter errors if compared to the two source (INGV and PARSEC) catalogs. However, the merged catalog has an RMS residual which is larger than the two parent catalogs. This is likely due to the larger number of stations in the merged catalog: as it usually occurs in earthquake locations, lower RMS is achieved when the number of arrival times to be fit is small.

The best-located events of this catalog will be used in the subsequent analysis to derive a 1D velocity model and to perform the 3D local earthquake tomography (Chapter 4), and will serve to analyze the seismic sequences occurring over the period 2005 - 2021 (Chapter 5).

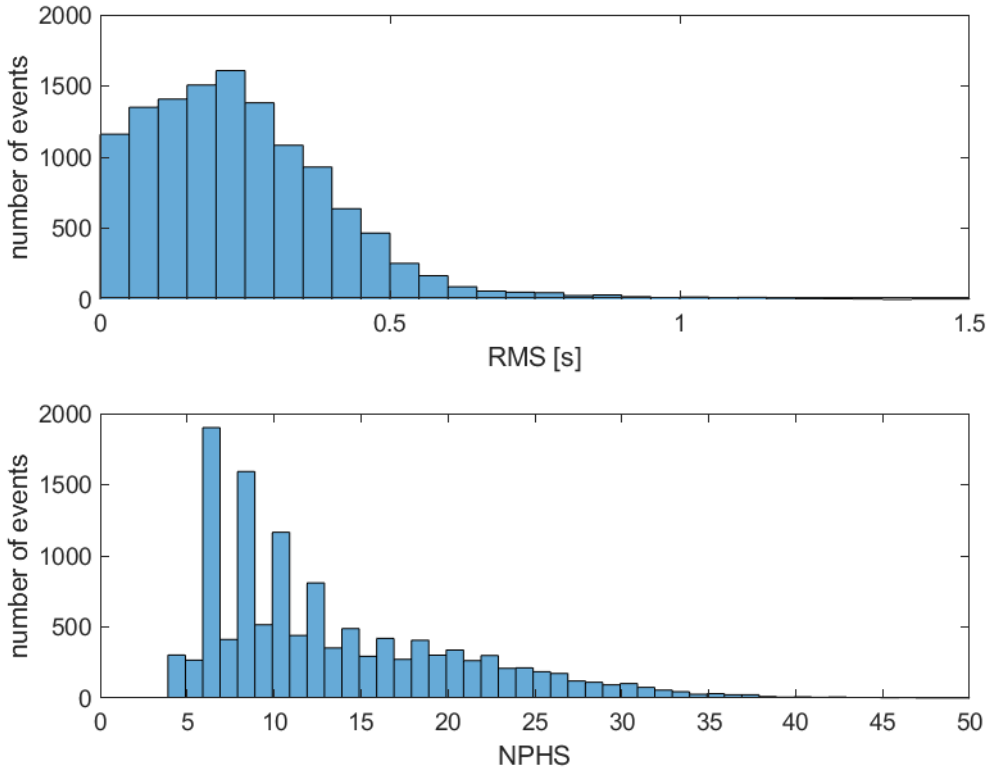


Figure 2.10: Histogram of the number of earthquakes versus the RMS (top) and the number of inverted phase arrival times (bottom) for the merged catalog.

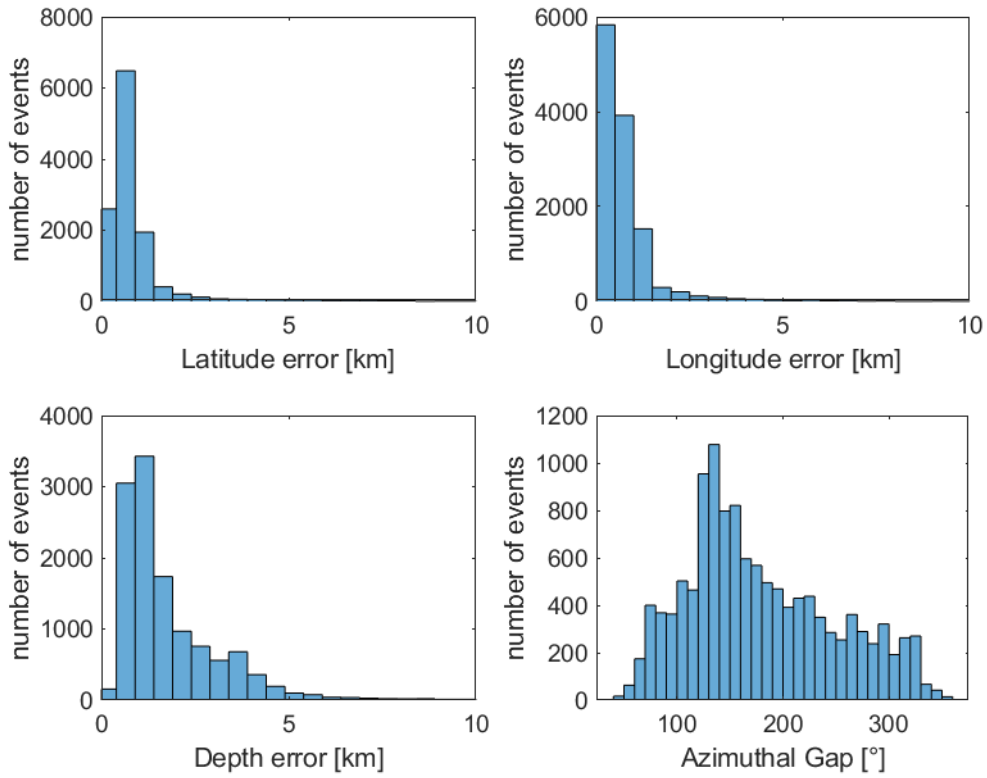


Figure 2.11: Histograms of location quality indicators. The top two panels show the two horizontal errors; the panels at the bottom illustrate the depth errors (left) and the azimuthal gap (right).

catalog	%90 RMS (s)	%90 NPHS	%90 lat err (km)	%90 lon err (km)	%90 depth err (km)	%90 azimuthal gap (°)
INGV	0.409	19	1.54	1.46	3.76	255
PARSEC	0.392	11	19.14	13.22	15.43	344
MERGED	0.458	24	1.45	1.36	3.69	287

Table 2.2: The 90th percentile values of RMS, NPHS, horizontal errors, depth errors and azimuthal gap for each catalog.

2.5 Conclusions

In this chapter I illustrated the method used to create an updated and unified seismic catalog based on the integration of the data obtained from the two seismic networks that monitor the study area. The data used are the phase arrival times from the catalogs of INGV and Fondazione PARSEC. The final catalog comprises 12593 events located using NonLinLoc, and the velocity model proposed

by Piccinini et al. (2014). The quality of the locations are mainly good, in particular, the 92% of the events have a RMS < 0.5s, the 86% of the solutions have the horizontal errors between 0.5km 1 km, and the 83% have the vertical errors less than 2.5 km, and the azimuthal gaps are mainly less than 120 degrees. This new merged and relocated catalog for the Northern Apennines will be used to select the best events to be considered in the next analysis on both 1D and 3D local earthquake tomography, and on seismic sequences occurring over the period 2005 - 2021.

Chapter 3

Temporary network, the 9M Mugello Temporary Seismic Deployment (MULTIPLY) network

This chapter is part of a report in Rapporti Tecnici INGV (in press):

Bruni R., Biagini D., Capello M., Corti G., D'Ambrosio M., Fiaschi A., Giunchi C., Keir D., Piccinini D., Sani F., Saccorotti G. *A temporary network for monitoring seismicity in the Mugello basin (Northern Apennines, Italy).*

The temporary network is registered to the International Federation of Digital Seismograph Networks (FDSN):

Bruni R., Saccorotti G., Keir D., Giunchi C., and Fiaschi A., (2019). *Mugello Temporary Seismic Deployment* [Data set]. International Federation of Digital Seismograph Networks. https://doi.org/10.7914/SN/9M_2019

3.1 Introduction

The seismicity of the study area is monitored permanently by the INSN and the RSTNO, as described in Chapter 2. The inter-distance of the permanent seismic stations ranges from 10 to 30 km. To better characterize the seismicity in terms of sensitivity in earthquake detection and accuracy in locations, a specific project was planned to increase the density of seismic stations in the study area, as aforementioned in Chapter 1. In this chapter I describe the steps of the installation of 9 temporary seismic stations, complementing the permanent networks presently operating, with the main goal to increase both the completeness and accuracy of the seismic catalog in and around the Mugello basin.

3.2 Site selection

The first step of the installation of a new seismic network is the site selection. The site selection procedure includes off-site studies and fieldwork. The off-site studies involve defining the geometry of the network on maps and collecting information about the potential sites from local and regional authorities. We defined a preliminary geometry of the temporary network, taking into account the permanent stations, in order to achieve a complete azimuthal coverage of the basin over a distance range of about 20 km. During the identification on map of the feasible sites it is important to also consider their proximity to plausible anthropogenic (such as roads, railways, heavy industry) and natural (such as forests, lake shores, rivers) sources of seismic noise. As a matter of fact, the most important characteristic of a site is the level of background noise that is evaluated by field measurement over a reasonable (at least one day) time interval. There were 9 sites to be identified and chosen, two of which coincided with existing but unused PARSEC sites. From November 2018 to May 2019 I participated in numerous field surveys with the aim of selecting the remaining 7 sites suitable for the installation of the seismic stations. Fieldwork essentially consisted of the scouting of the sites previously identified on maps. Site selection criteria includes the ease of access and site security, good Global Positioning System (GPS) signal reception, possibility of data transmission via Universal Mobile Telecommunications System (UMTS) digital telemetry, adequate sun exposure to allow powering the instruments through photovoltaic panels. During the scouting surveys, I also used a portable seismic station to assess the noise conditions of the site. In total, I participated in the survey of 12 sites, 5 of which were selected for the definitive installation. The other 2 sites were inspected by other members of the seismological INGV team of Pisa.

3.2.1 Procedure of the scouting survey

The measurements during the scouting lasted usually over 4 days. For this reason the installation realized in this step is simpler than the definitive one. The seismometer is wrapped in a plastic bag to prevent damage to the instrument by water and soil and is installed in a ~40 cm-deep hole. The sensor is oriented to magnetic north using a compass and leveled within the hole using an air-bubble on the top of the sensor. To better adjust the sensor to the soil, the soil was compacted and the sensor hole filled with sand. The seismometer is connected to the datalogger, which is positioned in an external box together with a battery and the GPS antenna. The battery is 40 Ah and is sufficient to power the instruments for the period of operation.

The instruments used for the scouting were provided by the INGV of Pisa. The seismometer is the three-component short period Tellus-1s manufactured by LUNITEK, with a flat velocity response between 1Hz and 100Hz (Fig. 3.1). The acquisition system is a 24-bit ATLAS (LUNITEK) datalogger equipped with a 1TByte internal memory card (Fig. 3.1).



Figure 3.1: The short period Tellus-1s seismometer (left) and the ATLAS acquisition module (right).

After the scouting the data that is recorded is collected and analysed. Site quality at individual stations of the temporary network is evaluated by calculating the probabilistic power spectral densities (PPSD) of the spectral power as a function of the frequency (McNamara and Buland, 2004; McNamara and Boaz, 2005), which are compared with the Earth's seismic noise models NLNM and NHNM (New Low- and High-Noise model, respectively) of Peterson (1993). In figure 3.2 I display two examples of the PPSD of seismic background noise, measured during the scouting of two sites, compared with the NLNM and NHNM. The color scale represents the percentage probability of observing a given spectral power at a given frequency. PPSD have been evaluated from consecutive power spectral densities (PSD) estimates taken on 600-s-long windows overlapped by 50%, spanning the days of continuous recording. I also investigated the possible presence of local amplification effects on the sites. For this purpose, I used the horizontal-to-vertical spectral ratio (HVSR) method [Nakamura, 1989]. The method consists of dividing the average of the Fourier spectra of the two horizontal components of ambient noise measurements with the corresponding spectrum of the vertical component. A curve is thus obtained which represents the ratio of the amplitudes HVSR as a function of frequency. The HVSRs were obtained over consecutive, 60-s-long noise windows spanning one day of continuous recording. Furthermore, I investigated the azimuthal variability studying the HVSR curves as a function of azimuth. This helps to understand the directional amplification of seismic noise.

At the end of the analysis of the sites investigated, I obtained the new 7 sites suitable for the installation of the seismic stations.

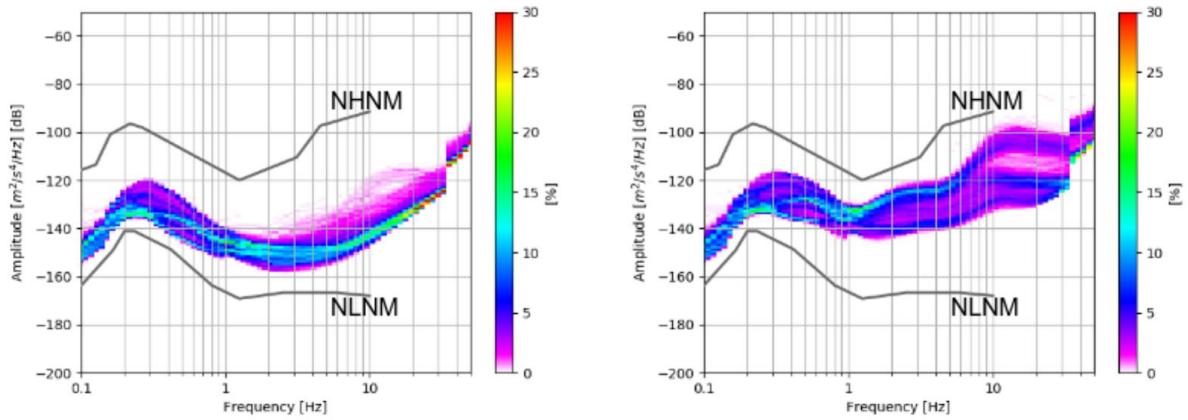


Figure 3.2: Examples of probabilistic power spectral densities of seismic background noise, used to evaluate the noise conditions at the investigated sites during two scouting in which I have participated. The gray curves are the Earth's seismic noise models: High-Noise model (NHNM) and New Low-Noise model (NLNM) of Peterson (1993).

3.3 Installation of seismic stations

Figure 3.3 shows the distribution of the stations in the study area. The 9 stations of the temporary network are represented with red symbols with two of the sites previously occupied by stations from the PARSEC Network (BOSL and VISG). The seismic stations of the permanent networks correspond to the blue symbols.

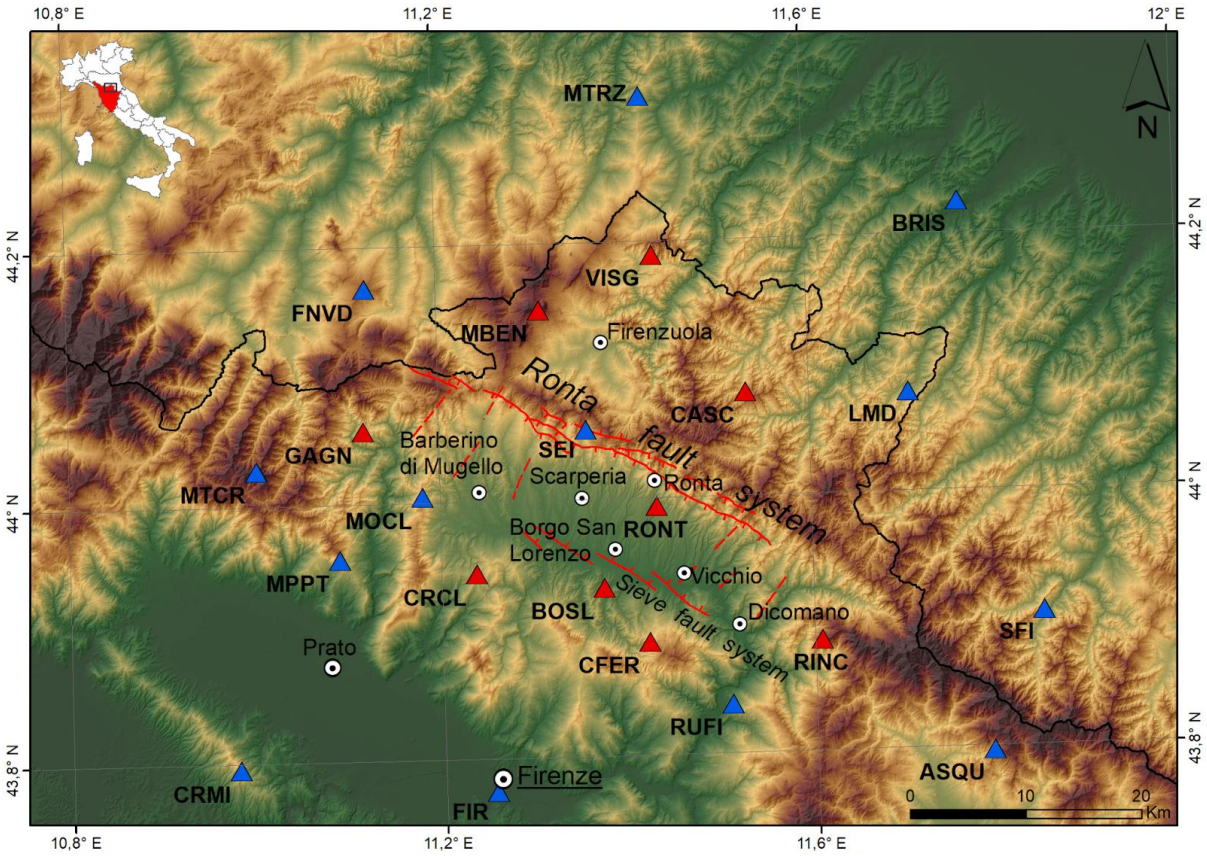


Figure 3.3: Configuration of the seismic stations in the study area. The 9 stations of the temporary network are represented with red symbols with two of these sites previously occupied by stations of the Fondazione PARSEC (BOSL and VISG). The blue symbols represent the seismic stations of the permanent networks (details about the DEM can be found in Tarquini et al. 2007 and Tarquini et al. 2012).

From the end of May 2019 to the beginning of July 2019, I collaborated with the team of the INGV of Pisa in the installation of the 9 seismic stations of the temporary network. The details of the installation (Fig. 3.4) are the following:

- The seismometer is installed in a ~50 cm-deep ~50 cm-wide pit on a cement base, with the top of the seismometer ~20 cm beneath the surface. The sensor is enclosed by a box covered by polystyrene sheets for thermal insulation. The whole installation is enclosed by a second, larger box for weathering protection.

- The acquisition-recording module is positioned in a separate box, together with the batteries, the power stabiliser, and the router for digital UMTS data transmission. The solar panels are mounted on a metallic frame, robustly anchored to the ground. The GPS and the UMTS antennas are placed on the metallic frame.

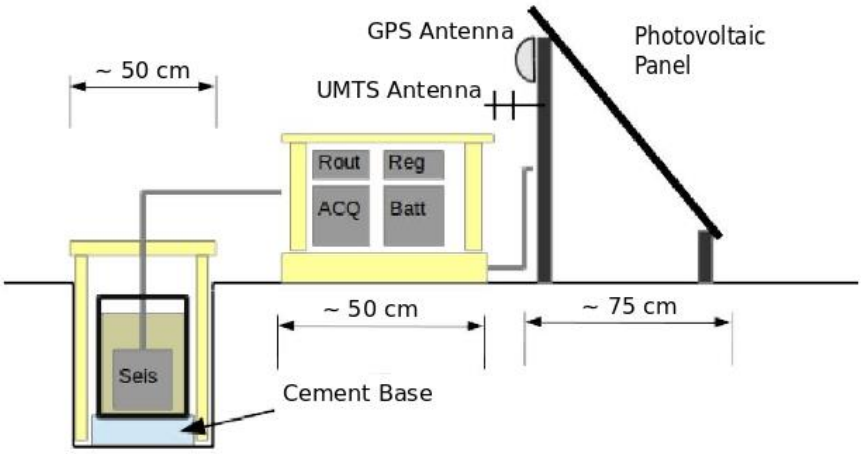


Figure 3.4: Configuration of the temporary seismic stations. The seismometer is placed on a cement base positioned at the bottom of a ~50 cm-deep pit. The acquisition-recording module, the batteries, the power regulator and the UMTS router for data transmission are stored in a separate box. The photovoltaic panels, mounted on a metallic frame, are robustly anchored to the ground. The UMTS and GPS antennas are installed on the metallic frame.

The most important step during the installation regards the seismometer. The sensor must be oriented to the magnetic North and must have a good coupling with the cement base that is in turn coupled with the soil. Using the air-bubble on top of the sensor we leveled the sensor within the pit. Prior to closing the box, I checked the mass-positions, data recording streams and GPS synchronization with Güralp software run from a pc connected to the acquisition module. Another feature of the installation is that the larger box that encloses the sensor is placed on a polystyrene sheet to avoid the transfer of tremor due to wind or rain that strike the box.

At the beginning, the stations recorded data locally on an internal hard-disk. Then, from the end of July 2019, the INGV team of Pisa progressively deployed UMTS routers, so that after October 2019 data from all the stations were received in real time by a SeiscomP3 server located at INGV, Pisa. I registered the temporary network as 9M to the International Federation of Digital Seismograph Networks (FDSN) with the name of MULTIPLY (Mugello Temporary Seismic Deployment; Bruni et al., 2019). Data from 3 of these seismic stations were forwarded to the INGV acquisition center, contributing to the seismic monitoring of the area.

The network remained operative till the end of May 2021, when the team of INGV Pisa dismantled it. After that, I saved all the data registered in the local hard-disk of each station in a separate hard-disk to check if the data transmitted were complete.

3.3.1 Instrumental characteristics and data

The instruments were provided by SEIS-UK, which is the seismic arm of the Natural Environment Research Council (NERC) Geophysical Equipment Facility (GEF), and is based physically at the University of Leicester, UK. They consist of 40TD broadband Güralp seismometers, each connected to a CMG-DCM/EAM Güralp acquisition module. The sensor has a flat response to velocity from 0.033Hz (30s) to 100Hz. Each seismometer is connected to a 24-bit CMG-DCM/EAM Güralp acquisition module (Fig. 3.5), with time synchronization achieved via reception of the GPS time signal. The acquisition modules were also equipped with an internal 40Gb hard-disk. Dataloggers were set in continuous recording mode with a sampling rate of 100 samples per second (sps).

The standard configuration of the temporary stations also includes four photovoltaic panels of 36W, two power batteries, a power stabiliser, a GPS antenna and a UMTS router (Fig. 3.5). Table 3.1 shows information regarding the station names and locations for the temporary stations. In the Supplementary Materials I report the data sheet of each station.



Figure 3.5: The 40TD broadband Güralp seismometer on the left and the DCM/EAM Güralp acquisition module in the middle, and the lightweight low power GPS module on the right.

After the installation, to control the state of health of the stations and maintain a good quality of the data, I calculated at each station the PPSD, as described previously, which are compared with the Earth's seismic noise models NLNM and NHNM of Peterson (1993). PPSD have been evaluated from consecutive power spectral densities (PSD) estimates taken on 600-s-long windows overlapped by 50%, spanning 7 days of continuous recording.

I also evaluated the HVSR, obtained over consecutive, 60-s-long noise windows spanning one day of continuous recording. PPSD and HVSR data at the different sites are reported in Supplementary Materials.

Station	Lat (WGS84)	Lon (WGS84)	Z (m.a.s.l)	Local area	Municipality
MBEN	44.14831	11.3107	1061	Monte Beni	Firenzuola
BOSL	43.93093	11.37433	380	Borgo San Lorenzo	Borgo San Lorenzo
CASC	44.08059	11.53222	740	Cascheta	Palazzuolo sul Senio
CFER	43.88798	11.42189	673	Collefertile	Borgo San Lorenzo
CRCL	43.94426	11.23742	506	Il Lavacchio	Croci di Calenzano

GAGN	44.05697	11.11862	670	Gagnaia	Cavarzano
RINC	43.88639	11.60719	955	Rincine	Londa
RONT	43.99353	11.43296	341	Ronta	Borgo San Lorenzo
VISG	44.18896	11.43431	727	Visignano	Firenzuola

Table 3.1: Location of the seismic stations from the 9M network.

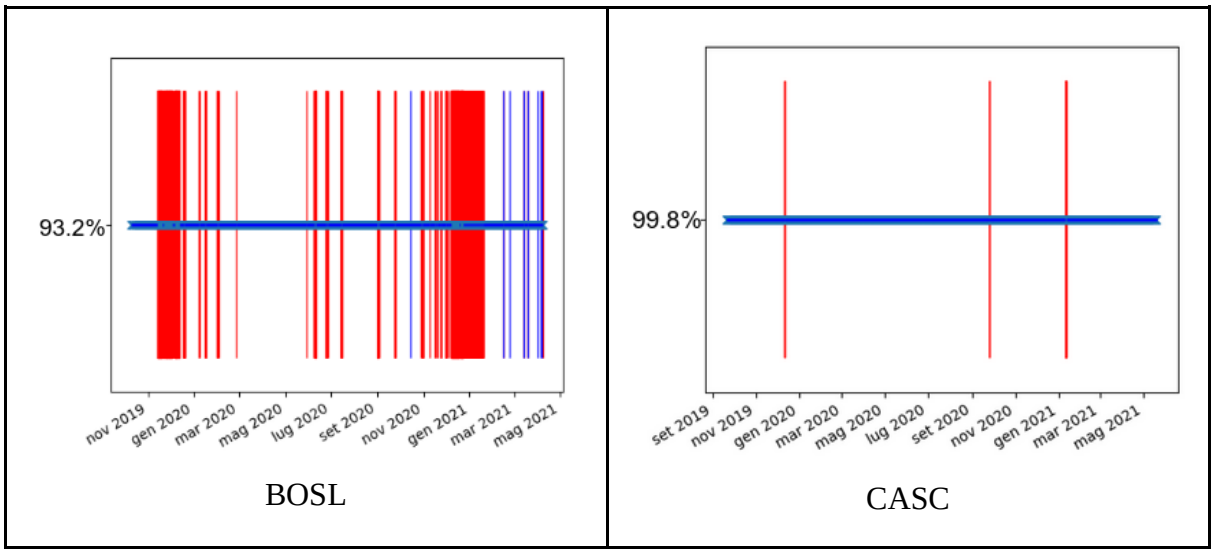
3.3.2 Network performance

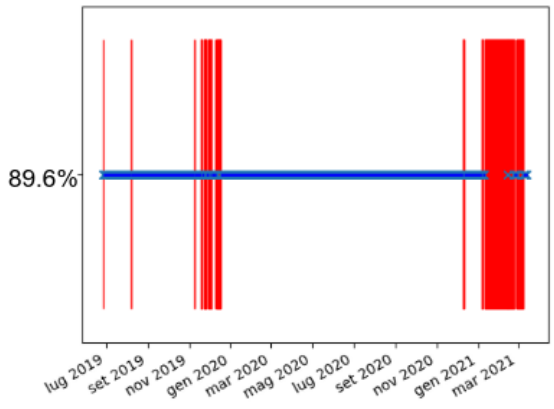
The 9M network provided a dense distribution of seismic stations that recorded data for 23 months from June 2019 to May 2021. The stations operated constantly and continuously with gaps in data acquisition being mostly due to shortage of power, especially in winter times, when the solar panels have been occasionally covered by snow or clouds and rain covered the sun. Due to the remoteness of most of the sites, a further issue was the occasional loss of the UMTS signal. In Fig. 3.6 I reported the temporal continuity of each station, and the red lines represent short-duration data gaps.

A particular station is BOSL, where after a week of installation I had to change the instruments due to a problem with the acquisition module and the sensor. In that case, I put a CMG40-T 1s sensor and a TAURUS Nanometrics acquisition module thanks to the Fondazione PARSEC that owns the site. After that it remained operative till the dismantling of the network without problems.

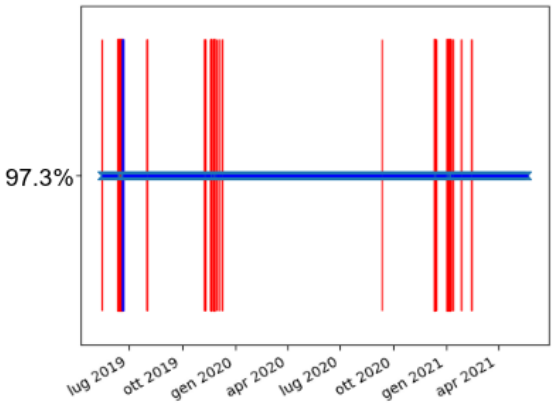
The stations with gaps, due to bad weather, were GAGN and MBEN. For the first, during May/June 2020 I had to substitute the sensor using the spare one provided by SEIS-UK. For the other, I had to reactivate the datalogger and the router. Apart from this time period the percentage of data acquired from GAGN and MBEN over the remaining time period was 82.1% and 84.5% respectively.

The rest of the stations in the network worked properly for more than 90% percent of the entire time. The only exception to this was CFER which has 89.6% of data continuity due to problems with the seismic instrument during the last few months of recording (Fig. 3.6).

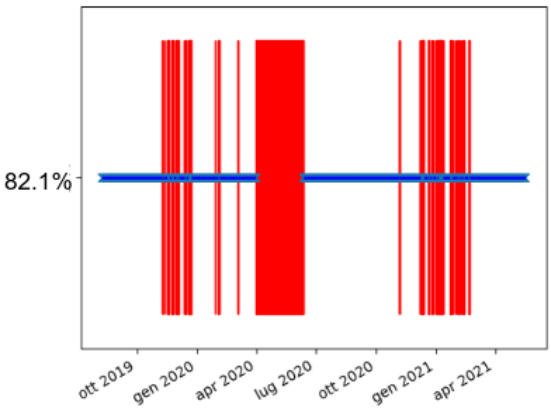




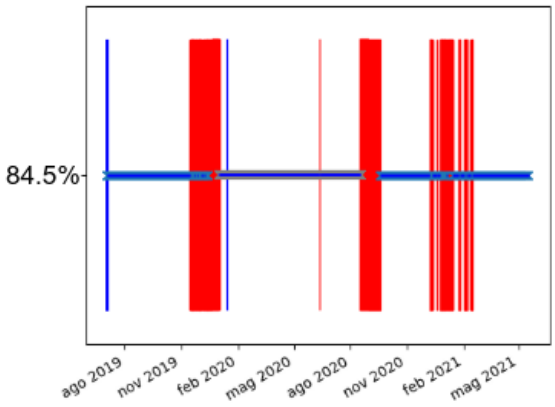
CFER



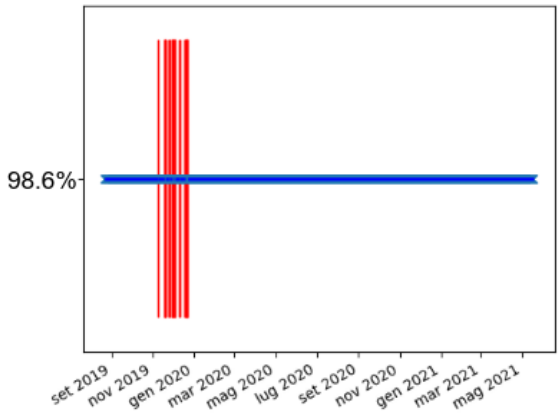
CRCL



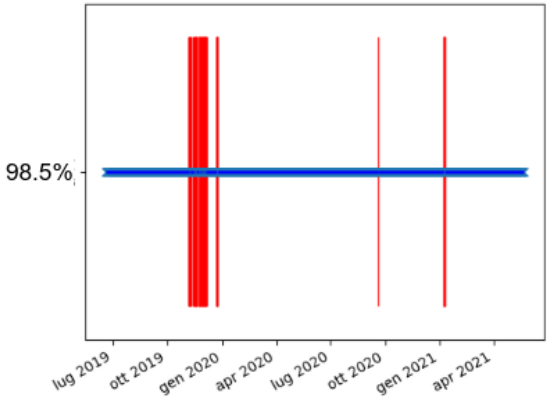
GAGN



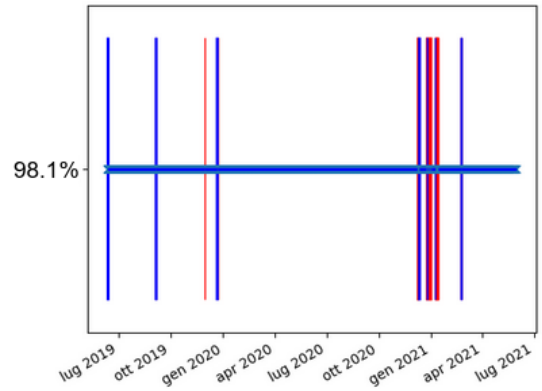
MBEN



RINC



RONT



VISG

Figure 3.6: The figures represent the station performances in terms of recorded data. The red lines correspond to short-duration data gaps.

3.4 Conclusions

In this chapter I described the procedure of the installation of the 9M MULTIPLY temporary network in the Mugello basin. This network, made up of 9 seismic stations, complemented the permanent networks currently operating from June 2019 to May 2021. The aim of the deployment was to enhance the completeness and the accuracy of the seismic catalog over the study area. In the first section I reported the steps of the site selection, that included the analysis of the background seismic noise of more possible and suitable sites. Then I illustrated the installation of the seismic stations. The stations operated constantly and continuously. Some gaps in the data were due to shortage of power for bad weather conditions. Anyway, the data recovery for the majority of the stations is above 90% of the all functioning period.

Chapter 4

Local Earthquake Tomography

4.1 Introduction

In this chapter, I aim to retrieve a 3-dimensional (3D) seismic velocity model of the crust in order to (i) understand crustal-scale tectonic deformation processes and its relationship to near-surface fault structure, and (ii) to re-locate earthquakes more accurately. For this procedure I used local earthquake tomography (LET, hereinafter; Kissling 1988), a passive method which exploits travel time information from local earthquakes to image the seismic velocity of the crust. In LET inversions, seismic rays must provide a homogeneous illumination of the volume under investigation. This implies that the sources (i.e., the hypocenters) and observers (i.e., the seismic stations) should be uniformly distributed. A further requirement is the availability of a reference velocity model to be used as a starting model for the subsequent iterative inversion of travel times. Methods and procedures for selecting travel time data and deriving a starting 1-dimensional (1D) velocity model are described in the following chapter.

4.2 Starting 1D velocity model

The first step in the majority of local earthquake tomography studies is to constrain a 1D velocity model that best fits the arrival time data from the region under investigation. The 1D model expresses the depth dependence of seismic velocity, described as discrete steps or as progressive variations in velocity over a depth range. In this section I describe the input data, methods and results for obtaining a 1D model representative of the northern Apennines. This constitutes a necessary step to derive a starting model for the subsequent 3D seismic tomography.

4.2.1 Data

The data used for constraining the 1D model are taken from the integrated earthquake catalog I derived for the time period 2005 to 2019 resulting from merging earthquake catalogs of the INGV and PARSEC, as outlined in Chapter 2. This catalog contains 12593 earthquakes, recorded at a minimum of 3 stations that all lie within the area of 43.7°- 44.4° latitude and 10.8°- 12.2° longitude.

In order to improve the construction of the velocity model, it is necessary to select the best events of the earthquake arrival time dataset by applying a number of filtering criteria, designed to select the earthquakes that have the best constrained hypocentres. The range of criteria that can potentially be used are the number of P- and S-wave arrival times used for the location, the azimuthal gap, the RMS, or selecting events whose minimum distance to a station is less than twice the focal depth. For my study, I selected events obtained from at least 20 arrival times, including at least 10 S-wave arrivals, thus obtaining 1796 events (Fig. 4.1). Due to the dense seismic network, coupled with utilized seismic stations being outboard of the region of seismicity considered, the vast majority of earthquakes satisfying the selection criteria exhibits a small distance to the closest station (Fig. 4.2) and a low azimuthal gap (less than 180 degrees) (Fig. 4.3). The average distance to the closest station is around 10 km, and for the 90% it is less than 17 km (Fig. 4.2). Figure 4.2 also shows the RMS distribution for this dataset; which shows that the average value for the selected events is 0.3 s. I also show the horizontal and vertical errors, that are mainly around 0.4 and 1 km respectively (Fig. 4.3). These elements demonstrate that a simple phase number selection criteria is sufficient to significantly improve both precision and robustness of the earthquake catalog to be used for the subsequent tomographic inversion.

The earthquakes mainly occur along the Apennine chain, according to a large number of spatial clusters that are distributed along the full width of the study area. Along the chain the earthquakes are distributed mainly above 10 km depth, with some down to 25 km. In contrast, beneath the Adriatic side of the Apennines the earthquakes are mainly located between 10 and 25 km depth. Minor seismicity occurs down to 65 km depth.

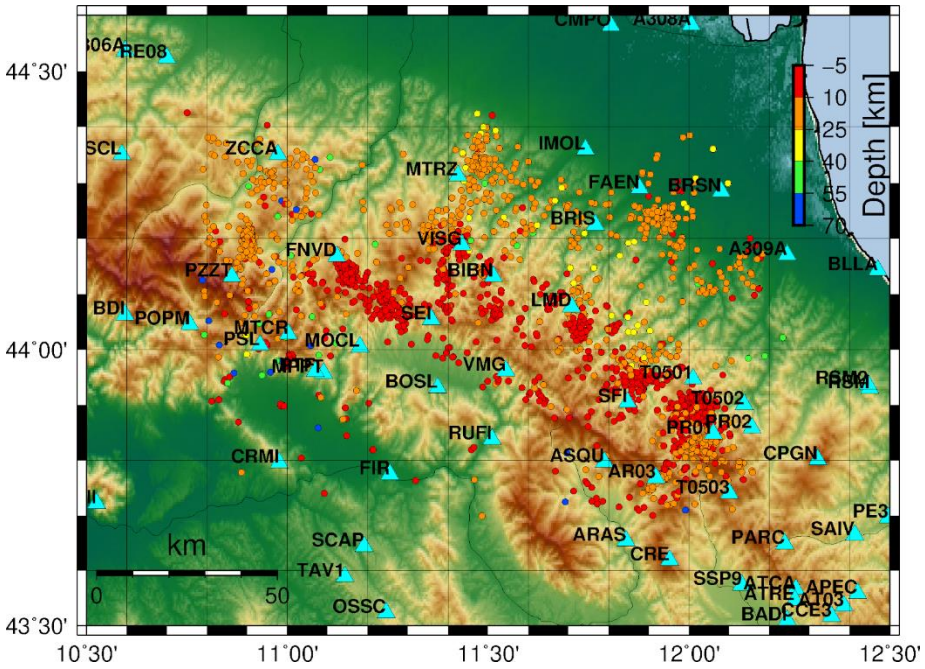


Figure 4.1: The 1796 earthquakes selected from the merged dataset and used for the best-fit 1D velocity model analysis.

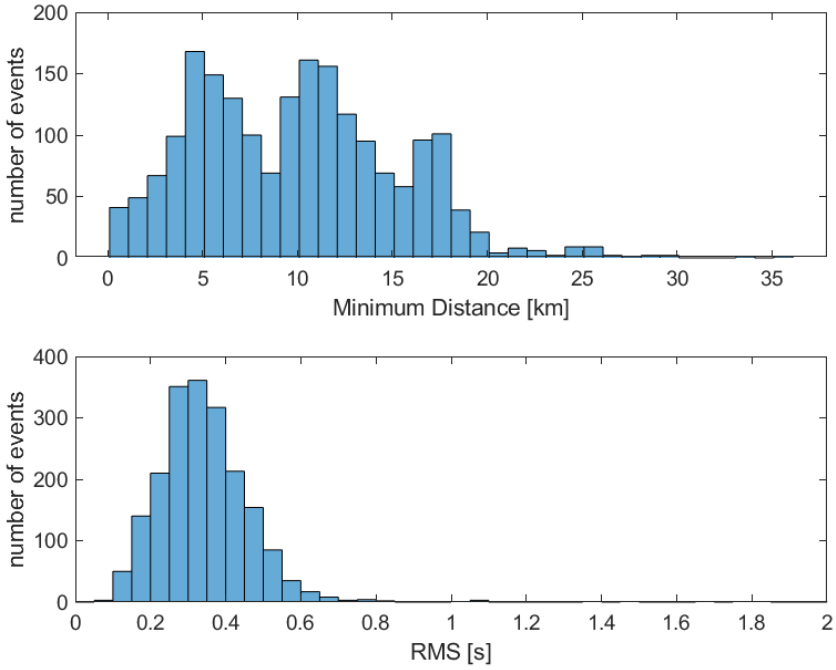


Figure 4.2: The distance of the station closest to the epicenter, the average is around 10 km. The RMS vs the number of events for the dataset selected, that comprises events with at least 20 phase readings.

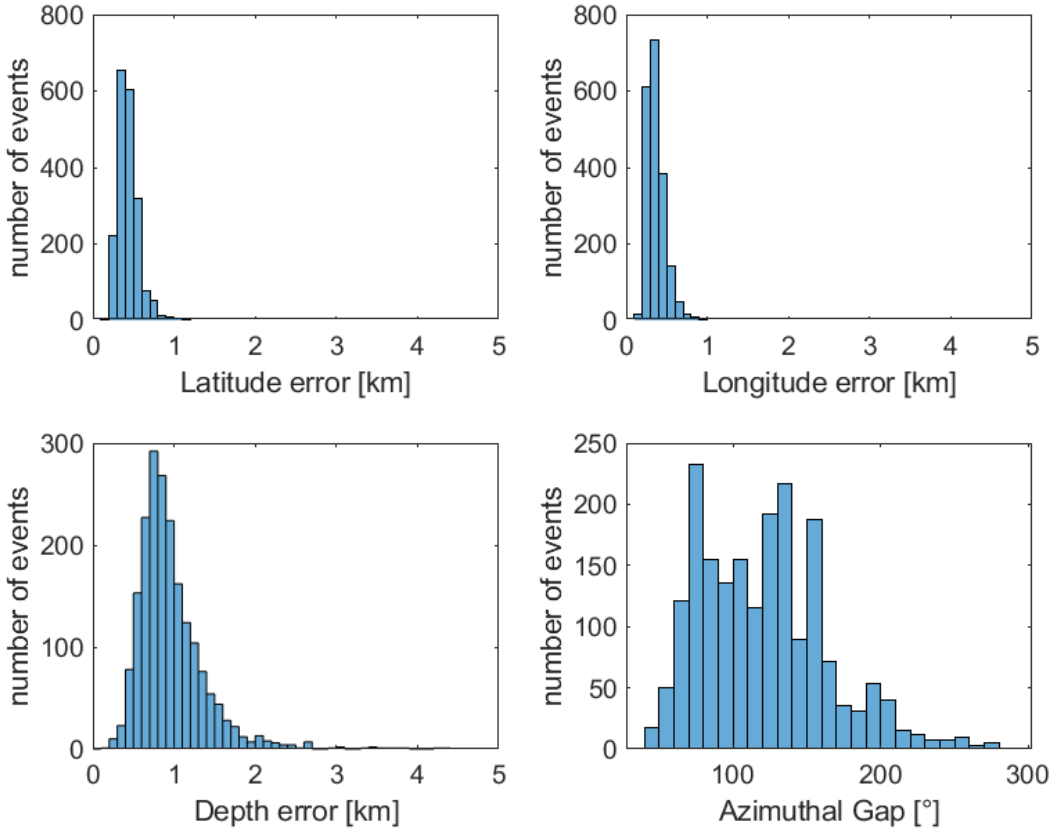


Figure 4.3 Top panel shows the horizontal errors, that are mainly around 0.3 km. The bottom left panel shows the vertical errors, that is an average. of 0.7 km. The bottom right panel shows the azimuthal gap for the dataset selected, that comprises events with at least 20 phase readings.

4.2.2 Method

I used the Velest program (Kissling et al. 1995) to define a best-fit 1D velocity model, or alternatively called the minimum 1D model, of the study area. The determination of the optimal model is an iterative process that starts from a trial model, either created by the user using available geological information or from previous regional or neighbouring velocity models. Given the non-linearity of the problem, Velest iteratively calculates the solution, i.e. the minimum velocity model, until it reaches the lowest root mean square (RMS) that is the misfit between the predicted and the observed travel times (Kissling et al. 1995).

The Velest procedure can use both P and S-wave arrivals to invert for a Vp and Vs model. It is possible to specify a value of the Vp/Vs ratio of the final model or leave the program to evaluate it for each layer. As a starting velocity model, I first used that derived from a previous inversion of seismicity for a 1D model in Piccinini et al. (2014). This model includes 10 crustal layers with Vp increasing from 0 to 33 km depth, and a Vp/Vs ratio of 1.81. The model does not explicitly consider topography since it has a starting depth of 0 km. I used the same layering structure as Piccinini et al. (2014), but using a starting depth of -2 km in order to consider the maximum surface elevation of the region.

In order to test the impact of the starting model on the best-fit 1D model solution I used a new starting velocity model, obtained after merging adjacent layers of similar velocity, and using a Vp/Vs ratio derived from a modified Wadati diagram of the data (Chatelain, 1978). Considering an event that is recorded by two stations (i,j) at hypocentral distances xi andxj, the differences between the arrival times of P- and S-waves can be expressed as $\Delta T_P = P_i - P_j = (x_i - x_j)/V_P$ and $\Delta T_S = S_i - S_j = (x_i - x_j)/V_S$. This leads to $\frac{\Delta T_S}{\Delta T_P} = \frac{V_P}{V_S}$, so a linear regression of ΔT_S versus ΔT_P for all available pairs of stations provides an estimate of V_P/V_S, the ratio between compressional and shear-wave velocities (Pontoise and Monfret, 2004). In the present application, the modified Wadati diagram yields a best-fit Vp/Vs ratio of 1.7300 ± 0.0008, typical of continental crust (Fig. 4.4).

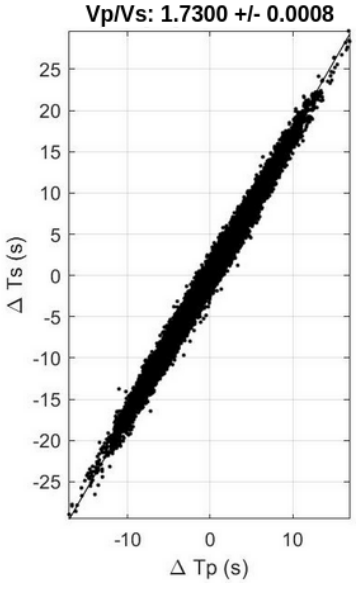


Figure 4.4: The result of the modified Wadati diagram: best-fit Vp/Vs ratio of 1.7300 ± 0.0008.

Due to the difference in the Vp/Vs of 1.81 in the starting model taken from Piccinini et al. (2014) and the value of 1.73 that I derived, I also ran the inversions using a starting Vp/Vs ratio of 1.73. I also ran the inversions from the starting 1D models using for the final model both a fixed Vp/Vs ratio for all layers, and allowing the Vp/Vs ratio to vary from layer to layer.

4.2.3 Results

The results achieved using Velest are shown in Figures 4.5. A common feature of the different runs is that lower RMS was achieved in the inversions that allow Vp/Vs to vary from layer to layer, and therefore these are the models that are shown in Figure 4.5. Overall, both the final Vp and Vs models are similar irrespective of the starting Vp model and Vp/Vs ratio. Looking in more detail, down to 20 km depth the two final models (named *output1* and *output2*) are similar, especially for the P- waves. Below a depth of 20km, the output models follow the trend of the respective starting model. This strongly suggests that the output model is well constrained and independent from the starting model in the top 20 km. However, from 20 to 33 km there is paucity of rays paths due to a very limited number of earthquakes located below 25 km depth, with the result that the model is poorly constrained below 20km depth.

My favoured minimum 1D P- and S-wave velocity model is model *output1* (red lines, Fig. 4.5), that is the output derived from the starting model of Piccinini et al. (2014) and with the output Vp/Vs variable for each layer. This is the best minimum 1D velocity model because it has a RMS error of 0.399 s, which is lower than an RMS of 0.433 s derived from the starting model (black dashed lines, Fig. 4.5), and is also lower than the RMS of the other final models. When compared to the starting model, the final velocity model is slower in its shallowest portions, and faster than the starting model from 5 to 15 km depth (Fig. 4.5). The output favoured best-fit velocity model of Vp and Vs is also displayed in Tab. 4.1, where the number of hypocenters in each layer (NHYP) and the number of rays passing through each layer (NHIT) are reported. In Table 4.1 one can notice that the Vp/Vs ratio of each layer remains in the range of 1.74 - 1.83. This model was used as one of the starting models for the 3D tomography and is referred to as velest velocity model hereinafter.

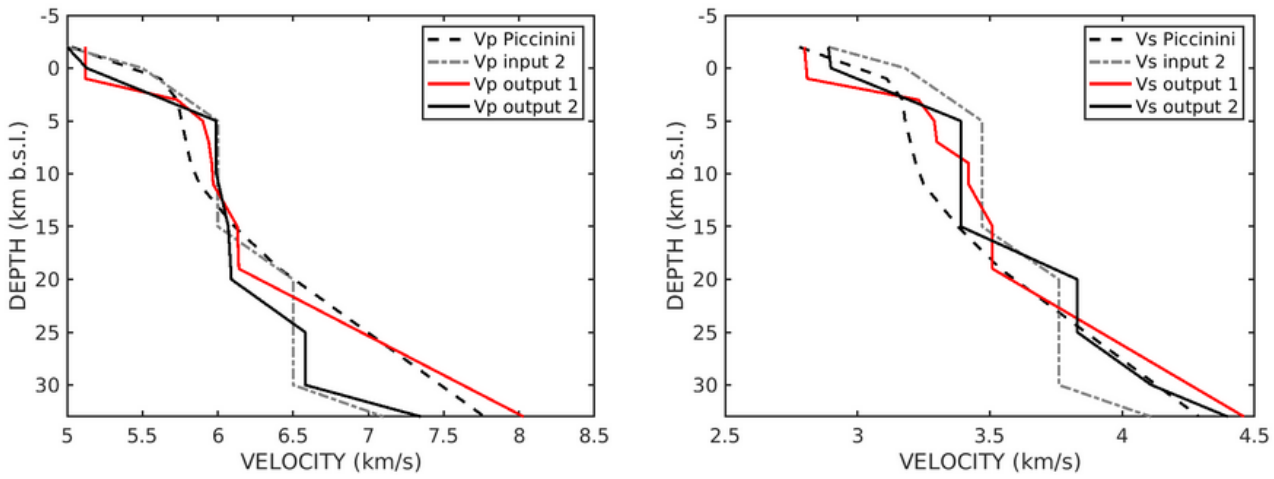


Figure 4.5: 1D velocity model for Vp (on the left) and Vs (on the right). The final velocity models are represented with the red lines. The black one is the output of Velest using a different starting model. The dashed lines represent the starting models.

Top (km)	Bottom (km)	NHYP	NHIT	Vp	Vs	Vp/Vs
-2.00	1.00	5	48067	5.12	2.80	1.83
1.00	3.00	78	49894	5.12	2.81	1.82
3.00	5.00	65	49316	5.73	3.23	1.77
5.00	7.00	203	46354	5.90	3.29	1.79
7.00	9.00	418	41803	5.94	3.30	1.80
9.00	11.00	272	30217	5.96	3.42	1.74
11.00	15.00	322	21536	5.97	3.42	1.75
15.00	19.00	114	12914	6.13	3.51	1.75
19.00	33.00	292	9428	6.14	3.51	1.75
33.00	-	0	0	8.03	4.46	1.80

Table 4.1: Velocity model deriving from Velest inversion of the selected subset of 1796 events. For each layer is specified the number of hypocenters and the number of rays passed through.

4.3 Local Earthquake Tomography (LET)

LET consists of the inversion of local earthquake travel time data for solving the joint problem of hypocenter location and velocity structure determination. It has been used to analyse the lithosphere and upper asthenosphere to depths up to 200 km in a variety of geodynamic context (Abers, 1994; Graeber and Asch, 1999; Rawlinson and Sambridge, 2003) and can potentially help reveal the mechanisms that control tectonic processes (Koulakov 2009). In seismic tomography the subsurface structure is represented by variations in P- and S- wave velocity, parameterizing the volume with a set of constant velocity blocks or nodes with a specified interpolation function, or a combination of velocity and interface parameters (Rawlinson and Sambridge, 2003). The tomographic method depends on the general principles of inverse theory (Tarantola, 1987; Menke, 1989; Parker, 1994; Sambridge, 1999). In this case, the data are earthquake source to receiver traveltimes and the model parameters define the subsurface velocity variations (Sambridge, 1999).

The inverse problem thus consists of retrieving those model parameters which minimize the difference between observed and predicted data (Sambridge, 1999).

The nature of the tomographic inverse problem is ill-posed; in other words, multiple solutions may explain the observations, which implies that the solution uniqueness is not guaranteed (Rawlinson et al., 2014, 2016). A further aspect to be investigated is the resolution of the solution, that means the ability of the method to resolve heterogeneities of variable size and intensity. The common methods for assessing solution robustness are the synthetic reconstruction tests, the most widespread of which uses the checkerboard model (Spakman and Nolet, 1988). This consists of a regular alternating pattern of positive and negative anomalies along each spatial dimension of the model (Rawlinson *et al.*, 2014) (Fig. 4.6b). Another test commonly used is the spike test (Walck & Clayton, 1987) in which the synthetic model contains one or more short-wavelength anomalies (Rawlinson *et al.*, 2014) (Fig. 4.6a).

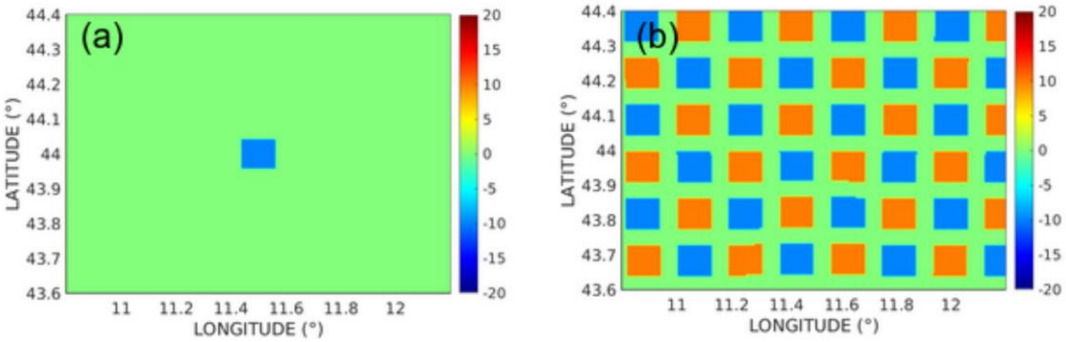


Figure 4.6: Examples of the synthetic reconstruction tests: a) the spike model; b) the checkerboard model. The colour is the percentage of change with respect to the input model.

Furthermore, local earthquake tomography needs a dense ray coverage of the target volume (a function of the source–receiver distribution) to obtain a good resolution of the results (Evans et al., 1994; Luckett and Baptie, 2015). This means not only a reasonable distribution of earthquakes, which must be distributed within the whole area and at different depths, but also a good coverage of the area by seismic stations.

4.3.1 Data and input starting velocity model

The data consist of the travel times from the merged archive dataset for 2005-2019 obtained in Chapter 1, integrated with the data from 2019-2021 retrieved from both the INGV and 9M stations.

Regarding the 9M data, I manually picked those earthquakes from the INGV bulletin that had also been recorded by the temporary stations. In particular, I considered the earthquakes of the INGV bulletin with magnitude greater than 2 located within the black area used in Chapter 2. Then, I used the origin time of those earthquakes to cut the continuous data streams from the 9M network. Then, I picked the P and S phases of the earthquakes for each station of the 9M network using the Seismic Analysis Code (SAC, hereinafter; Goldstein and Snoke, 2005; Goldstein et al., 2003), which is an interactive program designed for the study of time series, with particular reference to seismic signals.

The total number of stations is 75. I selected the 1757 events with at least 20 arrival times, including at least 10 S-arrivals, considering the phases with absolute station residual smaller than 1s and picking uncertainty lower than 0.1s.

Similar to that described above for deriving the minimum 1D velocity model, the 3D tomography starts with the use of a 1D input starting velocity model. Given the non-linearity of the inversion problem and the dependency on the input model, I verified the influence of the input model by repeating the inversion using two different input models. The first is a velocity model obtained simplifying the one from Piccinini et al. (2014) and with a Vp/Vs ratio of 1.73 (*model1*, hereinafter; black lines in Fig. 4.7 and Table 4.2), and the other is the Velest velocity model, that is the best-fit velocity model calculated with velest with a variable Vp/Vs ratio for each layer in section 4.1 (*model2* hereinafter; red lines in Fig. 4.7 and Table 4.3).

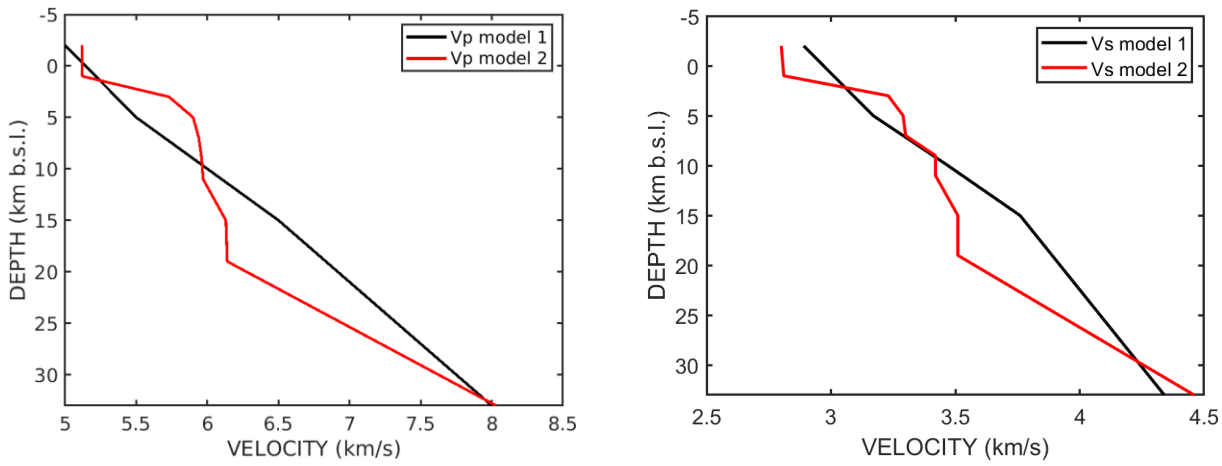


Figure 4.7: Starting velocity model for P- and S-waves. In black the modified Piccinini velocity model (Table 4.2). In red the velest velocity model obtained in the previous section (Table 4.3).

Depth	Vp	Vs	Vp/Vs
-2.00	5.0	2.89	1.73
5.00	5.5	3.17	1.73
10.00	6.0	3.47	1.73
15.00	6.5	3.76	1.73
32.00	8.0	4.62	1.73

Table 4.2: starting velocity model 1

Depth	Vp	Vs	Vp/Vs
-2.00	5.12	2.80	1.83
1.00	5.12	2.81	1.82
3.00	5.73	3.23	1.77
5.00	5.90	3.29	1.79

7.00	5.94	3.30	1.80
9.00	5.96	3.42	1.74
11.00	5.97	3.42	1.75
15.00	6.13	3.51	1.75
19.00	6.14	3.51	1.75
33.00	8.03	4.46	1.80

Table 4.3: starting velocity model 2, which is obtained from Velest.

4.3.2 Method

To perform the 3D tomography I used the algorithm LOTOS (Local Tomography Software) by Koulakov (2009). This computer code is designed for simultaneous inversion for P- and S-wave velocity structures and source coordinates (Koulakov, 2009). The information defined by the user are the starting velocity model, the parameters for the inversion such as smoothing and damping, grid construction of the subsurface model, number of iterations for the inversion. There are some advantages in using LOTOS with respect to other software: 1) the algorithm uses the minimal input information (arrival times and coordinates of stations); 2) the synthetic reconstructions use the same input files and the same program steps as in the case of real data processing; 3) the influence of the parametrization on the result is reduced, because the final result is obtained from the average of the individual inversions performed over grids of different orientations; 4) it permits the possibility to choose node or cell parametrization. Another characteristic of LOTOS is the solution of the forward problem (i.e., ray tracing and travel-time calculation) using a modified version of the bending algorithm, which is based on the Fermat principle of travel time minimization (Um and Thurber, 1987).

The first step of the LOTOS computer code is the optional optimization of the 1D velocity model, and the preliminary source location. Then, using the bending algorithm the rays are traced through a 3D extrapolation of the 1D model. For locating in the 3D model, LOTOS uses a gradient method (Koulakov et al. 2006), that is as robust as a grid search method, but is much faster (Koulakov 2009). In figure 4.8 I illustrate the flowchart of the main program steps of the 3D iterative tomographic inversion as reported in Koulakov (2009). The evaluation of P and S anomalies in nodes or blocks is performed over the same grid but with different orientation. Then, the results are combined to obtain a P and S velocity anomaly model in a regular 3D grid.

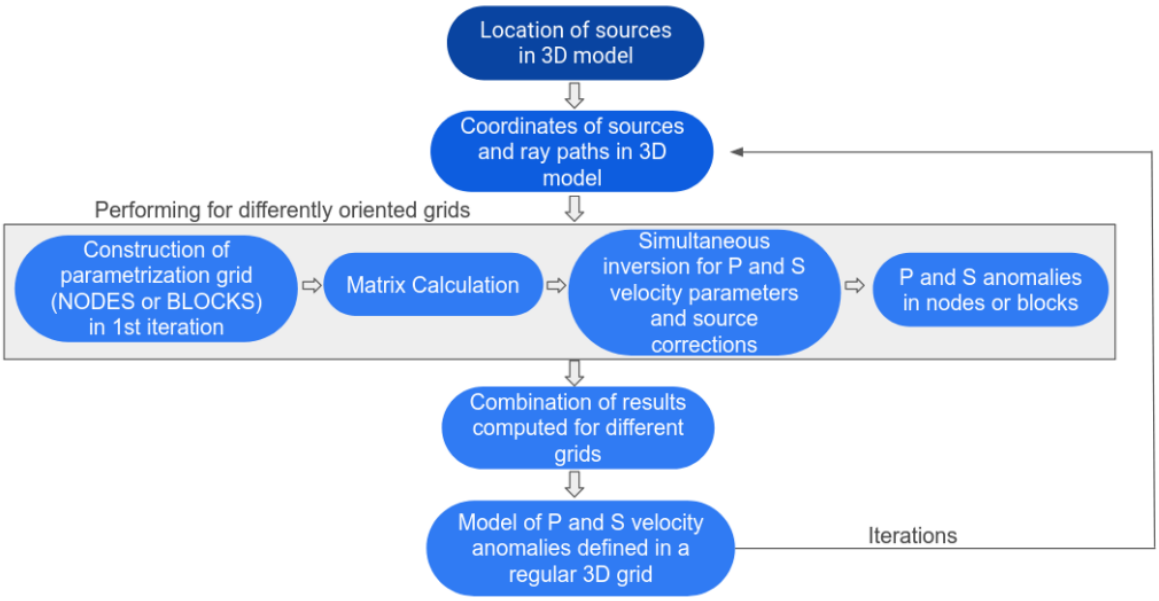


Figure 4.8: Flowchart of the program steps of the 3D iterative tomographic inversion of LOTOS.

Concerning the construction of the parametrization grid, the code uses a mesh of nodes that are positioned within the study volume in vertical lines using a method described in Koulakov et al. (2006). The nodes are distributed according to the ray density, and the velocity distribution between them is approximated linearly.

The matrix calculation refers to the first derivative matrix $A_{ij} = \partial t_i / \partial v_i$ that is evaluated using the ray paths in the 3D model and is equal to the time variation along the i-th ray due to a infinitesimal velocity perturbation in the j-th node/block. The inversion of the matrix is performed using an iterative LSQR code (Page and Saunders, 1982; Van der Sluis and Van der Vorst, 1987).

The resolution and reliability of tomographic inversion are controlled by the inversion parameters and the ray coverage of the investigated volume. The inversion parameters are the smoothing coefficient and the amplitude damping. The smoothing coefficient controls the smoothness of the solution. It reduces the difference between solutions in neighboring nodes, resulting in smoothing of the computed velocity fields. The amplitude damping controls the amplitude of the derived P or S velocity anomalies. To evaluate the optimal values for the inversion parameters I used the trade off curve method, which presents the data variance versus model variance computed for different smoothing or damping parameters. The resulting curve is generally a L-shaped curve, hence it is called L curve. So, the ideal smoothing/damping value is at the corner of the resulting L curve, beyond which increases in data variance do not correspond to a significant decrease in model variance, and vice versa.

I evaluated the smoothing and damping parameters by performing spike tests and using as the starting model the velocity *model 1*. The spike tests were also used to assess which is the smallest resolvable anomaly of the inversion.

Once the inversion parameters are fixed, in order to verify the independence of the results from the input velocity model, I performed the spike and checkerboard tests, and the real data inversions using the two different velocity models aforementioned as input model.

4.3.3 Results

In this section I show the results divided in 3 subsections. First, I present the distribution of the ray paths within the study volume. Second, I deal with the resolution tests for two different aims. I used the spike tests to constrain the value of the inversion parameters and to evaluate the minimum anomaly resolvable with the parametrization used in the analysis. Then, I used the spike and the checkerboard tests to constrain the resolution and the reliability of the tomographic inversion regarding depth and intensity of the anomalies. Furthermore, I compared the solutions of the synthetic reconstruction tests obtained using the two different starting models. In the end, I show the results of the real data inversions performed using the two starting models in order to verify the independence of the result from the input model.

4.2.3.1 Distribution of the ray paths within the investigated volume

Figure 4.9 shows the ray coverage of the study area for different depths: a) 5 km, b) 10 km, c) 15 km, d) 20 km. The red squares represent the nodes of the grid where the velocity is retrieved. In correspondence to the blank spaces, where no nodes are positioned as a consequence of poor or absent ray coverage, the code doesn't calculate any velocity. In Figure 4.10 I illustrate rays and inversion nodes along several cross-sections (the traces of the cross sections are shown in Figure 4.16c), in order to better investigate the extent of the regions covered by the inversion grid nodes. Different areas have different limits in resolution at different depths. In cross-section 1 the nodes extend down to 50 km depth, whereas for cross-sections 2 and 4 the nodes extend down to 40 km, and for cross-section 3 the velocity inversion is conducted down to 30 km depth.

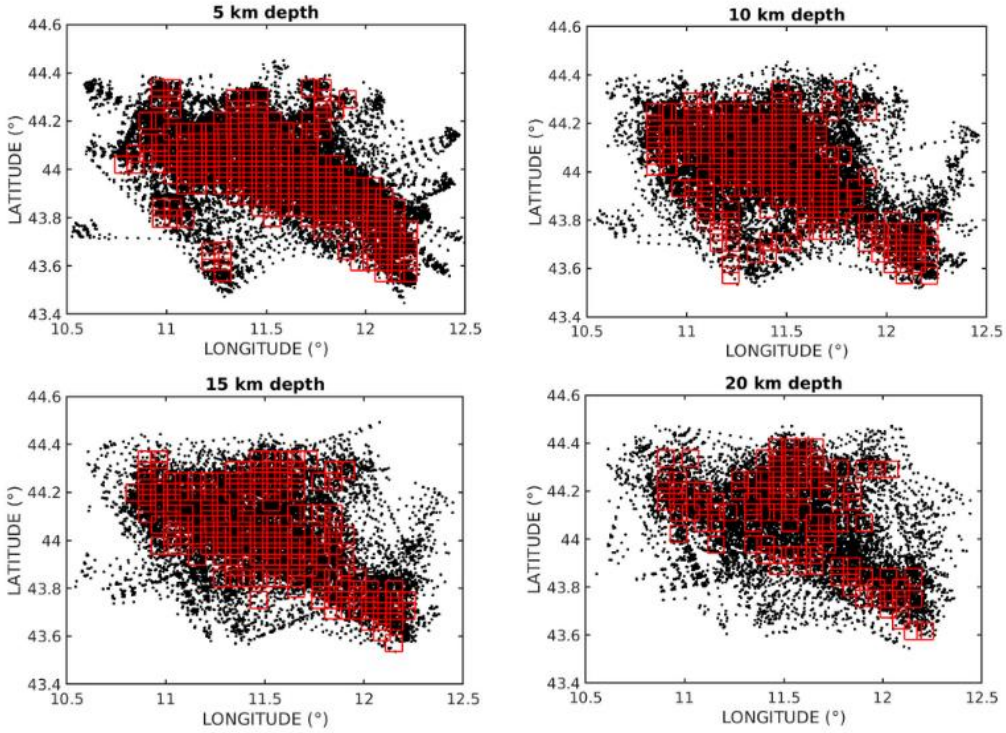


Figure 4.9: Horizontal slices of ray paths (black dotted lines) and nodes (red squares) coverage of the study area for different depths: a) 5 km; b) 10 km; c) 15 km; d) 20 km.

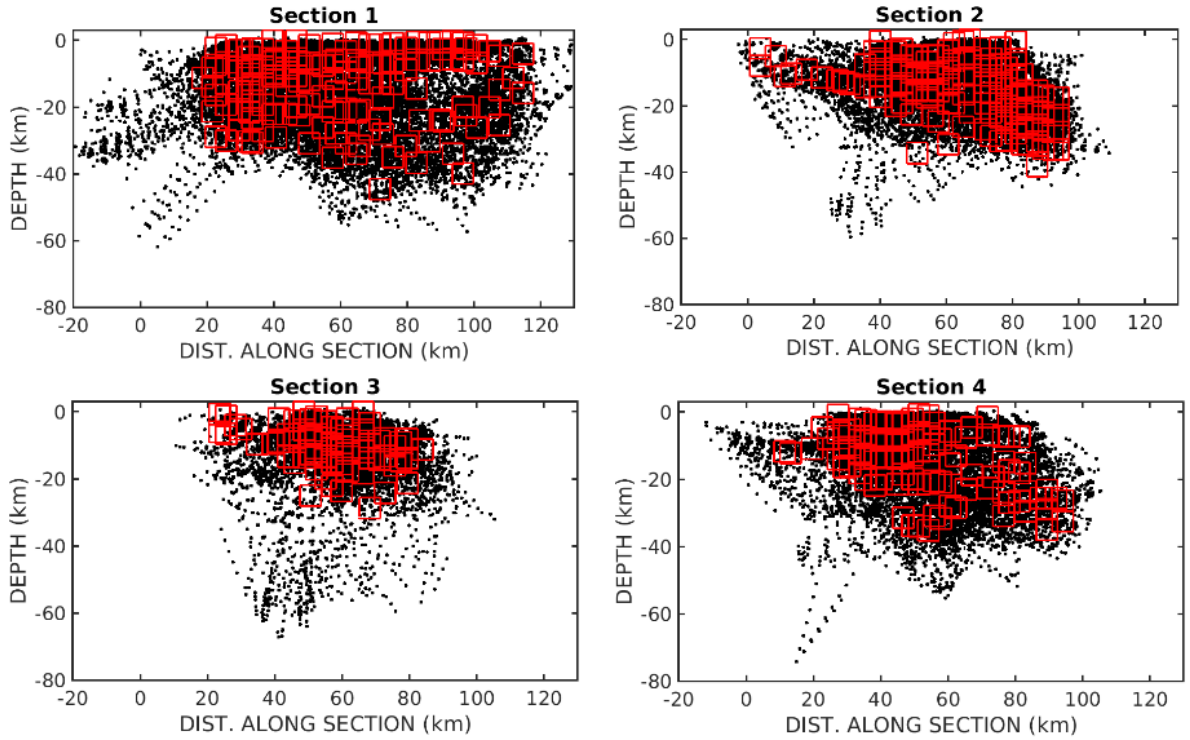


Figure 4.10: The cross-sections showing ray paths (black dotted lines) and nodes (red squares) coverage of the study area. The traces of the different cross sections are shown in Figure 4.16c.

4.2.3.2 Synthetic reconstruction tests

Spike Tests

Number of iterations, Grid Size. To evaluate the optimal grid size and number of iterations I performed a number of inversions using the spike model shown in Figure 4.13, with a velocity anomaly of 10% with respect to the background model. Furthermore, I repeated the inversions over 4 different angles of orientation of the grid, namely 0°, 22°, 45° and 67°. I tested grid spacings of 15, 10 and 5 km, and different numbers of iterations ranging from 1 to 7. The choice of the optimal parameters is based upon the final RMS and the average deviation of the anomaly, that is the L_2 norm of the model parameters. From those results (not shown here) I found that the optimal parameters are a grid size of 5km, and a number of iterations equal to 5.

Damping Factor. In order to assess the best value for the amplitude damping, I computed other spike tests keeping the values of the smoothing coefficient fixed and varying the damping factor. For P- and S-waves the smoothing factors are set equal to 0.5 and 1, respectively. In Figure 4.11 I show the diagrams of the final RMS against the average deviation anomaly of the tests (*trade-off* curves). Those curves indicate that the optimal values of the amplitude damping for the P- and S-waves are 1.5 and 2, respectively. Those values are thus used in the subsequent analysis.

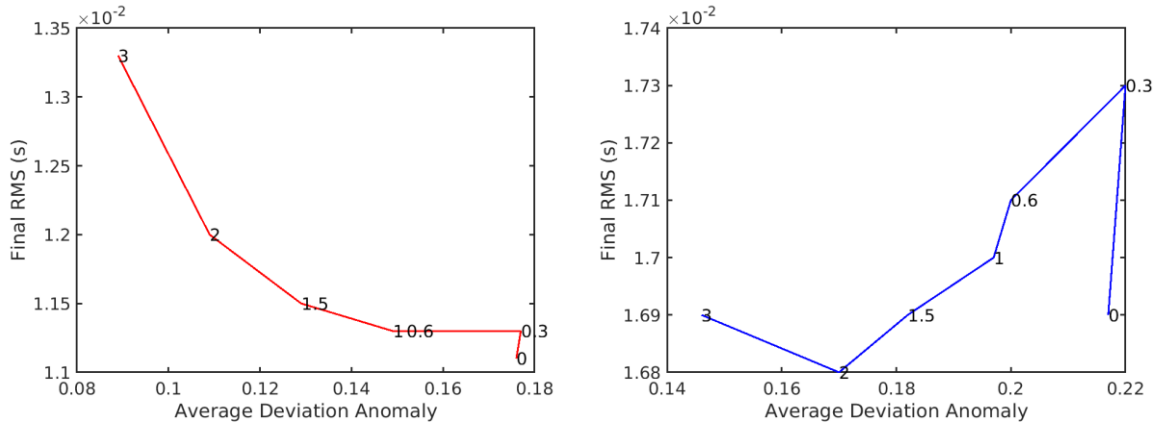


Figure 4.11: Results of the spike tests performed with the smoothing coefficients fixed (for P-waves is 0.5, for S-waves is 1). The values along the lines indicate the different amplitude damping.

Smoothing Coefficients. Then, I performed the spike tests keeping fixed the damping parameters to the optimal values retrieved above, and varying the smoothing coefficients. In this case, the optimal values for the smoothing coefficients are 1 for P-waves and 2 for S-waves (Fig. 4.12).

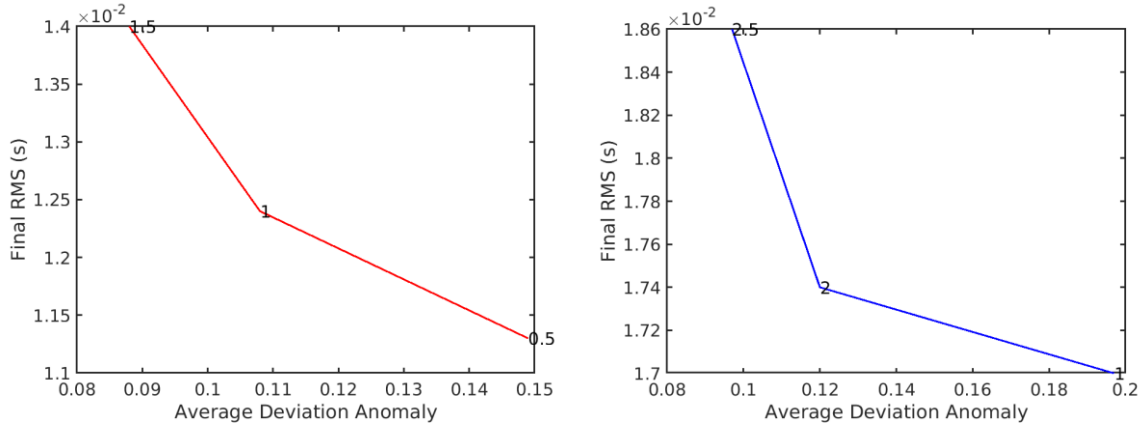


Figure 4.12: Results of the spike tests performed with the amplitude damping fixed (1 for P-waves, 2 for S-waves). The values along the lines are the smoothing coefficients.

Using the optimal values of the inversion parameters, I then computed other spike tests varying the size of the anomaly (Fig. 4.13). Figure 4.13 reports the results of the inversions using anomalies of different size: b) 10 km; c) 7.5 km; d) 5 km. From the figure it emerges clearly that the smallest resolvable anomaly with good amplitude recovery is of 10 km. At smaller anomaly sizes of 7.5 km and 5 km the presence of the anomaly is retrieved, but its shape and amplitude are poorly resolved.

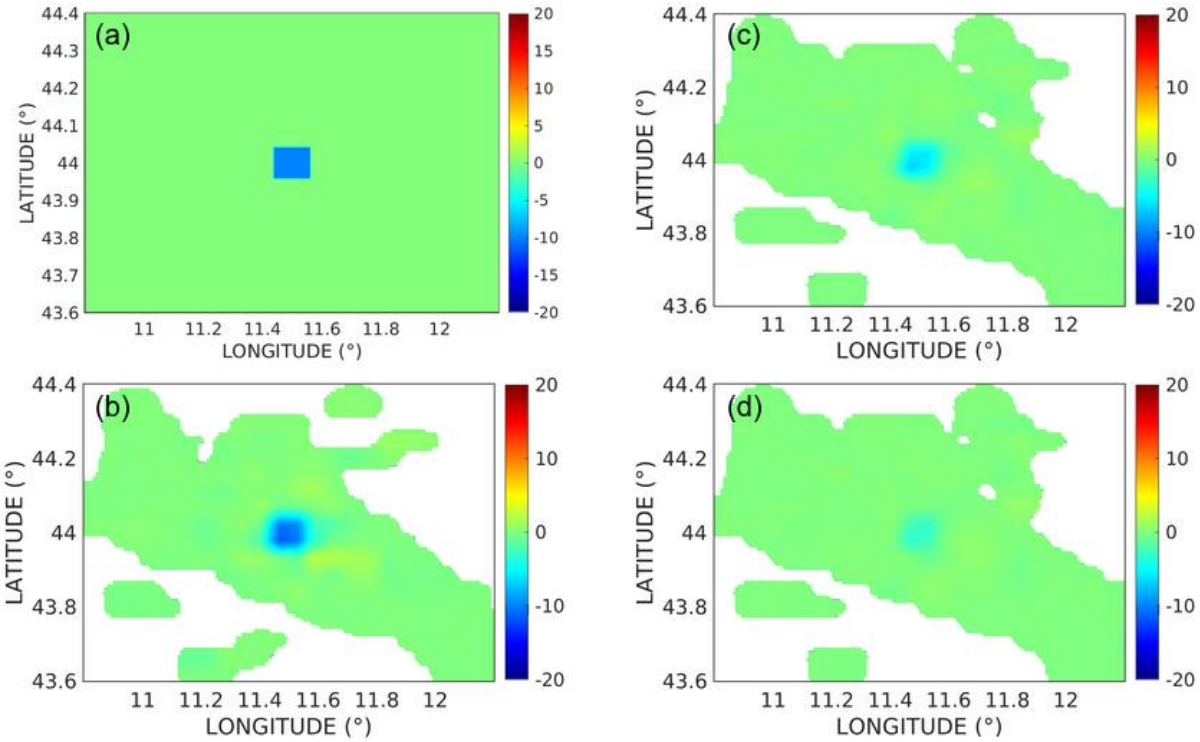


Figure 4.13: a) Example of the synthetic input model using a 10 km anomaly with 10% decrease of velocity. The results of the inversion computed using different sizes of anomaly, the size for each panel is: b) 10 km; c) 7.5 km; d) 5 km. The smallest anomaly that is well resolved in shape and amplitude is 10 km wide.

I now proceed to evaluate the sensitivity of the inversion to the starting velocity model. To perform this test, I repeat the spike and checkerboard tests using two different input models.

In Figure 4.14 and 4.15 I show the result of the spike tests conducted using input velocity *models 1* and *2*. The retrieved velocity model is shown on the horizontal slice at 5 km depth (Fig. 4.14) and two vertical sections oriented NS and EW (Fig. 4.15). From these figures it is possible to observe that the actual anomalies are recovered in a similar manner in the 2 tests, with a minimal smearing in both cases. The output from *model 2* seems to have slightly larger background velocity variations away from the anomaly than the output from 1. As we can deduct from the vertical sections, the resolving power decreases with depth and below 20 km the resolution deteriorates. This is due to the fact that the majority of the earthquakes have a hypocenter above 25 km depth, so that ray coverage is very poor at depths larger than that limit.

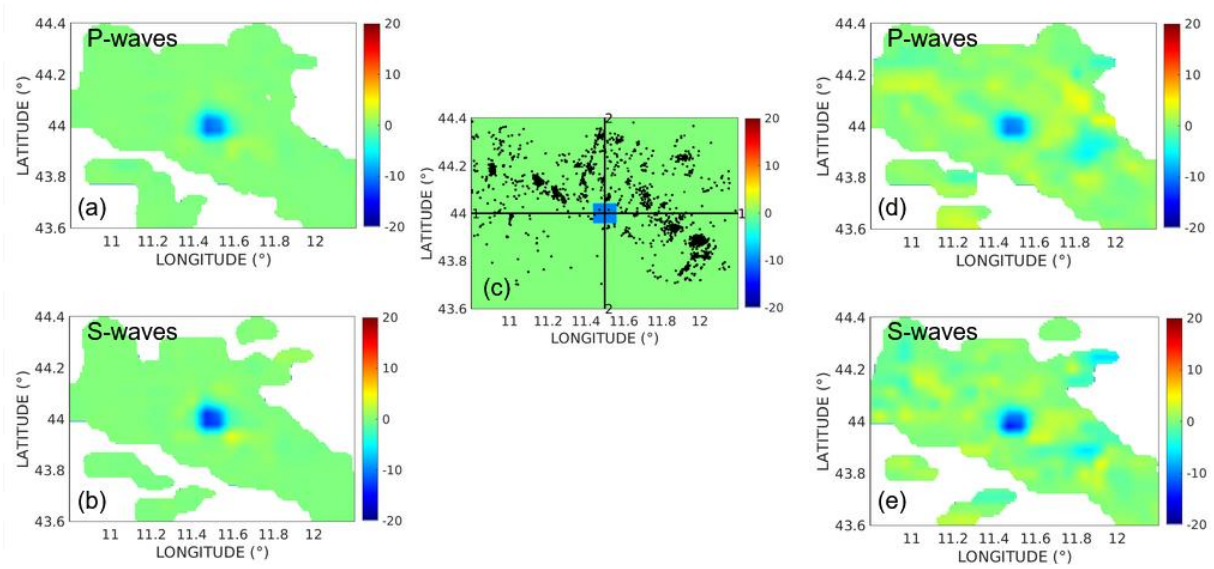


Figure 4.14: Horizontal slice at 5 km depth of the spike test computed for two starting models: on the left (a and b) velocity *model 1*; on the right (d and e) velocity *model 2*. The middle panel (c) shows the synthetic model and the distribution of sources. Results for P- and S-waves are reported in panels (a, d) and (b, e), respectively.

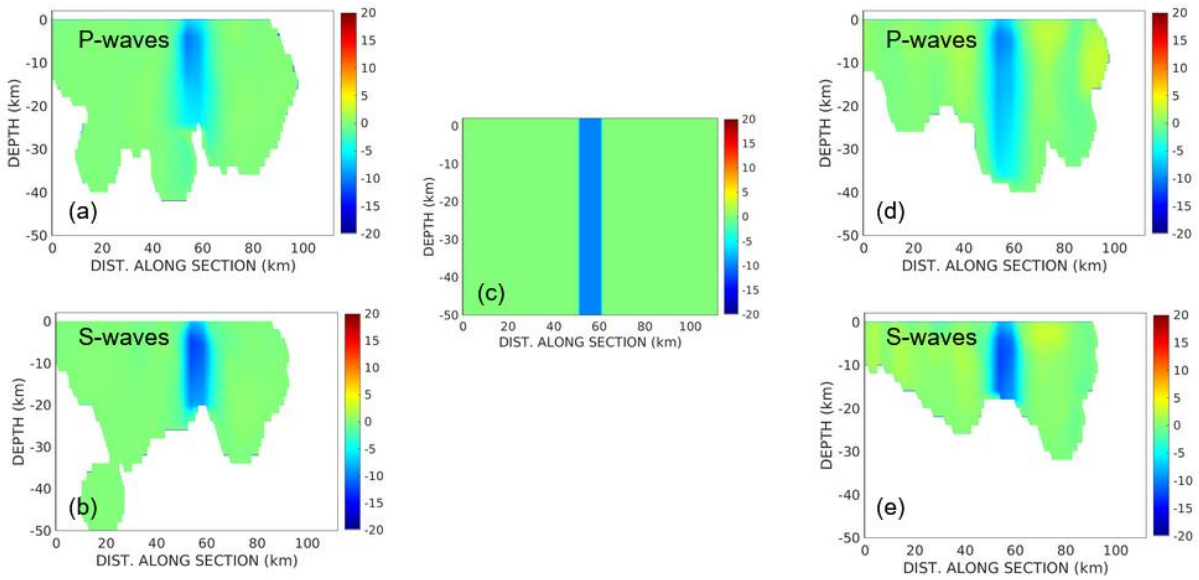


Figure 4.15: Vertical sections of the spike test computed for two starting models: on the left (a and b) the velocity *model 1*; on the right (d and e) the velocity *model 2*. The middle panel (c) shows the vertical section oriented EW of the synthetic model. Results for P- and S-waves are reported in panels (a, d) and S-waves (b, e), respectively.

Checkerboard tests

Proceeding in the analysis, I computed the checkerboard tests, using a synthetic model given by the alternance of positive and negative anomalies (see Figures 4.16, 4.17, 4.18). The anomalies have dimensions of 10 x 10 x 10 km, and an intensity of +/- 10% with respect to the background velocity; adjacent anomalies are separated by 5 km along the three dimensions. The horizontal slices at 5 km depth evidence that resolution is best at the center of the study area. The inversion performed

using velocity *model 1* exhibits significant smearing features in the eastern part of the study area that are not present in inversion from input velocity *model 2*. Regarding the vertical sections, in this case it is more difficult to assess the limits of resolution in depth. It is possible to see regions of the study area that are well constrained thanks to the presence of more earthquakes than in other regions. For both of the sections and starting model, there are two anomalies in the centre and north that are well detected, whereas the southern portion of the profile where earthquakes are lacking are less sharply resolved.

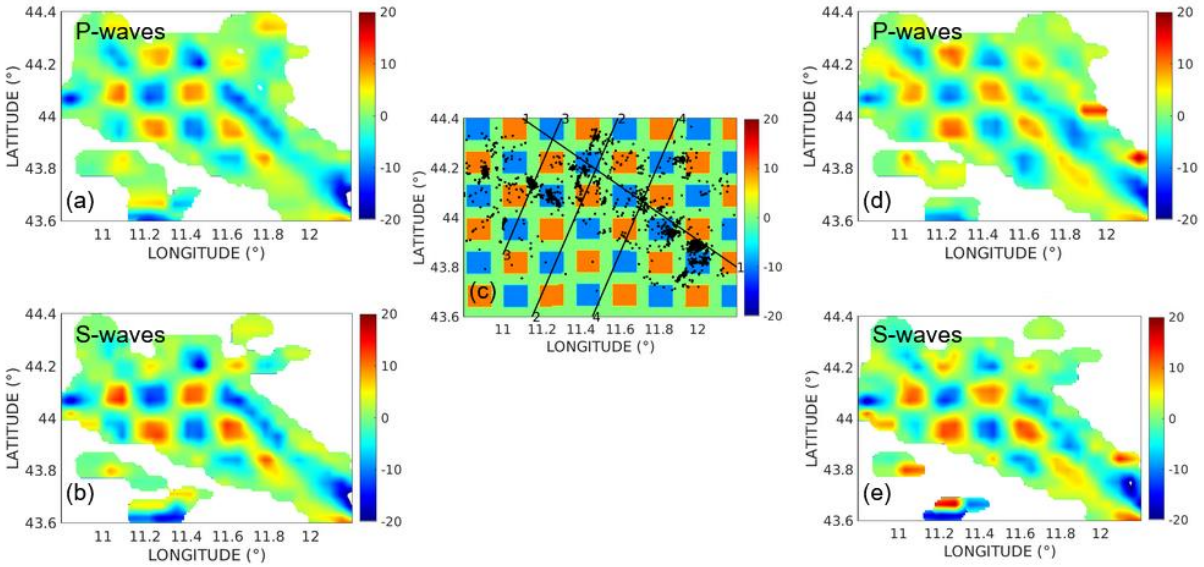


Figure 4.16: Horizontal results at 5 km depth of the checkerboard tests computed for two starting models: on the left (a and b) the velocity *model 1*; on the right (d and e) the velocity *model 2*. Panel (c) reports the horizontal slice of the synthetic checkerboard model at 5 km depth. Results for P- and S-waves are reported in panels (a, d) and S-waves (b, e), respectively.

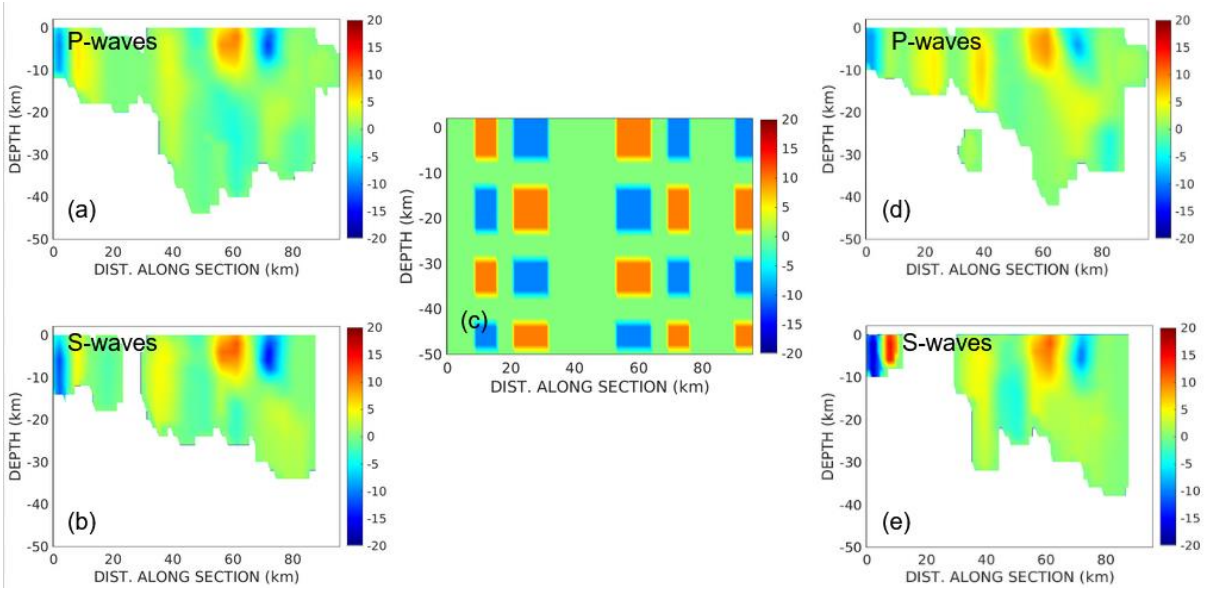


Figure 4.17: Vertical sections 2 of the checkerboard test computed for two starting models: on the left (a and b) the velocity *model 1*; on the right (d and e) the velocity *model 2*. The middle panel (c) reports the vertical section n. 2 of the retrieved velocity model. Results for P- and S-waves are reported in panels (a, d) and S-waves (b, e), respectively.

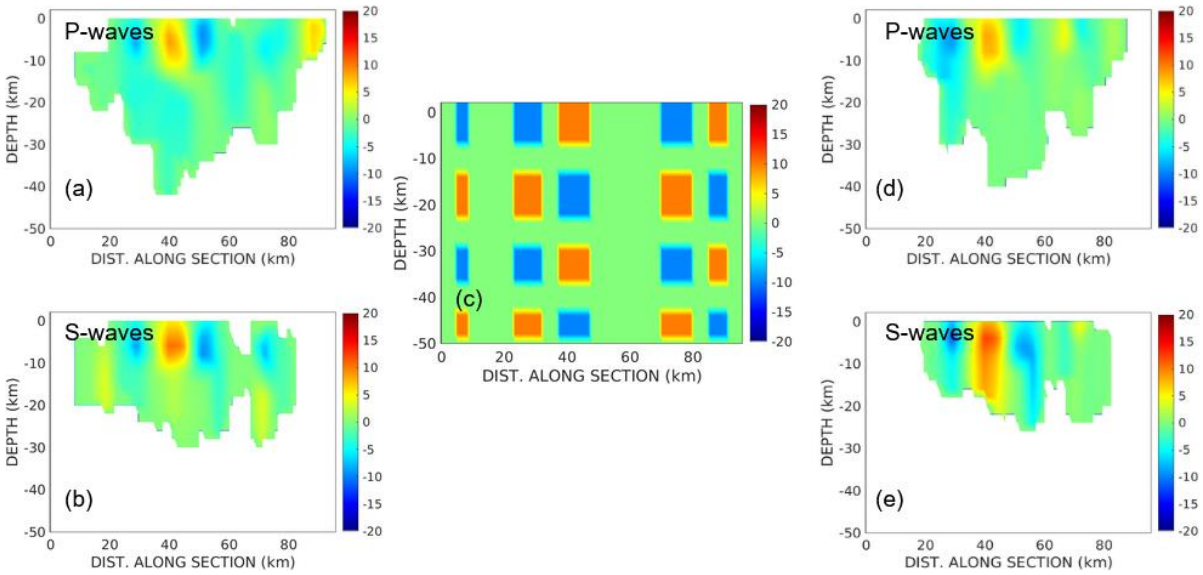


Figure 4.18: The same as in Figure 4.17, but for Vertical section 4.

4.4 3D Tomographic Inversion of real data

After selection of the optimal inversion parameters, I performed the real data inversions from both the 2 starting models used in the reconstruction tests. The horizontal slices at 5, 10, 15 and 20 km depth of the output velocity models are reported in Figures 4.19, 4.20, 4.21 and 4.22. The colorbar represents the percentage of change with respect to the starting velocity model. Figure 4.23 shows the topography of the study area.

Results obtained from the 2 starting models share the same main features. The main positive anomalies (i.e. higher velocity) in the Vp slices at 5 km depth are located mainly along the Apennine hinge, and in two NW-SE striking bands on the western side of the Apennines, including the surroundings of the Mugello basin. In the 10-km-depth slice the Vp images remain fairly similar to those at 5km, with the exception that the mid portion of the NW-SE striking positive anomaly bands is not as clearly observed. The main negative P-wave velocity anomalies are located on (i) the Adriatic foreland side of the Apennines, (ii) within the western side of Apennine hinge in between the positive anomalies mentioned above, and (iii) beneath the plain between the Apennines and the western coast. Going down to a depth of 20 km the two models show the same features: a negative velocity zone around the Mugello basin and including the Apennines to a positive velocity zone in the western part of the study area.

Even though the results from the 2 starting models share the same features, models derived from starting *model 1* exhibit velocity changes of up to ± 20%. Conversely, a closer inspection of the models from starting *model 2* shows that the amplitude of anomalies is far more subdued, with the vast majority of amplitude variations (at least at depths of 10km or more) concentrated within the ± 10% interval. For these same results, the sharper anomalies generally have small dimensions, and are confined on the edge of the investigated volume. Crustal seismic velocity anomalies of ± 10% are more in line with the kind of variation typically observed in tectonically active regions (e.g. as seen further south in the Apennines by Carannante et al., 2013). I therefore favour the models resultant from starting *model 2*.

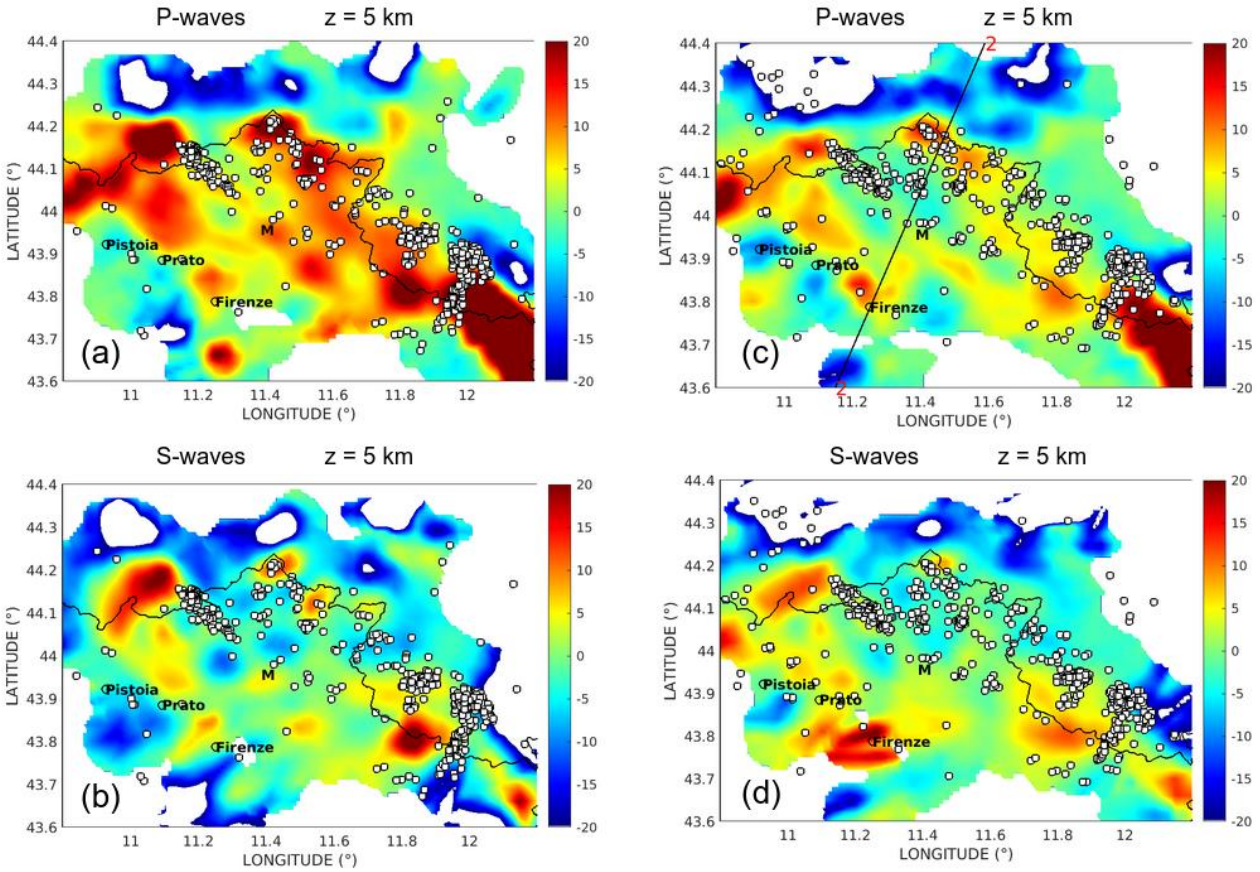


Figure 4.19: Horizontal slice at 5 km depth of the results from the tomographic inversion of the real data computed for two starting models: on the left (a and b) the velocity *model 1*; on the right (c and d) the velocity *model 2*. Results for the P- and S-waves are reported in panels (a, c) and (b, d), respectively. In panel c the trace of the vertical cross-section 2 is reported. The re-located earthquakes are represented with white dots.

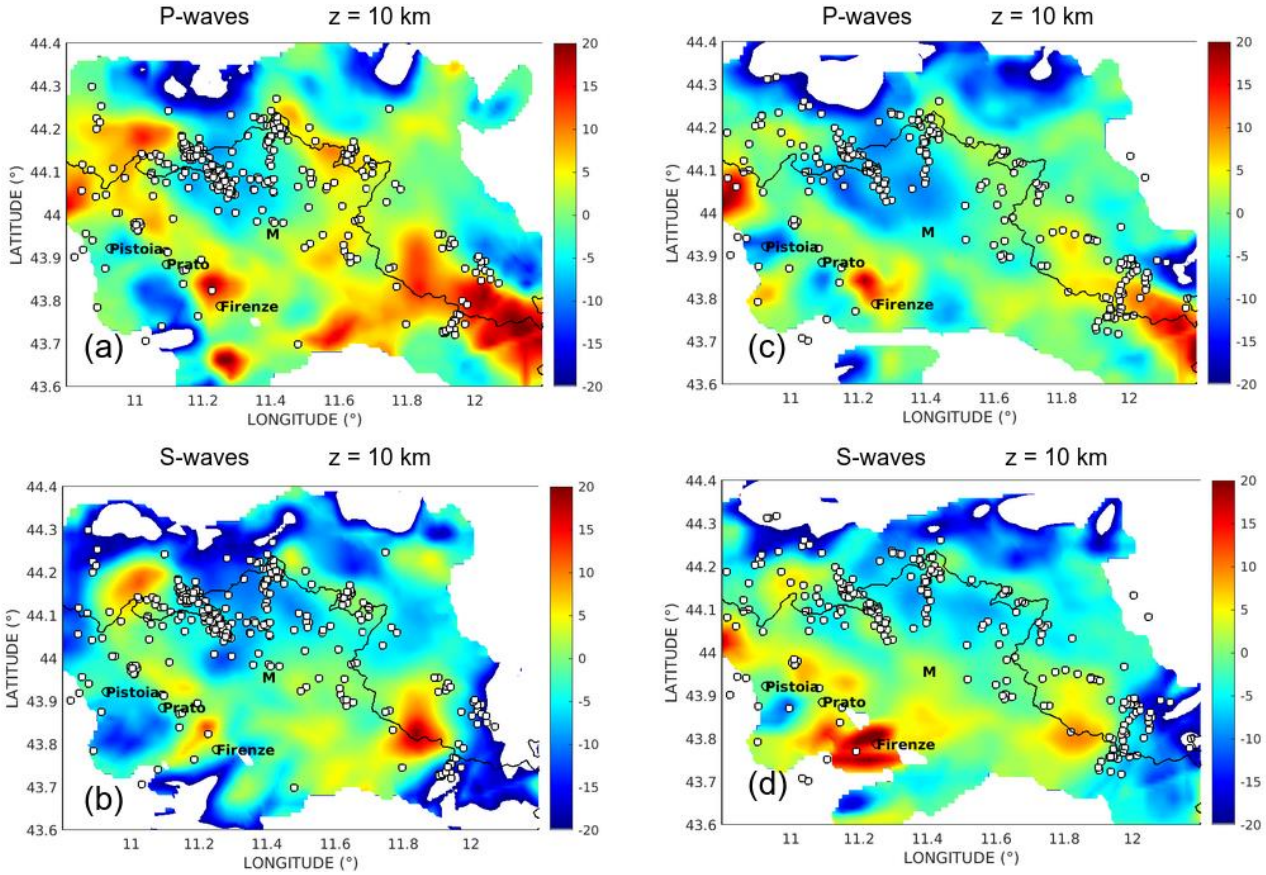


Figure 4.20: The same as in Figure 4.19, but for the horizontal slice at 10 km depth.

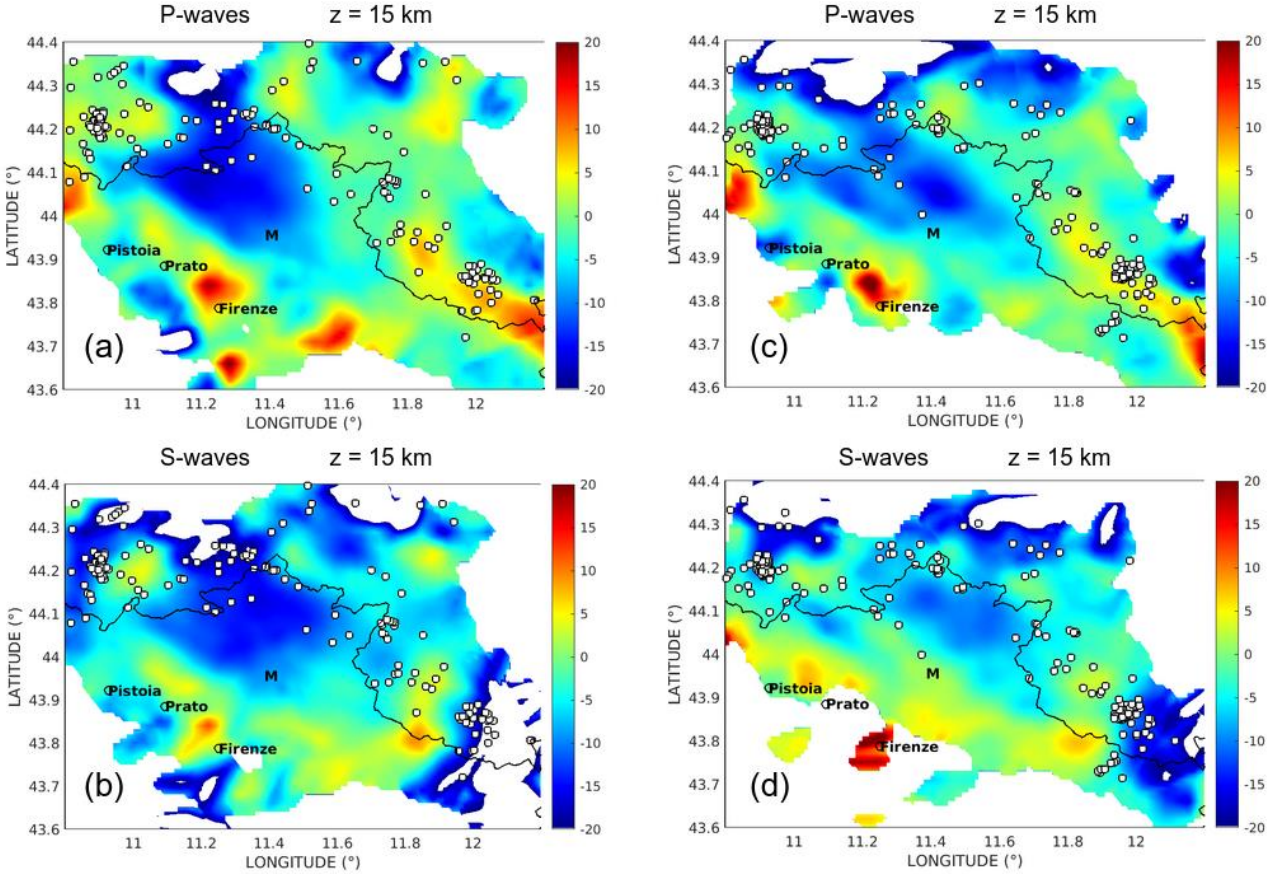


Figure 4.21: The same as in Figure 4.19, but for the horizontal slice at 15 km depth.

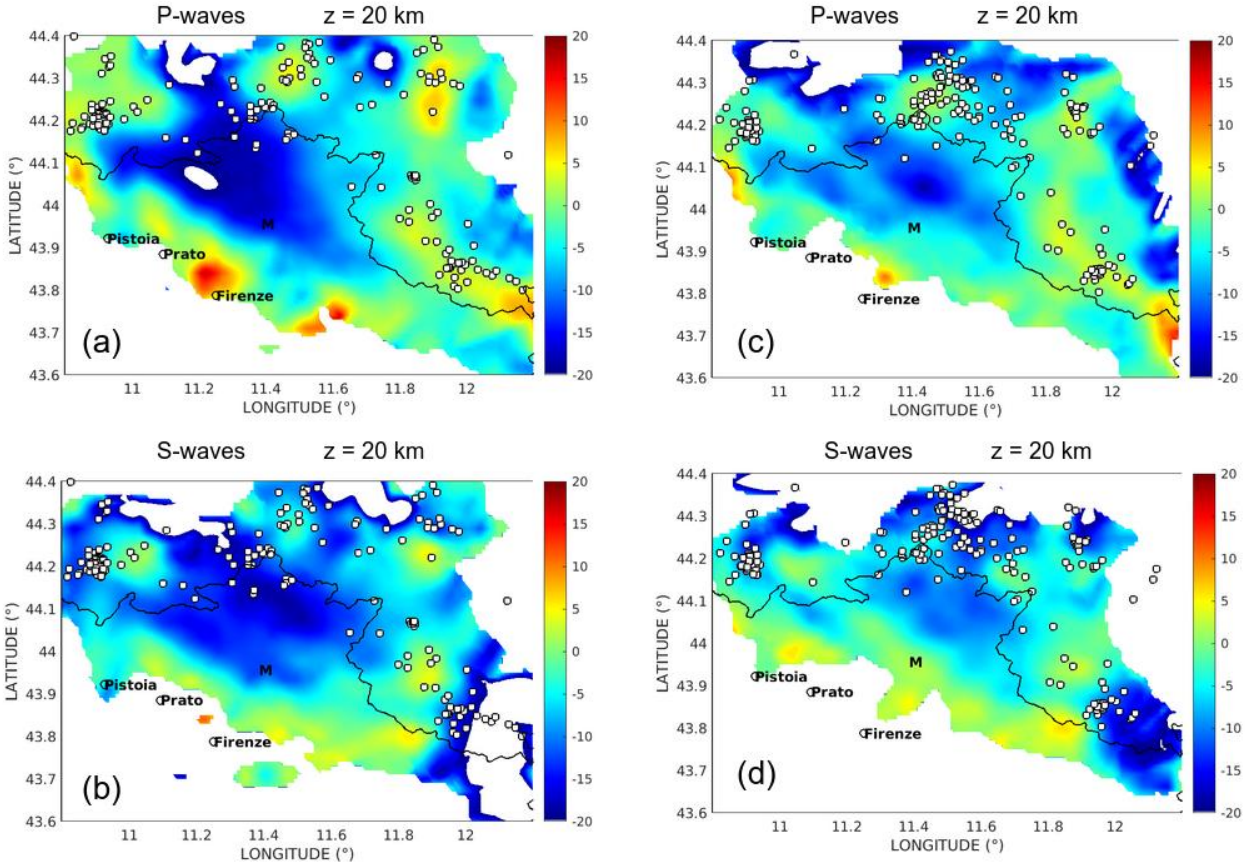


Figure 4.22: The same as in Figure 4.19, but for the horizontal slice at 20 km depth.

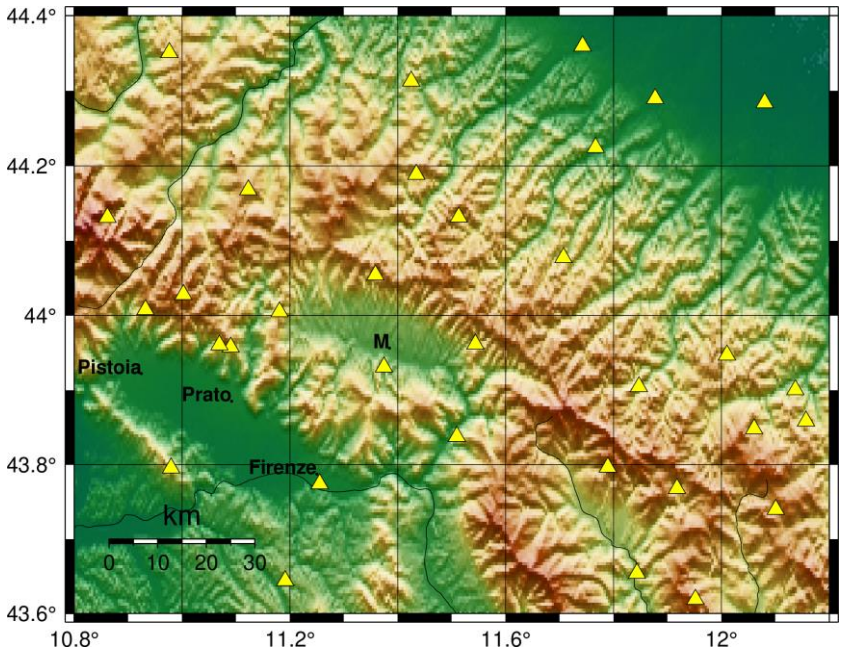


Figure 4.23: Topography of the study area. The Mugello basin is represented by the area sorrounding the letter M. The yellow triangles represent the seismic stations.

Figure 4.24 illustrates the output velocity models along the vertical cross-section n.2. The most striking features are the spatial changes in depth to fast velocity contours such as ~7-8 km/s. The transitions to such fast velocities are broadly deeper (30-35 km) beneath the Apennines, and shallower (~25 km) beneath the Adriatic foreland and shallowest (~20 km) at the western side of the profile. However, exceptions to this are shorter wavelength and fast velocity anomalies up to 5-km-deep beneath the Apennine hinge and to 10-km-deep beneath the western edge of the Apennines near Florence. This characteristic is common to the results obtained from the 2 starting models, and broadly replicated in the S-wave speed images as well, though of course the absolute velocities are slower in the S wave images.

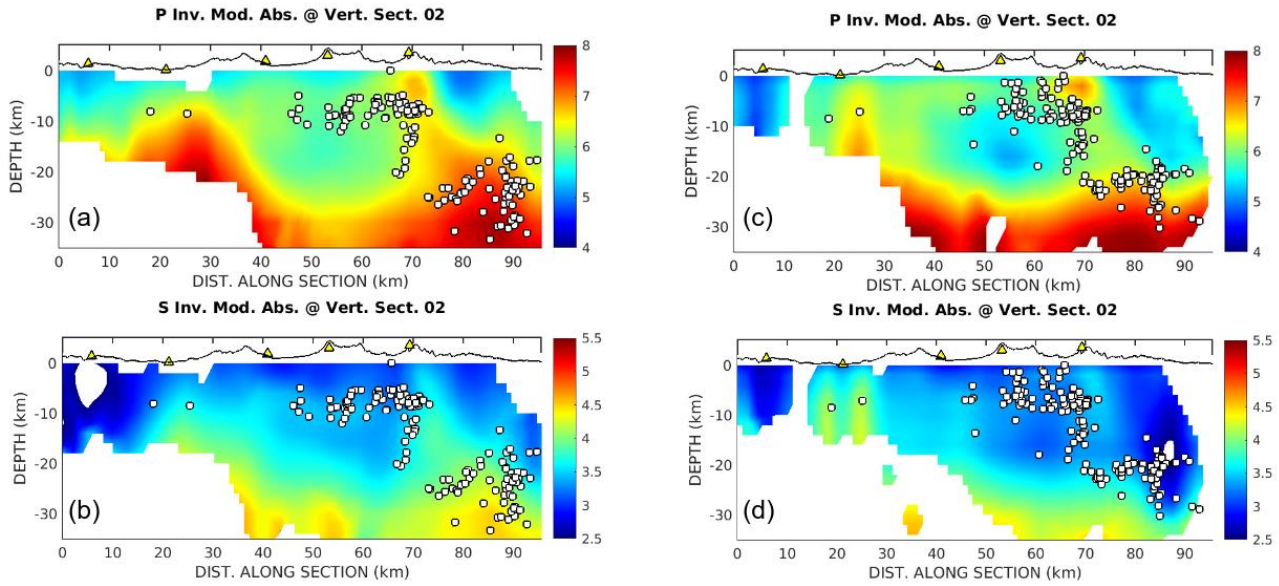


Figure 4.24: Vertical cross-section 2 of the real data inversion computed for two starting models: on the left (a and b) the velocity *model 1* (P and S respectively); on the right (d and e) the velocity *model 2* (P and S respectively). The relocated events are represented with white dots. The elevation of the topography is exaggerated by a factor 5.

The Vp/Vs values from the two models are quite similar, even if in the *model1* there are more high features (Vp/Vs ~ 1.9) around the Mugello basin at 5 km depth (Fig. 4.25). The Mugello basin for the two models has a Vp/Vs around 1.8, but for the *model2* it is extended to the nearby area. Along the Apennines the Vp/Vs is higher with values up to 2. In deeper slices the Vp/Vs decrease especially in the area of the basin for both the models, and it is around 1.6 - 1.65, even if the *model 2* shows some unresolved zones (Fig. 4.26, 4.27, 4.28).

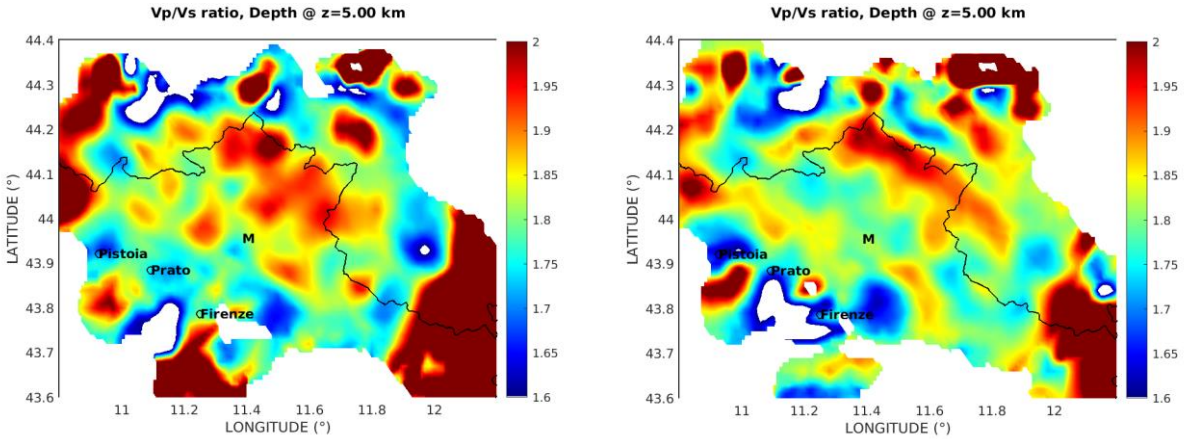


Figure 4.25: Horizontal slice at 5 km depth of the Vp/Vs ratio resulted from the tomographic inversion of the real data computed for starting *models 1* and *2* (left and right panel, respectively).

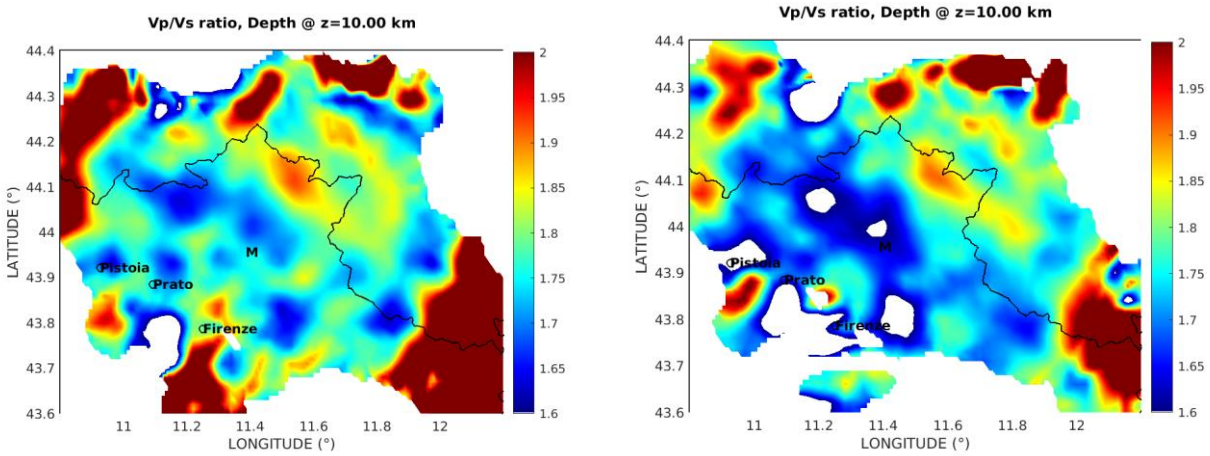


Figure 4.26: The same as in Figure 4.25, but for the horizontal slice at depth 10 km.

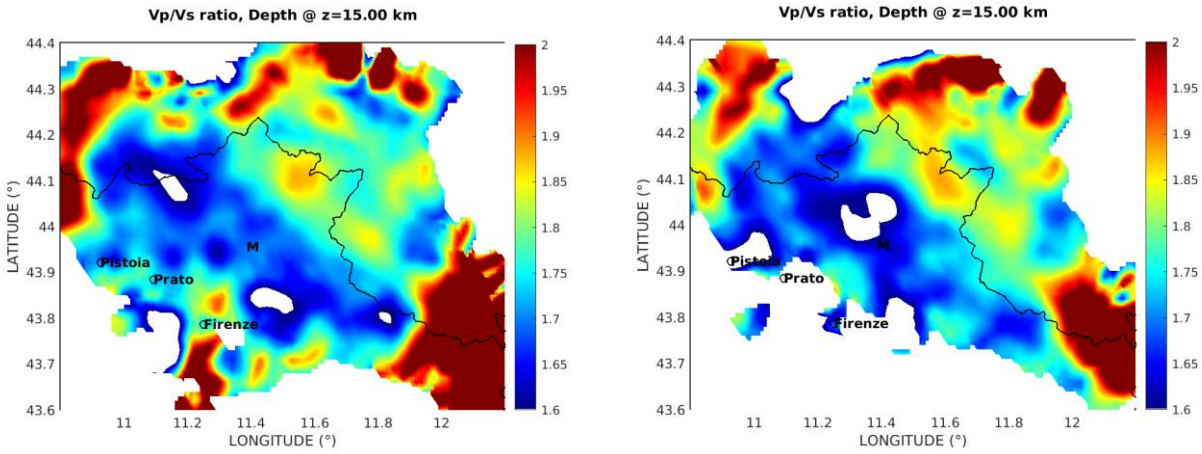


Figure 4.27: The same as in Figure 4.25, but for the horizontal slice at depth 15 km.

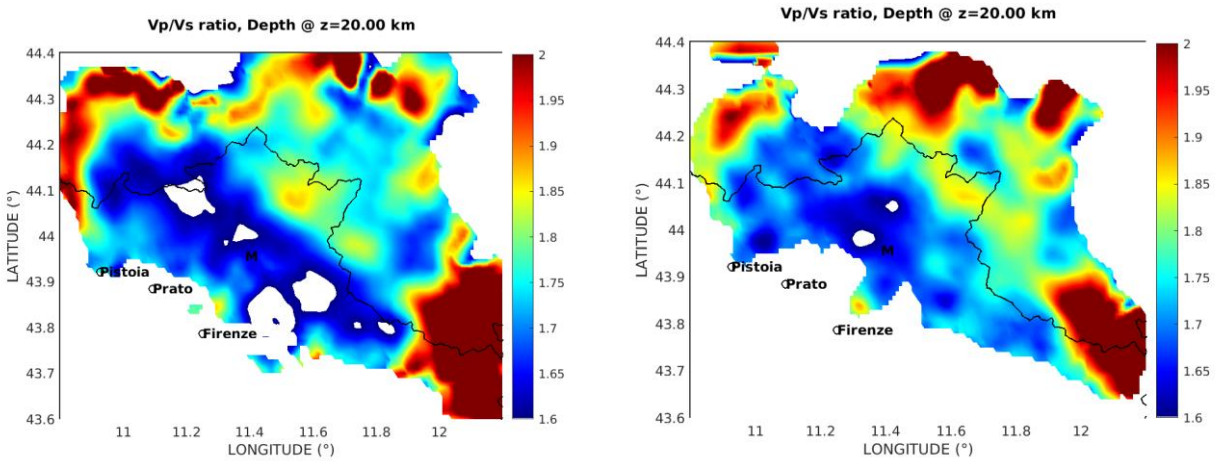


Figure 4.28: The same as in Figure 4.25, but for the horizontal slice at depth 20 km.

4.5 Interpretation

At crustal depths, the majority of the image is characterised by seismic velocities between 5.5 km/s at the surface to around 6.5 km/s in the lower crust (Fig. 4.24). Such velocities are typical of continental crust globally (Christensen and Mooney, 1995), and consistent with previous results derived from LET studies conducted over a wider region (Scafidi and Solarino, 2012), and an adjacent portion of the belt (Carannante et al., 2013).

The Moho discontinuity is likely represented by a velocity contour near the ~7.5 km/s - 8.0 km/s range (Ponziani et al., 1995). On a broader wavelength in the images of Figures 4.24 we see the depth to such velocities highest beneath the Apennines at 30 km deep, but around 20 km deep beneath the western side of the study area and at intermediate depths beneath the Adriatic foreland. This longer wavelength variation combined with the absolute seismic velocity is consistent with this feature in our image being controlled by depth to Moho, or in other words crustal thickness. This is in agreement with the findings by Piana Agostinetti and Amato (2009) who, using inversion of teleseismic receiver function data, individuate broad regions with consistent Moho depth, specifically: (i) the areas in between the Thyrrennian coast and the belt, with a 20 to 25 km deep Moho; (2) the Adriatic foreland region with 30–35 km deep Moho; (3) the Apennines belt, where a general crustal thickening is encountered, possibly involving a Moho doubling related to overthrusting (e.g., Ponziani et al., 1995).

A noticeable feature of the cross sections in Figure 4.24 are the two faster (6.8 - 7 km/s) lobes to around 5 km depth beneath the Apennines hinge, and to 10-5 km depth beneath the western side of the Apennines near Florence. Velocities of ~6.8-7 km/s are faster than the global average wave speed of lower continental crust, but are typical of high grade metamorphic rocks (Christensen and Mooney, 1995). The spatial correlation between these shorter wavelength and positive velocity anomalies beneath the Apennines leads us to interpret them as the cores of major anticlines associated with the thrust system, in which deeper crystalline basement is driven upwards by compressional tectonics.

These structures likely coincide with the basement high reported in the deep cross sections by Martelli et al. (2017). Although deep wells did not reach the basement in the study area, many of them crossed anticlines which likely have the basement at their core (Anelli et al., 1994).

Similar interpretations for the origin of shallow high wavespeeds are proposed for the southern Apennines using results from controlled source tomography (Improta and Corciulo, 2006). There, the velocity model shows lobes of high-velocity higher than 7 km/s at up to depths as shallow as 8 km. The authors invoke that such large velocities cannot be related to sedimentary rocks, and imply the presence of shallow crystalline rocks, i.e., the basement involved in the thrust belt (Improta and Corciulo, 2006). For the southern Apennines the velocity model derived from controlled source tomography is consistent with crustal models from other geophysical data (local earthquake tomography, Bouguer and magnetic anomalies), and interpreted to support the process of thick-skinned tectonics affecting the Apennine crust (Improta and Corciulo, 2006).

A tentative tectonic interpretation of the tomographic data is proposed in Figure 4.29. The high compressional wave-speeds (7.8-8.0 km/s) resulting from the inversion are likely related to the crust/mantle interface (Moho discontinuity). Thus, I have put this limit where the Vp reaches 7.8-8.0 km/s. Similarly to what observed in several other studies (e.g., Di Stefano et al., 2009; 2011; Piana Agostinetti & Amato, 2009; Scafidi et al., 2009) the Moho is inferred to lay at a depth of about 25 km in the southwestern part of the section, deepening toward North-East to up to 30-35 km. Similarly, the limit between the internal and the external sectors, where the Moho is shallower and deeper, respectively, has been interpreted as a crustal thrust doubling the Moho (Ponziani et al, 1995; Barchi et al., 1998, Finetti et al., 2001; Sani et al., 2016 and references therein).

More difficult is to interpret the structures within the crust. The available focal mechanisms (Sani et al., 2016 and references therein) suggest very different kinematics of the seismic events at shallower depth (<15km) where extensional kinematics prevail, in respect to the deeper events showing compressional mechanisms. Moreover, the extensional mechanisms are generally concentrated along the main divide of the northern Apennines, whereas the deeper compressional events mainly occur along the north-eastern side of the chain. Following these considerations, the shallower seismicity along the divide can be associated with normal faults, such as those bordering the Mugello area. These faults likely cut previous compressional structures as indicated in field studies (Bonini et al., 2016). On the contrary, the deeper seismicity located to the NE could be related to the still active thrust system emanating from the deep crust. The combination of my earthquake locations and velocity model is consistent with previous interpretation that this complex thrust system gradually splays at surface, at the leading edge of the northern Apennines chain, and corresponds to the active thrusts that generated the 2012 seismic events in the Mantova-Ferrara area in the Po Plain (Martelli et al., 2017).

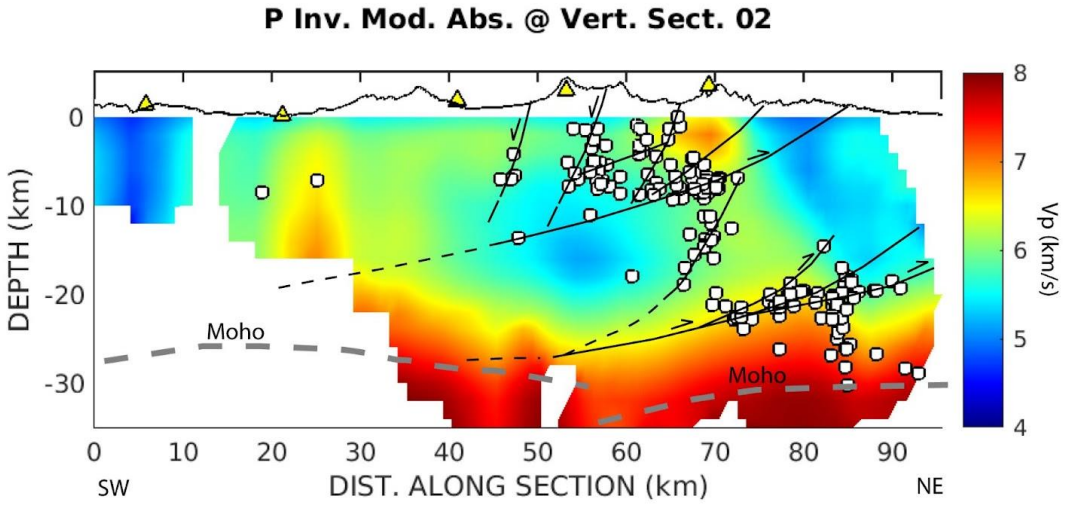


Figure 4.29: Tectonic interpretation of the tomographic section reported in Figure 4.24 (panel c). The Moho discontinuity is reported with dashed grey lines. Major structures are reported in black,

and their inferred kinematics is indicated by arrows on the hangingwall. The prolongation at depth of some of the structures is inferred with dashed black lines.

4.6 Conclusions

I used local earthquakes recorded on 75 permanent and temporary seismic stations to invert for both 1D and 3D seismic velocity models for the Northern Apennines. For the 1D model, I used 1796 events selected from the merged catalog (Chapter 2) with at least 20 arrival times, including at least 10 S-wave arrivals, and the code Velest. I tested different P-wave starting models and starting Vp/Vs of 1.73 and 1.81. I ran inversions with the Vp/Vs ratio of the output model fixed and variable for each layer. In this study, the latter option yielded the best output model. The resultant output models are, however, similar independent of the starting model. The favoured best-fit 1D model was then used as a starting model for the 3D tomography, along with an alternative starting model from Piccinini et al. (2014), and using the code LOTOS. The inversion was performed using a parametrization in nodes, 5 iterations and a grid size of 5 km. The inversion result is a combination of the inversions performed over 4 different orientations of the grid (0°, 22°, 45°, 67°). Spike and checkerboard tests indicate that our study has good resolution to ~20-25-km-depth in the middle of our study area, but the well resolved area shallows to ~15-20-km-depth towards the edges of the study area. The tests indicate that the minimum size of anomaly that can be resolved is 10 km size.

Results obtained from the 2 starting models share the same main features. Overall, the crust is characterised by seismic velocities between 5.5 km/s at the surface to around 6.5 km/s in the lower crust, typical of continental crust globally. At depth, we observed a marked velocity gradient culminating with velocities in the ~7.5 km/s - 8.0 km/s range that we interpret as the Moho. The depth to this is highest beneath the Apennines at ~30 km deep, but around 20 km deep beneath the western side of the study area and at intermediate depths beneath the Adriatic foreland. At shallow depth there are localised lobes of fast velocities of >7-km/s up to 5-10 km depth that are located mainly along the Apennine hinge, and in a sub-parallel NW-SE striking band on the western side of the Apennines. The spatial correlation between these shorter wavelength and positive velocity anomalies beneath the Apennines leads us to interpret them as the cores of major anticlines associated with the thrust system, in which deeper crystalline basement is driven upwards by compressional tectonics. Elsewhere, the main slower P-wave speed regions are located on (i) the Adriatic foreland side of the Apennines, (ii) within the western side of Apennine hinge in between the positive anomalies mentioned above, and (iii) beneath the plain between the Apennines and the western coast. Overall, the new seismic images provide evidence that thick-skinned tectonics occurs to build the Apennines.

Chapter 5

Seismic Sequences

Portions of this chapter are parts of:

- a report in Rapporti Tecnici INGV (in press):

Bruni R., Biagini D., Capello M., Corti G., D'Ambrosio M., Fiaschi A., Giunchi C., Keir D., Piccinini D., Sani F., Saccorotti G. *A temporary network for monitoring seismicity in the Mugello basin (Northern Apennines, Italy).*

- and a published paper on the Journal of Geophysical Research - Solid Earth:

Cianetti S., **Bruni R.**, Gaviano S., Keir D., Piccinini D., Saccorotti G., Giunchi C. *Comparison of deep learning techniques for the investigation of a seismic sequence: an application to the 2019, Mw 4.5 Mugello (Italy) earthquake. https://doi.org/10.1029/2021JB023405*

5.1 Introduction

A seismic sequence is a series of earthquakes occurring in a local area within a relatively short period of time. The length of that time interval varies, but it may be days, months, or years. A seismic sequence is characterized by a major event (main shock), followed by a series of aftershocks, and sometimes preceded by foreshock activity.

The detailed analysis of seismic sequence is of paramount importance in the characterization of the seismo-tectonic setting of a region. The accurate location of the mainshock and its aftershocks may provide decisive constraints for identifying location and geometry of the activated fault systems. With this in mind, in this chapter I use the accurate relocation of seismic sequences from near the Mugello basin in the Northern Apennines to evaluate the locus, subsurface geometry, and segmentation of the extensional fault systems. This is particularly important for the northern side of the Mugello basin where there is debate regarding the location of active faults, and how these faults interact (Bonini et al., 2016 and references therein).

During the time period 2005-2021, four important seismic sequences occurred within the area of study, in particular in the years 2008, 2009, 2015 and 2019. In this Chapter, I first describe those sequences and, through integration of high-resolution hypocentral locations and fault plane solutions, proceed with an assessment of the subsurface properties of these activated fault systems.

5.2 Seismicity over the 2005-2021 time interval

In this section I focus the attention on the seismic sequences that occurred in and around the Mugello basin over the 2005-2020 time interval. I analysed the sequences using distinct datasets: i) the INGV catalog as described in Chapter 2; ii) the merged catalog in Chapter 2 for the period January 2005 - April 2019, and of the integration of the arrival time of INGV with the data recorded by the stations of the 9M network for the period encompassing the 2019 sequence. The coordinate limits of the area considered in this chapter are [43.85°- 44.20°] and [11.05° - 11.60°] for latitude and longitude, respectively. Hereafter, I refer to this region as the '*study area*'. This selection has been made to better constrain the main sequences that occurred over the whole period within and around the Mugello basin.

5.2.1 The INGV Catalog

An overall picture of the seismicity within the study area is offered by the INGV catalog which, for the considered time interval, includes 1920 earthquakes. The spatial and temporal distribution of the seismicity from this catalog are shown in Figures 5.1 and 5.2. The epicentral map (Fig. 5.1) is dominated by two main spatial clusters, located at the NW and central sectors of the area. These two spatial clusters correspond to periods of enhanced activity (Fig. 5.2) that occurred in January 2015, and December 2019. The 2015 sequence was located near Castiglione dei Pepoli (BO), with a mainshock of Magnitude 4.3. The 2019 sequence was located in proximity to Scarperia e San Piero a Sieve (Fig. 5.1), with a mainshock of Magnitude 4.5.

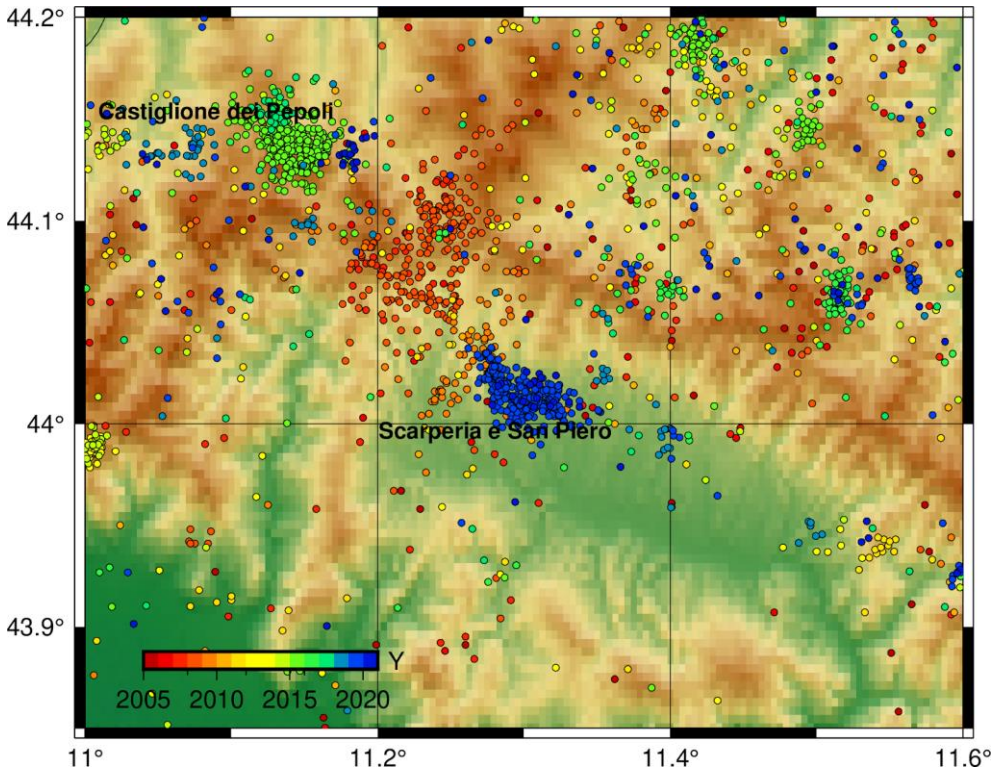


Figure 5.1: Spatial and temporal evolution of the seismicity of the INGV catalog over the period 2005-2020 within and around the Mugello basin. The dots are the epicenters colored by the origin time.

Figure 5.2 shows the temporal evolution of earthquake magnitudes and weekly occurrence rate. The rate histogram shows the main seismic sequences of 2015 and 2019 mentioned earlier, as well as two additional sequences that occurred in 2008 and 2009. For all these sequences, the mainshocks had similar magnitudes, spanning the range Mw=[4.2 - 4.5].

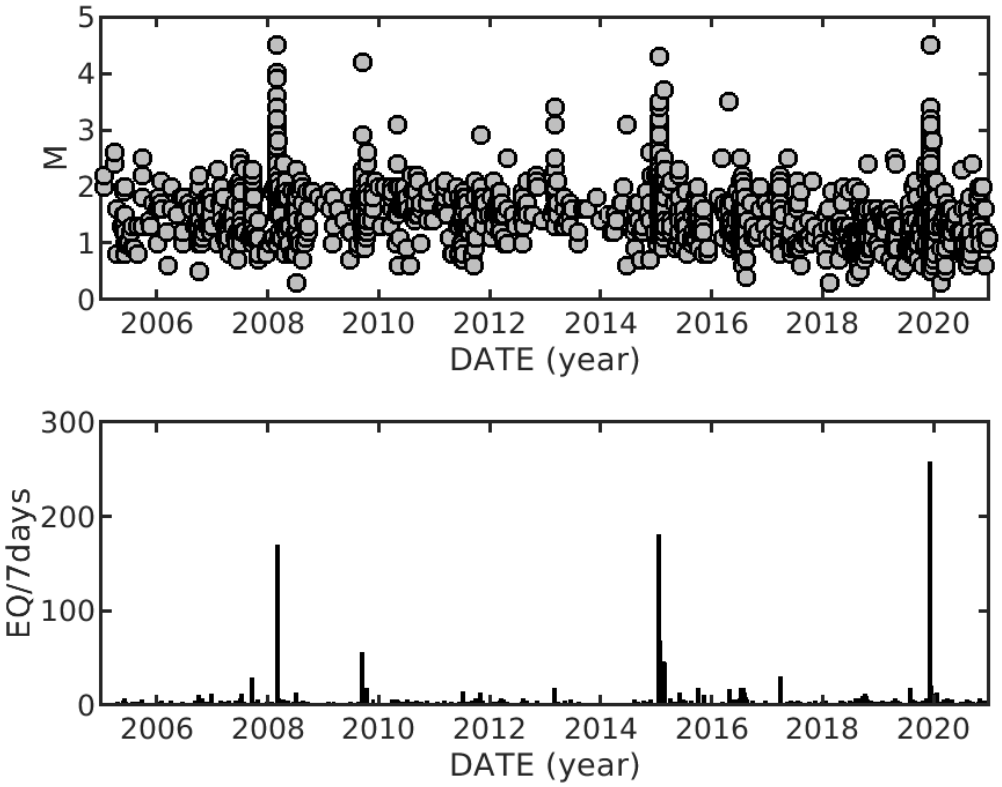


Figure 5.2: Time evolution of the magnitude (on top) and the weekly occurrence rate of earthquakes (on bottom) for the seismicity recorded in the period 2005-2020 in the area of study. The maximum value of magnitude for each sequence is similar, nearly 4.5.

5.2.1.1 Catalog statistics

The statistical properties of the INGV catalog are analysed using the Gutenberg-Richter (GR) law, that expresses the relationship between the magnitude and the total number of earthquakes of a particular magnitude in a given region and time period (Figure 5.3). The GR relationship takes the form: log(N(M)) = a-bM, where N is the number of earthquakes with magnitude greater than M, *a* and *b* are constants to describe the equation of a straight line when plotted semi-logarithmically (Ishimoto and Iida, 1939; Gutenberg and Richter, 1944). The *a-value* (y-intercept) is an indicator of the total seismicity rate of the region; the *b-value* (slope) indicates the relative proportion between the number of high-magnitude and low-magnitude earthquakes. The parameter *b* is commonly close to 1.0 in seismically active regions. Using the least-squares estimation, based on the script included in the Zmap package (Wiemer, 2001), the values of the parameters are: a = 5.12; b = 1.1. The magnitude of completeness (Mc) is the minimum magnitude above which all earthquakes within a

certain region are reliably recorded. The Mc is evaluated with the Maximum Curvature method (MAXC; Wiemer and Wyss, 2000), and is equal to 1.4. In the MAXC technique, Mc is obtained from the maximum value of the first derivative of the frequency-magnitude curve.

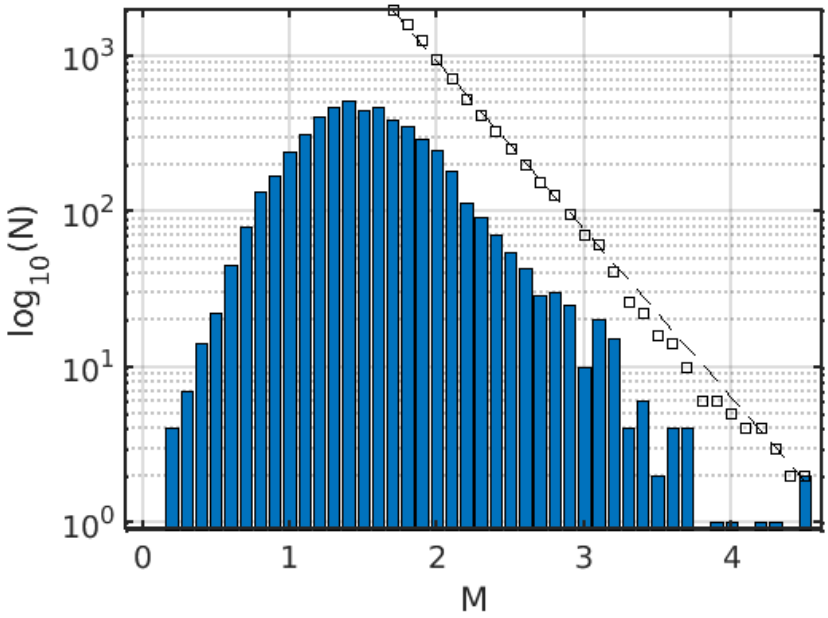


Figure 5.3: The Gutenberg–Richter law of INGV catalog. Bars are the number of earthquakes in magnitude bins of 0.1 magnitude units. The black squares are the cumulative number of earthquakes starting from the largest magnitude earthquake.

5.2.2 The seismic sequences from the integrated catalogs

An improved image of the aforementioned sequences is gained using two integrated catalogs which are: i) from 2005 to April 2019, the INGV - PARSEC merged catalog, already described in Chapter 2. For the study area, this data set has 2542 events; ii) for the 2019 sequence, a set of re-picked P- and S-wave arrival times measured at stations from the 9M network, and INGV stations located within 30km from the epicentral area. These arrival times are inverted using the same procedure described in Chapter 2, Section 2.3, leading to a set of 287 events spanning the December 8, 2019 -January 11, 2020 time interval.

Figure 5.4 shows the spatial and temporal evolution of the seismicity resulting from the above two catalogs. In this case, the spatial clustering of epicenters is much more evident, especially for the 2008 and 2009 sequences. In particular, epicenters from the 2009 sequence appear to delineate a NNW-SSE striking structure, linking the epicentral areas from the previous (i.e., 2008) to the subsequent (2019) sequences. Figure 5.5 shows the temporal distribution of the weekly number of earthquakes. From this distribution, it is clear how the integration between the INGV and PARSEC catalogs brought a marked improvement in catalog completeness. This is particularly evident for the 2008 and 2009 sequences, for which the peak weekly rate increased from 170 to 260 and from 50 to 230 earthquakes/day, respectively. These catalogs also form the basis for double difference earthquake relocation described in section 5.2.3 in this chapter.

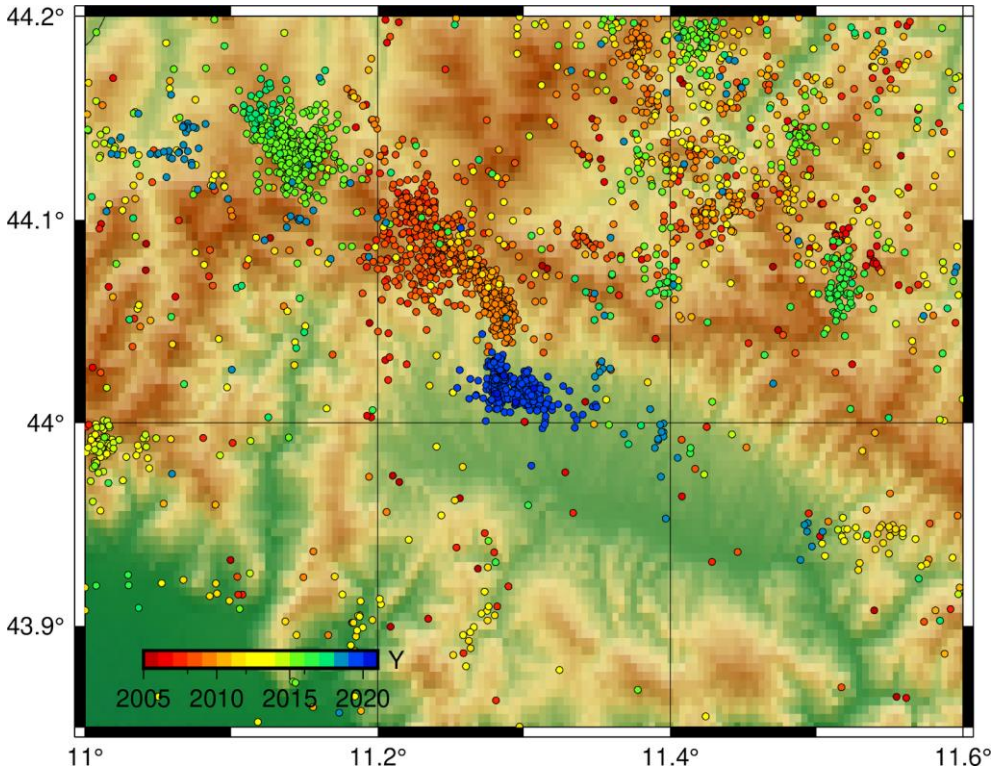


Figure 5.4: Spatial and temporal evolution of the seismicity of the merged catalogs over the period 2005-2020 within and around the Mugello basin. The dots are the earthquakes colored by the year of occurrence.

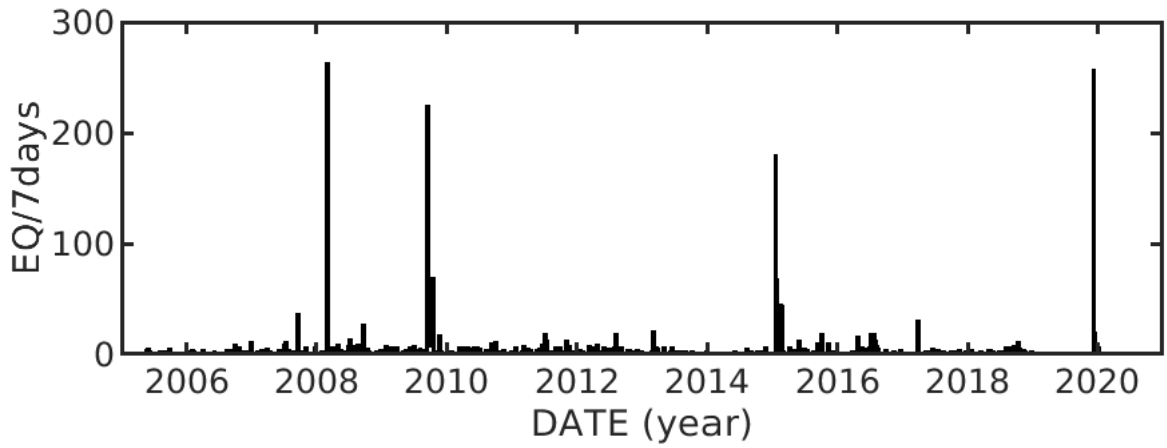


Figure 5.5: Temporal evolution (histogram of weekly event rate) during the 2005-2020 time interval.

5.2.3 Relocations, focal mechanisms and fault planes

Earthquakes from the merged datasets are then relocated using HypoDD, a Fortran computer program package that uses the double-different (DD) algorithm of Waldhauser and Ellsworth (2000) to locate earthquakes. The DD technique is based on the similarity of the raypaths between the source and a common station when the hypocentral separation between two earthquakes is small with respect to the event-station distance and the extent of velocity heterogeneity. This approach permits to reduce systematic errors related to the prediction of travel times in poorly known velocity structures, and hence to achieve more focused images of hypocenter clustering.

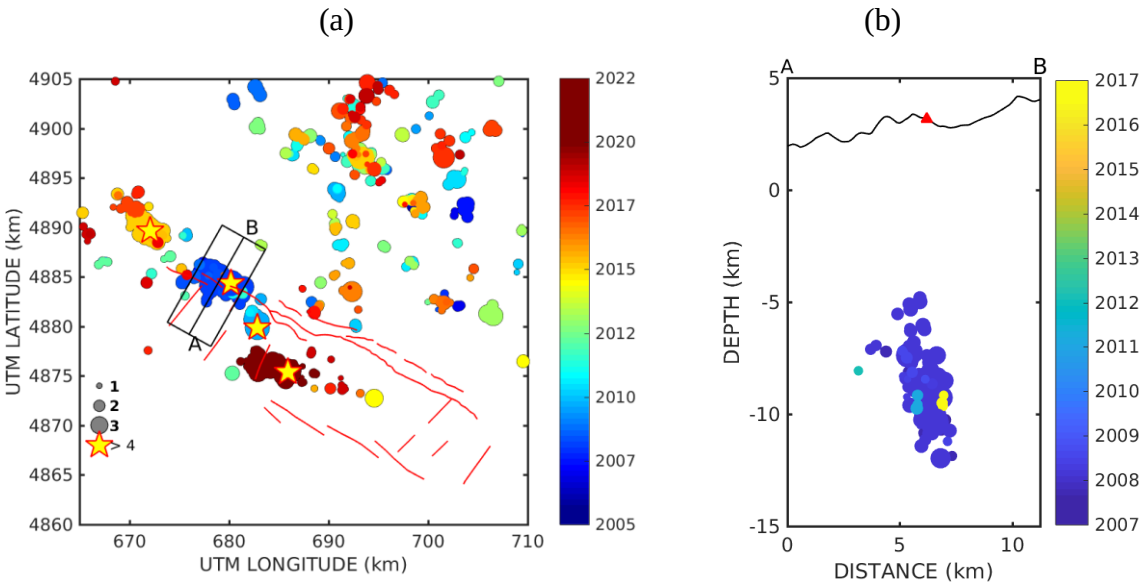
In Figure 5.6 I show the result of the relocation of the merged datasets, where one can appreciate an improved spatial clustering of the four sequences. From the cross-sections of Figure 5.6 it can be seen the orientations of the clusters and the possible fault planes the clusters are on. I also show the TDMT solution of the mainshocks as reported in the INGV catalog. Below I describe distinguishing features of the clusters in chronological order (Fig. 5.6).

The 2008 sequence occurred in a 7-12 km depth range, is well clustered and hypocenters are distributed along a steep NNE-dipping planar structure (Fig. 5.6 a,b), consistently with the previous findings by Piccinini et al. (2014) and Bonini et al. (2016). The mainshock occurred on March 1, 2008, with moment magnitude Mw=4.5. The corresponding TDMT solution from the INGV catalog is reported in Fig. 5.6 a.

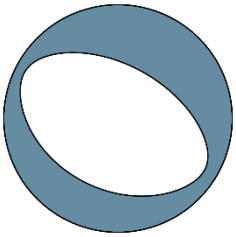
The 2009 sequence has a mainshock of Magnitude (Mw) 4.2 that occurred on September 14, 2009, and hit the NW margin of the Mugello basin. The depth distribution of this seismic sequence delineates a SSW-dipping normal fault ascribable to the Ronta fault system (Fig. 5.6 c,d), consistently with the previous studies by Piccinini et al. (2014) and Bonini et al. (2016).

The events of the 2015 seismic sequence occurred from 2015 to 2017, and seem to be distributed according to 2 different structures. In particular, hypocenters from the main activity (occurred in January, 2015) define a cluster at 5-10 km depth that is sub-vertical (Fig. 5.6 e,f). The mainshock occurred on January 23, 2015, with a moment magnitude of 4.3. The source mechanism as derived from the TDMT reported by the INGV catalog is shown in Figure 5.6 e. The later seismicity is spatially detached from the previous activity and forms a slightly more diffuse cluster at ~9 km depth that subtly exhibits a NW-dipping orientation (Fig. 5.6 g,h).

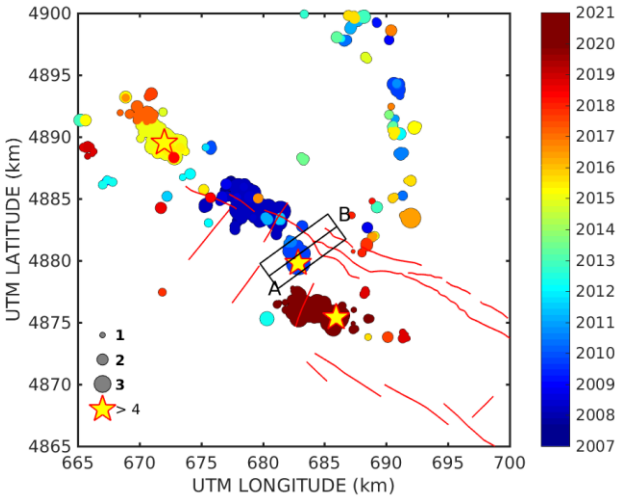
The relocation with HDD of the 2019 sequence, which is well described in the next section (Section 5.3), delineates a SW-dipping planar structure extending over the 6-11 km depth interval (Fig. 5.6 j). This geometry is in agreement with the Time Domain Moment Tensor (TDMT) solution of the mainshock reported by the INGV catalog (http://cnt.rm.ingv.it/event/23558121), which indicates a normal fault striking N105°E and dipping about 45° (see Fig. 5.6 i).



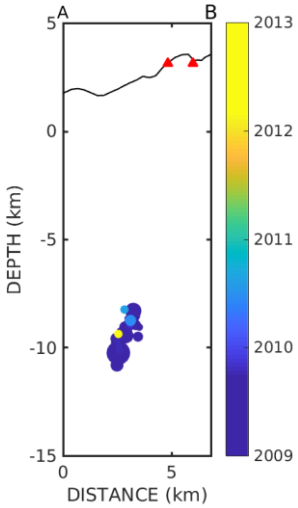
Mw 4.5 of 01-03-2008 07:43:13 (UTC)



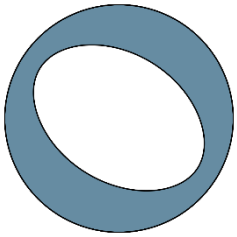
(c)



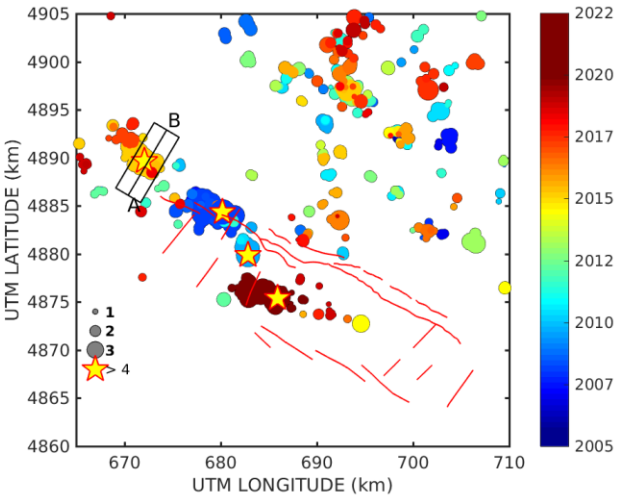
(d)



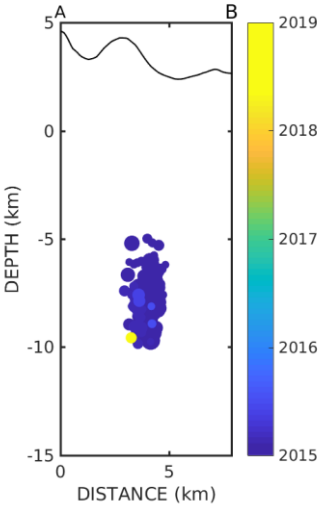
Mw 4.2 of 14-09-2009 20:04:31 (UTC)



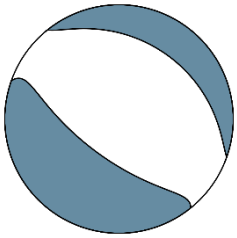
(e)



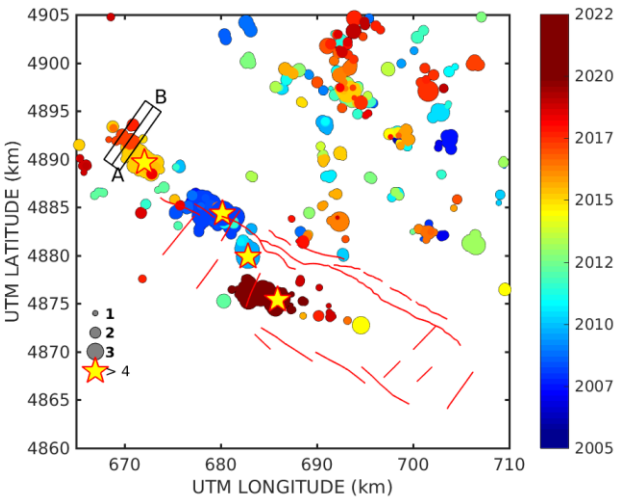
(f)



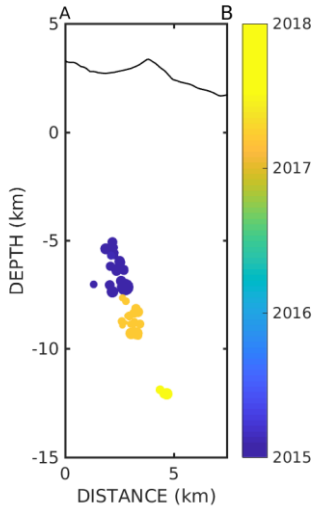
Mw 4.3 of 23-01-2015 06:51:20 (UTC)



(g)



(h)



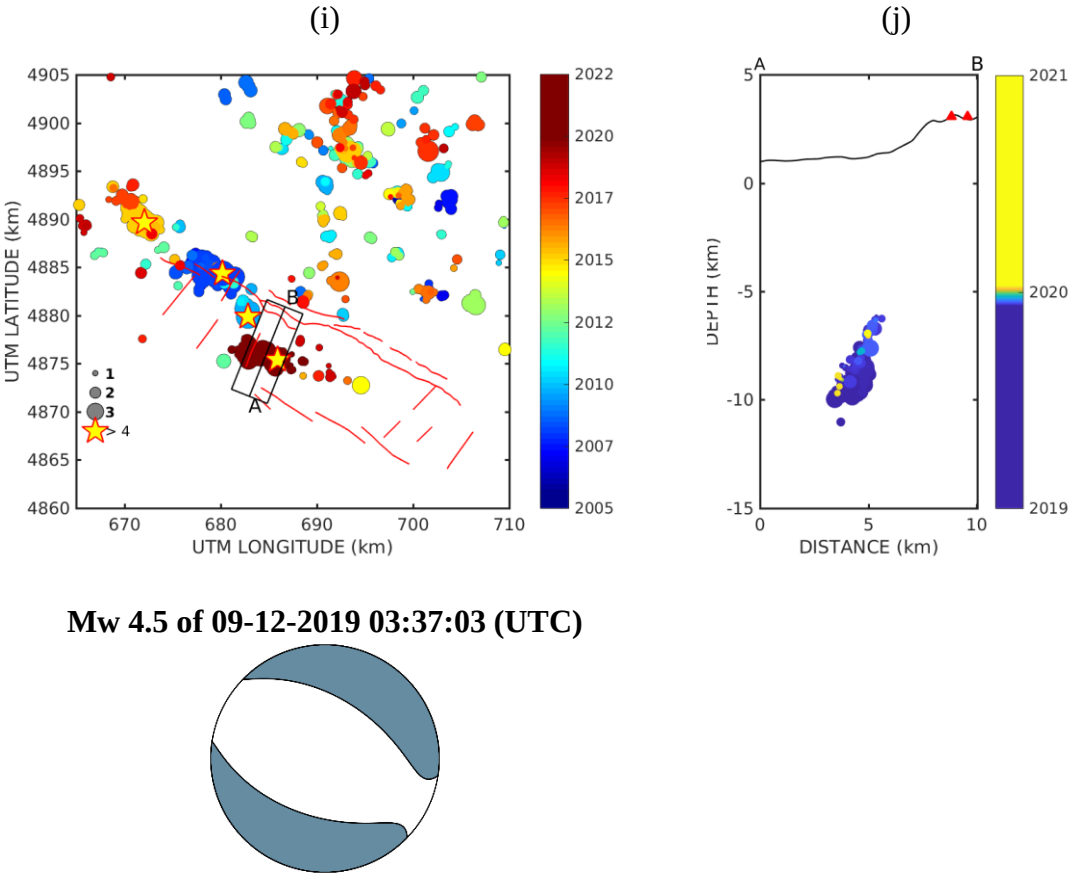


Figure 5.6: Epicentral maps and vertical cross sections. Symbol size is proportional to magnitude, and stars indicate the mainshock of each sequence. Colors correspond to the date of occurrence of the events. The focal mechanism refers to the double-couple component of the TDMT solution reported by the INGV catalog for each mainshock. In panel a) there isn't a focal mechanism because the events are considered part of the 2015 sequence reported also in panel c). This split is due to a possible, different orientation of the structures along which the hypocenters are distributed.

To constrain the actual fault plane of each sequence, I fitted the hypocenters with a plane and compared it with the two nodal planes obtained from the TDMT solution reported by the INGV catalog. The results are shown in Table 5.1: the TDMT solutions most similar to the planes identified by hypocenters alignment are highlighted. Figure 5.7 shows the plane fitting to hypocentral data from Double-Difference relocation for each sequence.

	Plane Fitting Hypocenters		**TDMT**			
Sequence	**Strike (°)**	**Dip (°)**	**Strike (°)**	**Dip (°)**	**Strike (°)**	**Dip (°)**
2019	106	59	105	46	308	46
2015	315	86	127	60	304	30

2009	136	53	122	45	303	45
2008	292	70	116	38	300	52

Table 5.1: Comparison between the plane fitting the hypocenters with the TDMT solutions. For each sequence, the TDMT solution most similar to the plane identified by hypocenters alignment is highlighted in grey.

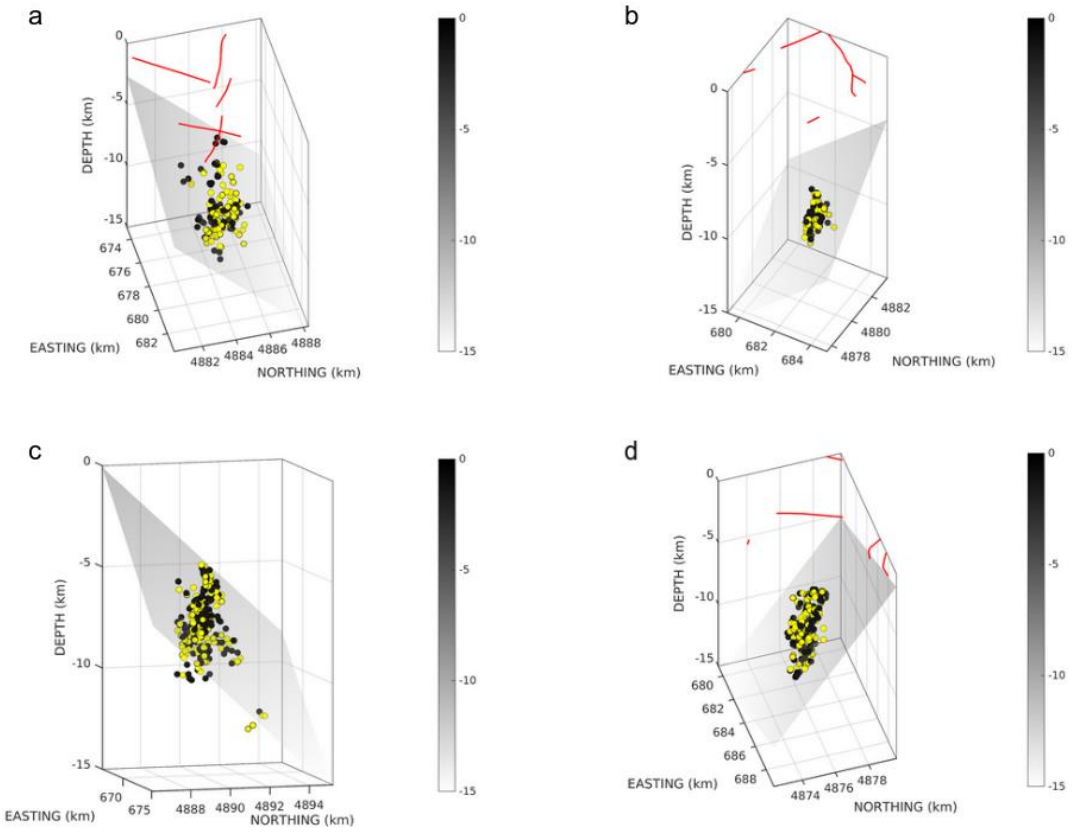


Figure 5.7: Plane fitting to hypocentral data from Double-Difference relocation of each sequence: a) 2008, b) 2009, c) 2015, d) 2019.

Furthermore, the fault dimensions expected from the magnitude of the mainshocks (~4.2-4.5) are on the order of 1-1.5 km length, according to the empirical relationships proposed by Leonard (2014). The volume spanned by aftershocks in each sequence is greater than the fault size calculated from the magnitude of the respective mainshock only. This is graphically shown in Figure 5.8 where the area that includes the hypocenters of each sequence (black box) is compared to the fault size modeled from the magnitude of the respective mainshock (red box). This observation may be interpreted in different manners. If the modelled main shock faults are realistic in size, then this means that the aftershocks are occurring on 1) adjacent portions of the same fault, or 2) on adjacent fault segments. Option [1] implies that the main shocks are only rupturing a portion of each fault segment, and that larger-magnitude earthquakes could result from rupture of that segment as a whole. Option [2] implies that earthquakes larger than that observed would require the quasi-simultaneous failure of multiple fault segments. Discriminating between these two possibilities is a crucial issue toward a more

solid assessment of seismic hazard in the region; however, such discernment goes beyond the resolving capabilities of the available data set.

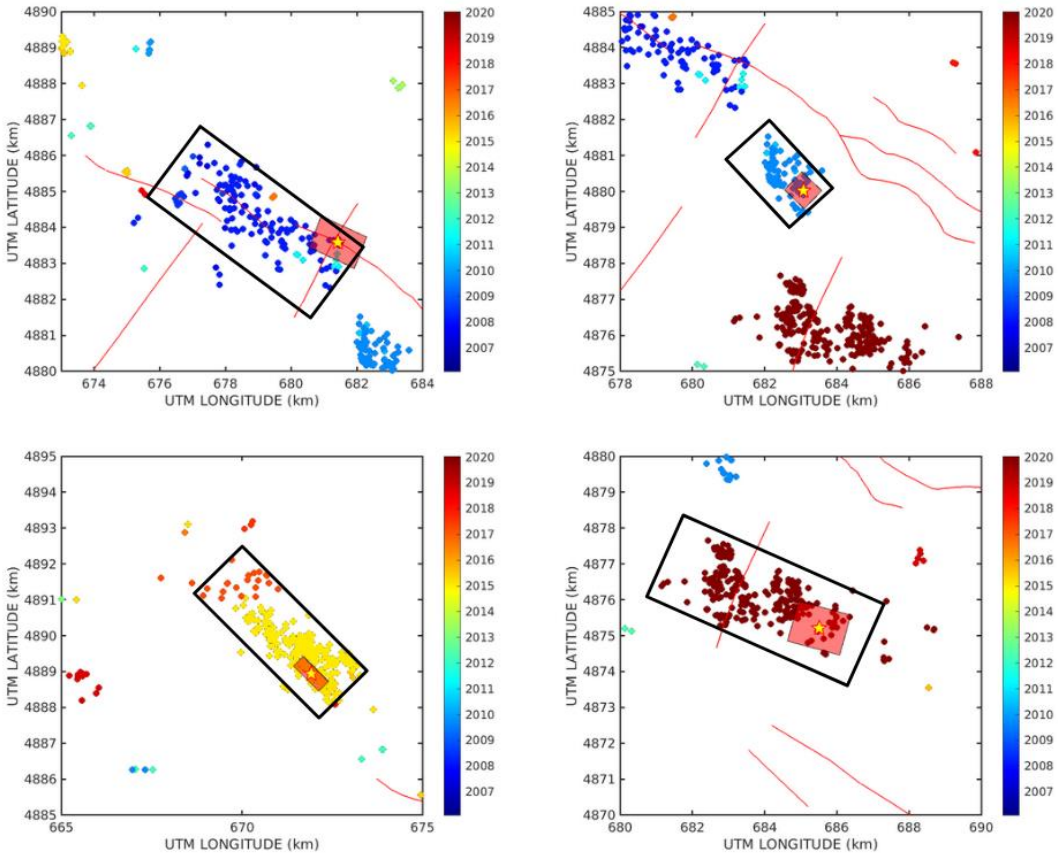


Figure 5.8: Comparison of the extension of the hypocenter distributions with the fault size corresponding to the mainshock. The black box contains the hypocenters of each sequence, and the red box is the fault projection calculated using Leonard (2014) empirical relationship, and assuming a fault aspect ratio equal to 1.

A further question regards the possible involvement of fluids in the processes which control the analyzed sequences. This aspect is approached in the Supplementary Material, where I investigate the spatial and temporal evolution of individual sequences. I anticipate that such determinations do not provide any evidence pointing to the diffusion of a pore pressure front as the driver of the observed seismicity.

5.3 Focus on the 2019 sequence

In this section I focus on the 2019 sequence, whose mainshock struck the NW margin of the Mugello basin on December 9, 2019, at 03:37:03 UTC, with an estimated magnitude M_w=4.5. Figure 5.9 shows the seismograms of the main event recorded by stations of 9M and INGV networks. Figure 5.10 shows the daily plot of the seismicity recorded by the 9M station RONT during the 9th of December 2019. The aftershock events lasted about a month, accounting for 279 earthquakes with magnitudes in the range of 0.5 - 4.5.

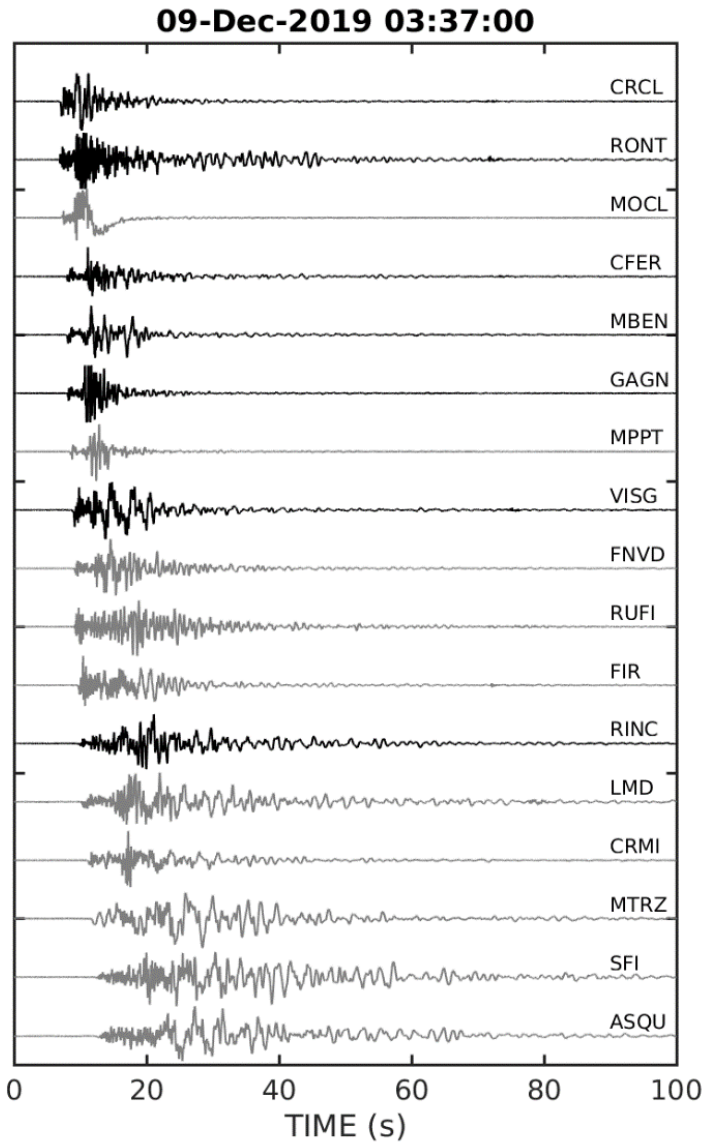


Figure 5.9: Vertical-component 100s-long seismograms from stations of the 9M and INGV networks (black and gray lines, respectively) for the M_w=4.5 earthquake occurred on December 9, 2019. Traces are individually normalized to the respective maximum amplitude.

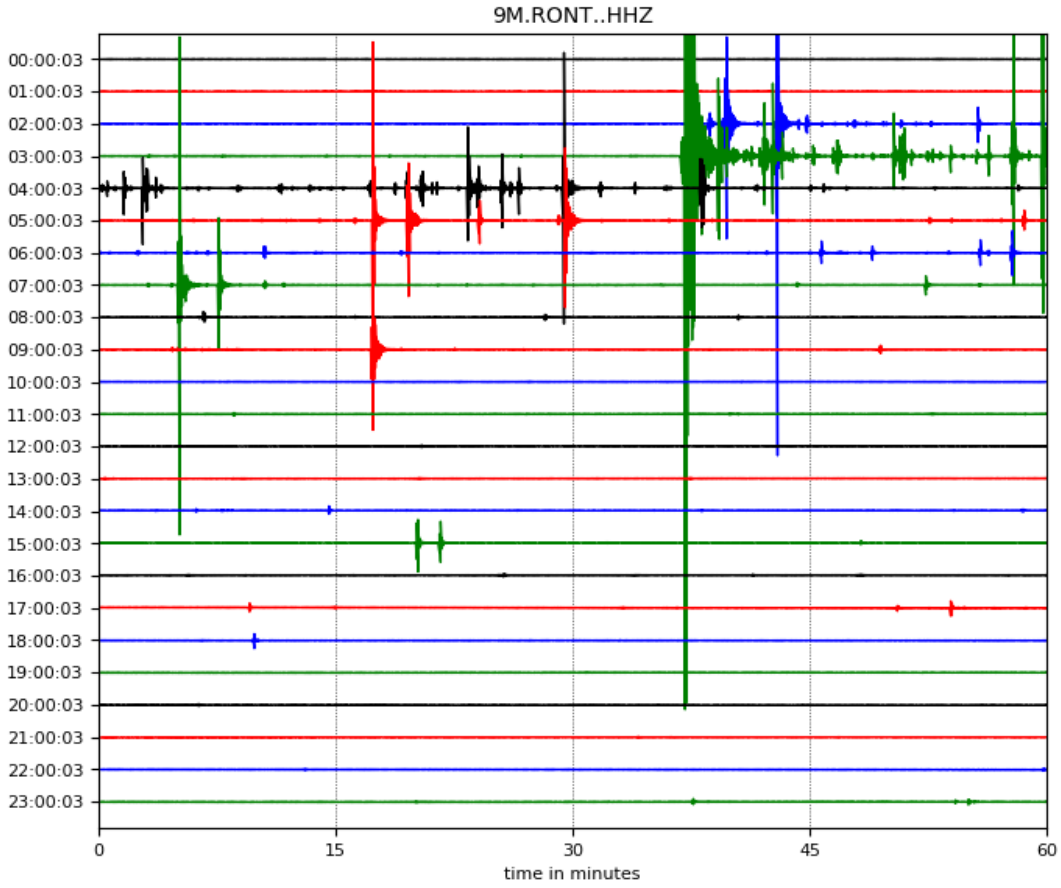


Figure 5.10: Daily helicorder plot of the seismicity recorded by the vertical component of the 9M station RONT on 9th December 2019. Each horizontal line is a one hour-long seismic trace, with the 24 traces progressing in time from the start of 9th Dec at the top. Different colours of traces are purely to help differentiate adjacent seismic traces. The vertical scale is the same for all the traces.

Using the local magnitude (M_L) reported in the INGV catalog I show on top of Fig. 5.11 the temporal evolution of the M_L during December 2019, and on bottom the cumulative release of seismic moment (M_0). For each event, the seismic moment was estimated from the catalog magnitude using the formula $M_0 = 10^{(1.5*M_L+9.1)}$ [N m] (Kanamori H., 1977). Most of the events occurred during the first 2 days following the mainshock, corresponding to the maximum seismic moment release. The seismic activity continues quite homogeneously until 17th December, then reappears with 4 events at the end of the month.

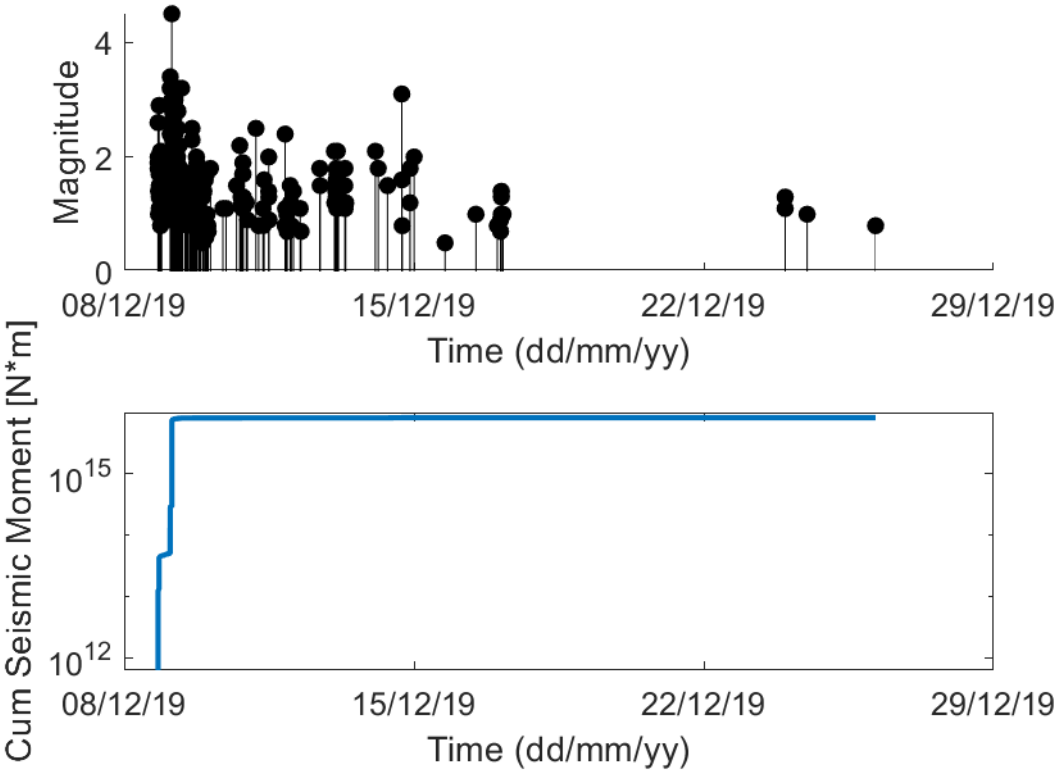
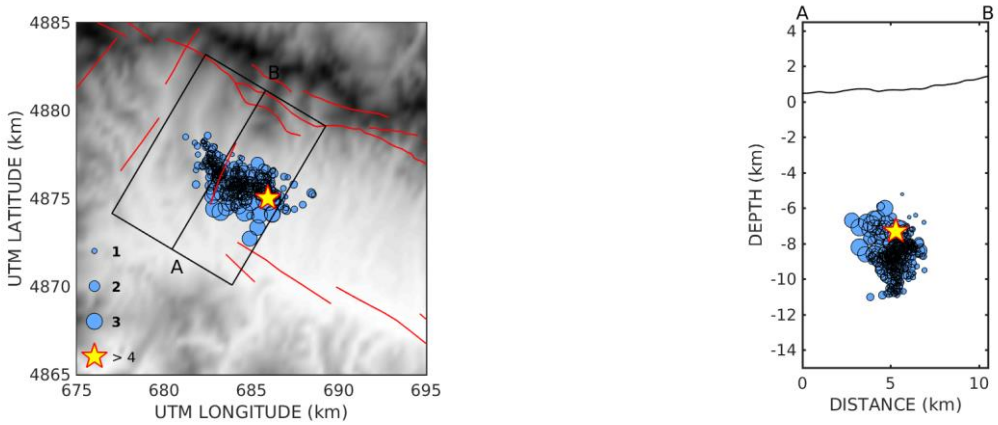


Figure 5.11: On top the local magnitude versus time; on bottom the cumulative seismic moment release during the sequence.

Figure 5.12 illustrates the comparison between the original INGV locations, and those retrieved after integration of the phase readings from the temporary network, as described in the previous Section 5.2.2. The two datasets are referred to as INGV and 9M+INGV, and displayed with light blue and red symbols, respectively. The two sets of locations exhibit a similar epicentral pattern, that delineate a 6-km-long, NW-striking structure (Fig. 5.12 a,c), despite the use of different geometry network and velocity models.

(a) (b)



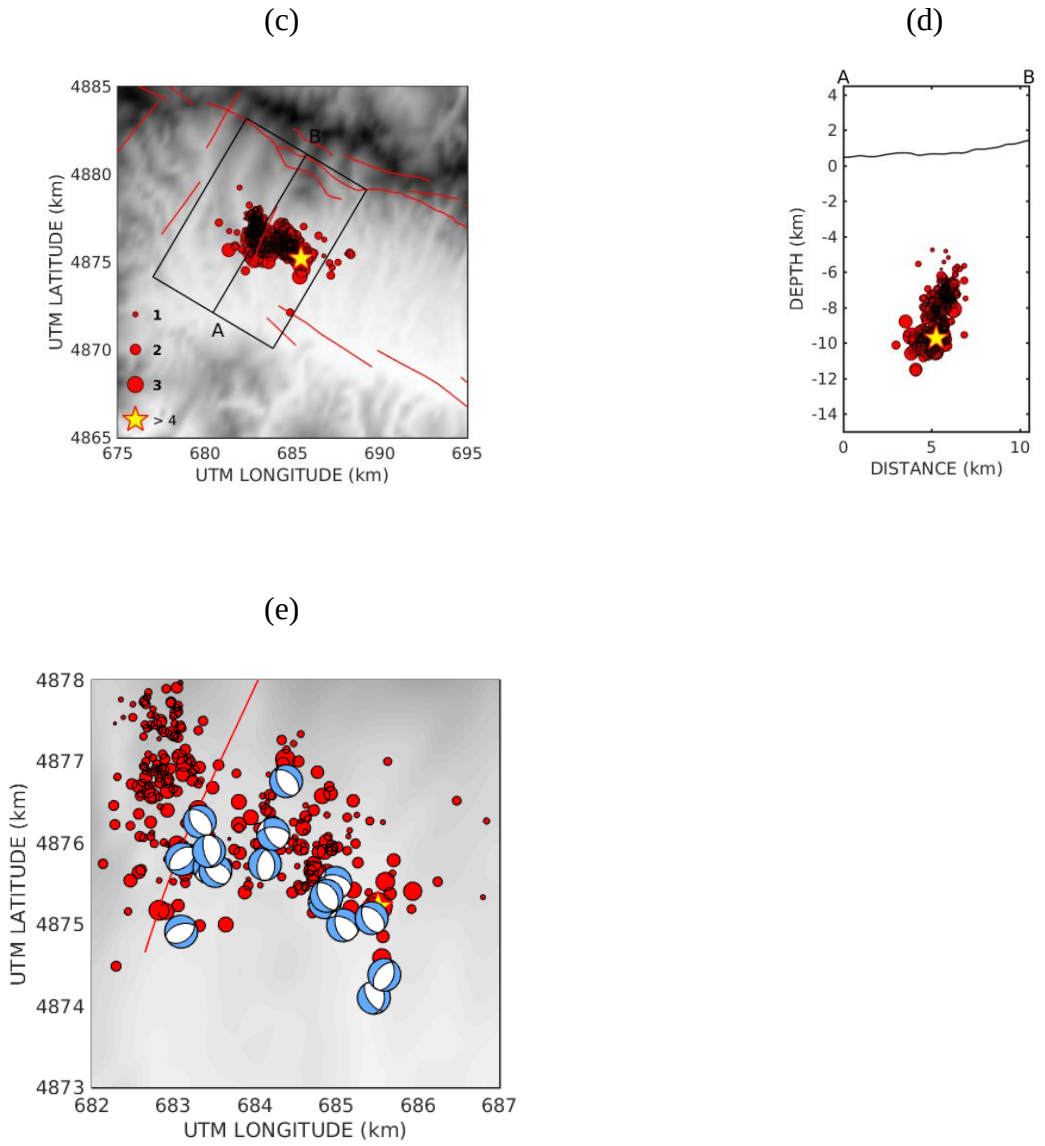


Figure 5.12: Epicentral maps and vertical cross sections for the December 2019 seismic sequence located using data from the INGV (a,b) and 9M+INGV (c,d) configurations. The area corresponds to the black box reported in Chapter 2 Figure 2.1. Symbol size is proportional to magnitude according to the scale reported at the bottom left in panels (a) and (c); stars indicate the mainshock. In panel (e) the double-couple fault plane solutions derived from 17 earthquakes with at least 15 polarity readings, and gaps in azimuth and take-off angles lower than 180° and 60°, respectively.

The three-dimensional fault geometry, however, is much better shown by the 9M+INGV locations, which exhibit the same SW-dipping fault as mentioned before (Fig. 5.12 d). While comparing the INGV and 9M+INGV locations, however, one has also to consider that some stations of the 9M network (specifically: RONT, RINC and VISG) have been shared in real time with the

INGV acquisition center, and therefore also used for INGV locations. Figure 5.12 panel (e) reports the fault plane solutions derived from inversion of P-wave polarities using the HASH code (Hardebeck and Shearer, 2002). The results are from 17 earthquakes with at least 15 polarity readings, and gaps of azimuth and take-off angles lower than 180° and 60°, respectively. All the solutions indicate normal faulting, and most of them are consistent with the NW-SE striking planes indicated by both the Moment Tensor solution of the mainshock and the plane-fitting of hypocentral data. A few solutions, however, suggest the activation of fault planes striking NNE-SSW, the so-called 'anti-Apenninic' direction. Such a hypothesis would be supported by the surface evidence of a similarly-oriented transverse structure outcropping in the area, as it is shown in Figure 5.12. It must be considered, however, that individual fault plane solutions derived from inversion of P-phase polarities only, may be poorly constrained due to both data and modeling uncertainties.

5.3.1 Improvement of catalog completeness using Matched Filter

In order to improve the completeness of the catalog of the 2019 sequence, I applied the matched filtering technique to the continuous time series acquired by some stations of the 9M and INGV networks in the period spanning the 1 - 31 December 2019. Matched filter is an earthquake detection method based on waveform cross-correlation for identifying replicas of a known signal in continuous time series data (e.g. Gibbons and Ringdal, 2006). The method is based on the waveform similarity observed within seismic sequences (Geller and Mueller, 1980): seismic waves originated from sources with similar location and mechanism travel a similar path to the receiver, resulting in similar waveform shapes recorded by the receiver (Herrmann et al., 2019). This technique facilitates detection of new events characterized by low signal-to-noise ratio (SNR) yielding a better sensitivity than the one obtained from the common detection techniques such as STA/LTA (e.g. Gibbons and Ringdal, 2006; Schaff, 2008). In correspondence with windows containing a replica of the template signal, cross-correlation will exhibit a maximum at a time lag corresponding to the delay between the two signals.

I used up to 279 earthquakes reported in the INGV catalog as template earthquakes and performed a detection procedure on the continuous seismic data at six stations that are close to the epicentral area and have the most continuous records (specifically, stations CRCL, GAGN, MBEN, MOCL, RONT, and SEI). The exact number of template events does vary (227-279) between stations, since not all the events were recorded with sufficient quality at all the stations. The matched filter procedure is conducted separately for P- and S-waves. P-waves are searched over the vertical-component recordings, using 3 s-long template waveforms starting 1 s before the picked arrival time. For S-waves, the procedure is iterated over the N and E components, using 5 s-long template waveforms starting 1 s before the picked arrival time. Both templates and continuous data streams are band-pass filtered within the [2-15] Hz frequency band. At first, I stored all the matching wavelets having maximum cross-correlation (CC) larger than 0.5. Then, I removed duplicate matches derived from different templates with similar waveforms, keeping only the template-match pair with the highest CC. At all the stations, the number of matches decreases with increasing CC; the rate of decrease, however, is not constant, exhibiting an evident change of slope at CC0.7 (see example for P-wave in Fig. 13a and for S-wave in Fig. 14a). Therefore, I choose CC = 0.7 as a threshold for selecting the matched phases to be subsequently used for the location procedure. The number of matches for each template changes as shown in Figure 5.13b and 5.14b. Two examples of P- and S-wave templates and corresponding matching phases are shown in Figure 5.13 and 5.14, panels (c) and (d), respectively.

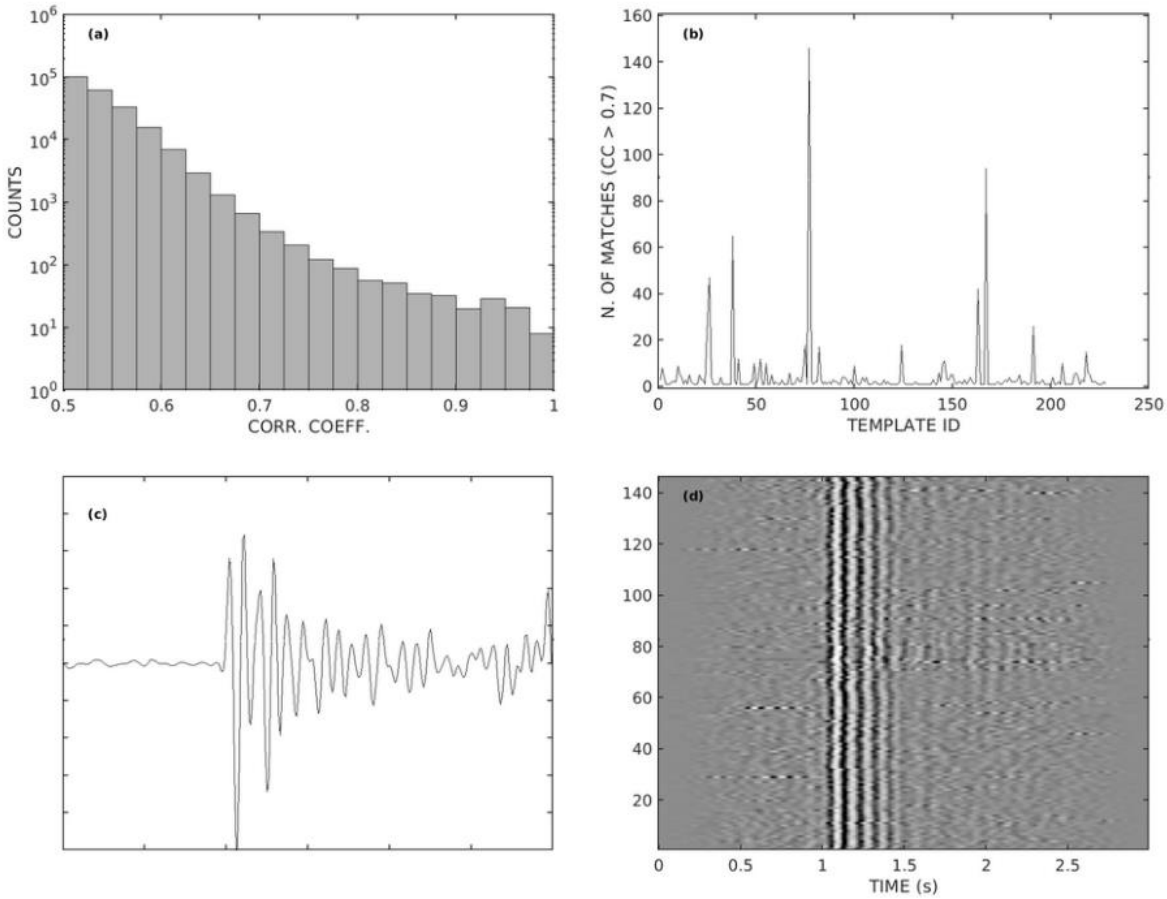


Figure 5.13: Example of the matched filter procedure for P-waves recorded at station RONT. a) Number of P-wave matches as a function of CC. b) Number of matches for each template. c) Seismogram of the P-wave template with the largest number of associated detections; d) the corresponding matched waveforms.

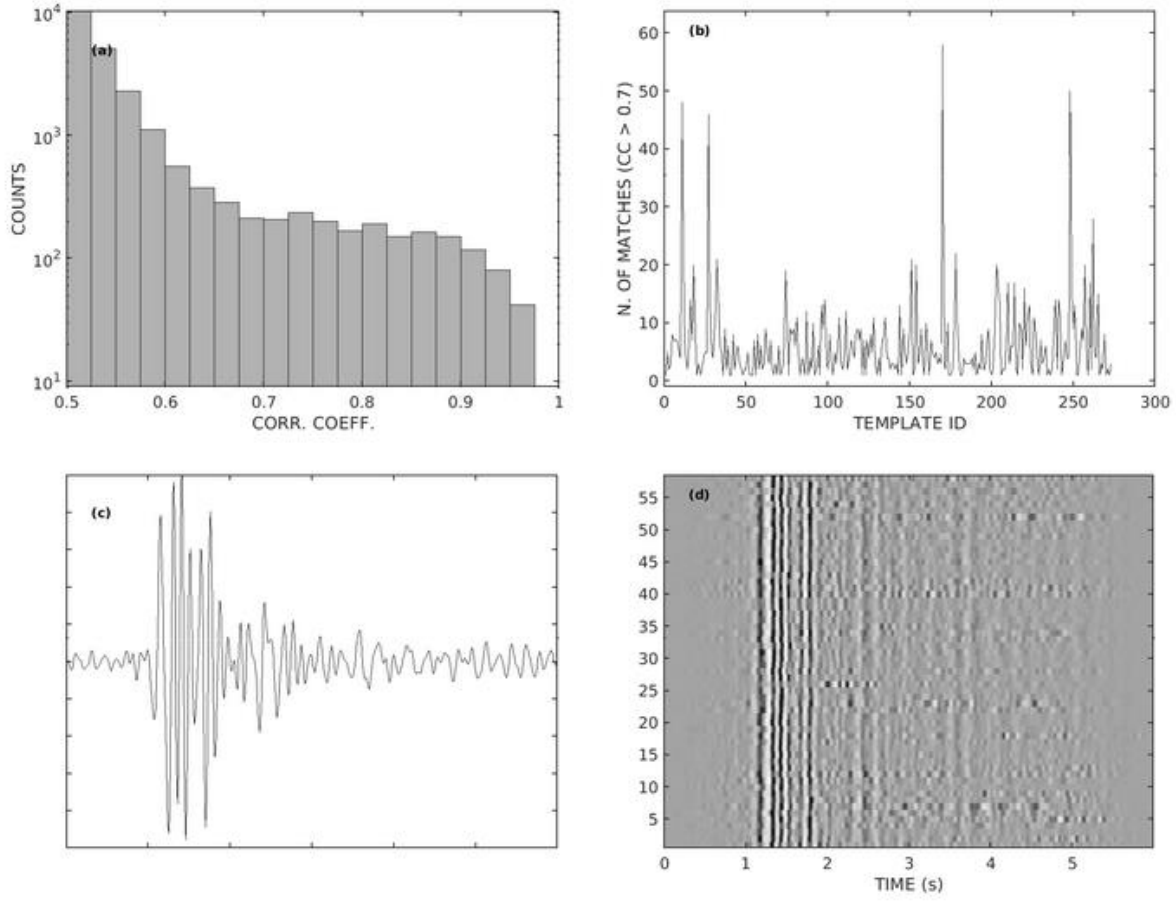


Figure 5.14: The same as in Figure 5.13, but for S-waves. a) Number of S-wave matches as a function of CC, and b) number of matches for each template. c) Seismogram of the S-wave template with the largest number of associated detections; d) the corresponding matched waveforms.

To associate P- and S-waves detected by the matched filter, I sorted the set of arrival times in chronological order, then I declared an event whenever the time difference between two consecutive times was larger than 5 s. Such a simple procedure is justified by the limited extension of the epicentral region, and the little difference of the waves' travel time to the different stations. The set of associated arrival times was finally located using NonLinLoc with the velocity model taken from Piccinini et al. (2014) and displayed in Table 2.1 of Chapter 2. In this case, I set the minimum number of phases (either P or S) to locate an earthquake equal to 5. The local magnitudes (M_L) of this dataset were then computed following Di Bona (2016) and Mele and Quintiliani (2020).

5.3.2 Results

Some indications about the detection performance of the method could be carried out by comparing the total number of matches with CC greater than 0.7 and the actual picks considered as arrival times of events. Table 5.2 shows, for the six stations used to determine the matched filter catalog, the total number of picks before associating (T), of arrivals (A, i.e. picks associated and located into events within the study area) and the percentages of picks retrieved as arrivals (% A/T) in the seismic catalogs. This is an indirect way to assess the presence of false positive picks, i.e. picks that do not contribute to event location. The shortcomings of this approach are the impossibility to consider true positive picks belonging to very low magnitude events that cannot be associated due to the low number of phases retrieved, or to events located outside the selected area (within a 10 km

radius). From Table 5.2 it is possible to state that on average the percentages obtained span between 40% and 90%. Two exceptions are stations CRCL and MOCL, which display a huge number of detections. However, only the 10% and 4% of these detections, respectively, are successfully associated and located. This occurrence is related to electronic disturbances and short-duration gaps in the data streams of those two stations, which provoked numerous false detections, particularly for the most impulsive P-wave arrivals. The catalog has 930 locations. Given the high cross-correlation thresholding, the reduced number of used stations and their proximity to the hypocentral area, I consider it rather robust and reliable.

		RONT	GAGN	CRCL	MBEN	SEI	MOCL
MATCH P	T	1008	736	3632	577	760	19380
	A	534	598	352	520	333	795
	%A/T	53%	81%	10%	90%	44%	4%
MATCH S	T	1676	1449	880	1243	1319	1457
	A	966	908	710	851	560	779
	%A/T	58%	63%	81%	68%	42%	53%

Table 5.2: For the stations used in the matched filtering technique I report the total (indicated as T) number of picks (sum of templates and matches with CC $\geq$ 0.7), the number of associated picks (as A) and the percentages of picks retrieved as arrivals (as % A/T), for both P and S phases.

Figure 5.15 and 5.16 respectively illustrate the epicentral map and temporal evolution for the matched filter catalog. Both the spatial distribution and daily earthquake rate exhibit a similar pattern to what previously shown; following the mainshock, the sequence rapidly decreased till waning by December 17. The improvement in catalog completeness brought by the matched filter procedure is better evidenced by examining the distribution of magnitudes.

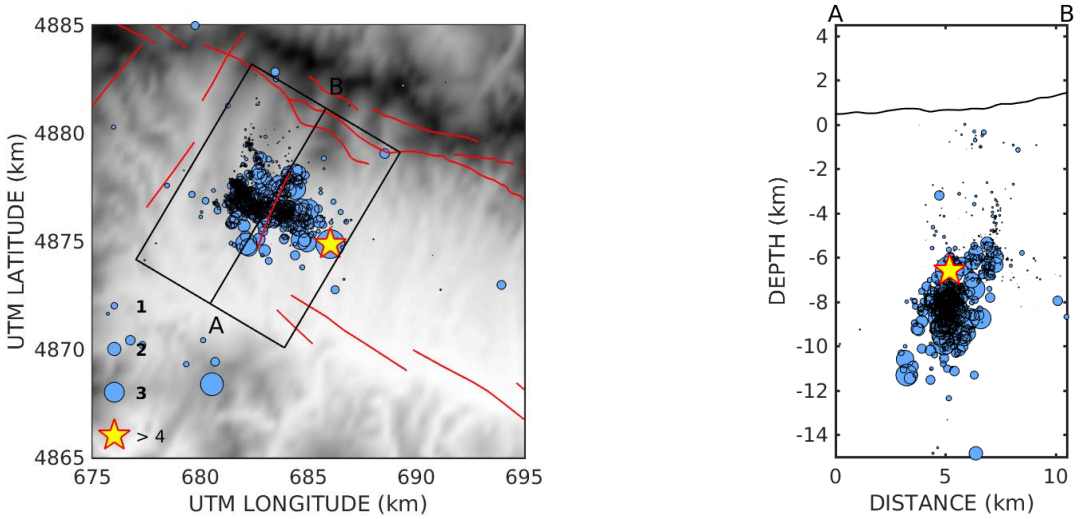


Figure 5.15: Distribution of the seismicity of the matched filter catalog regarding the 2019 sequence in map view (left) and along vertical cross section AB (right). Hypocenters are sized by magnitude, according to the scale at the bottom left of the map. The star is the mainshock.

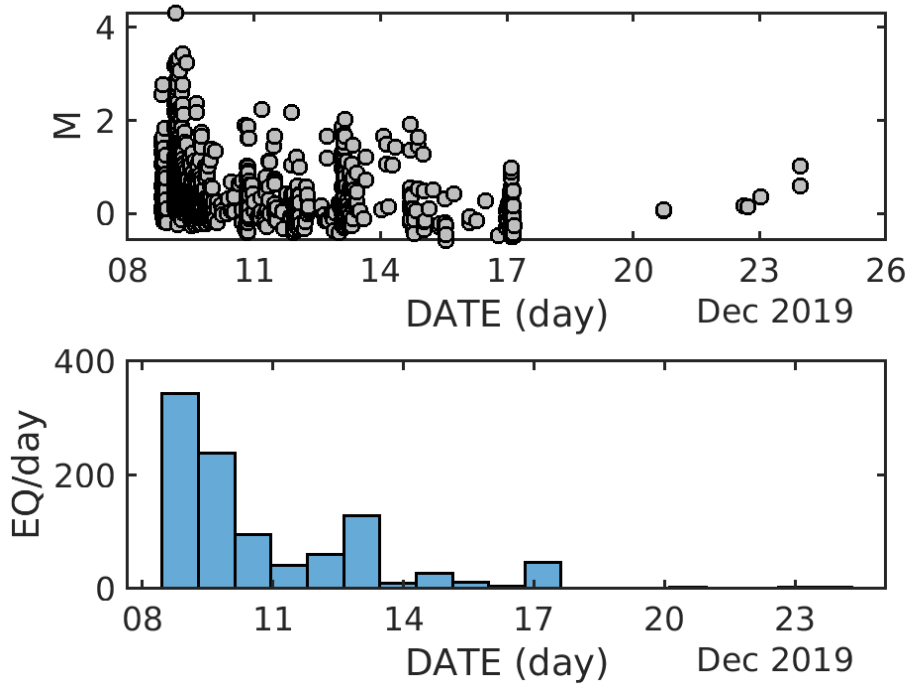


Figure 5.16: Temporal evolution of the magnitude (on top) and the daily earthquake rate (on bottom) of the matched filter catalog of the 2019 sequence.

Figure 5.17 compares the magnitude distributions and corresponding GR relationships from the 9M+INGV and matched filter catalogs, from which it emerges clearly the larger number of small-magnitude events contained by this latter data set. Such improvement is quantified by a decrease in the completeness magnitude of more than one magnitude unit, from 1.3 to 0.12 (see Table 5.3).

GR parameters	INGV (2005-2019)	9M+INGV (Dec. 2019)	Matched (Dec. 2019)
a	5.12	3.29	3.00
b	1.08	0.75	0.61
Mc	1.4	1.3	0.12

Table 5.3: Parameters of the GR relationships for the 9M+INGV and the matched filter catalogs.

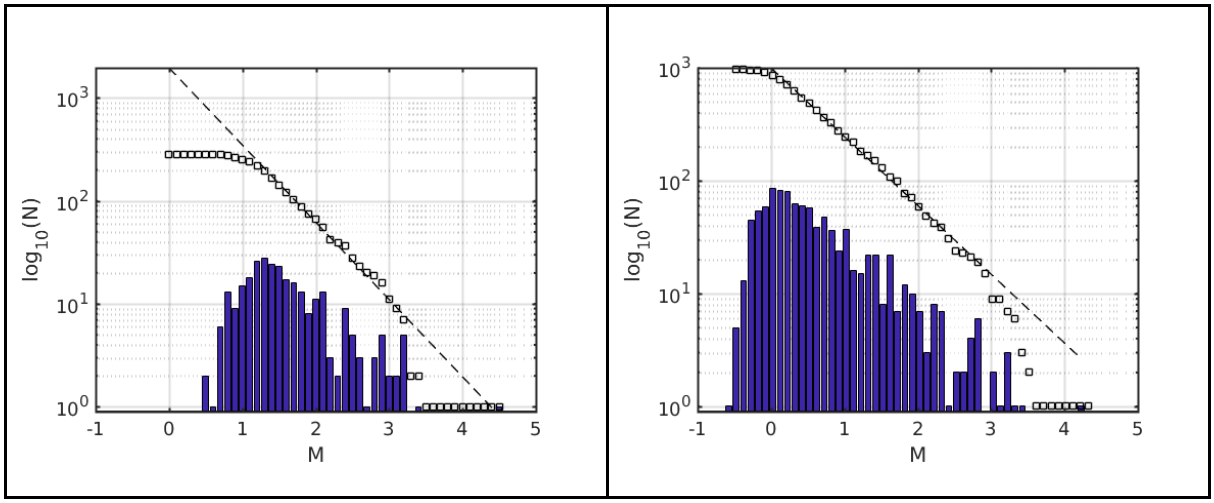


Figure 5.17: The Gutenberg–Richter law of 9M+INGV (a) and matched filter catalog (b) of the 2019 sequence. Bars are the number of earthquakes in bins of 0.1 magnitude units. The black squares are the cumulative number of earthquakes starting from the largest magnitude earthquake. The dashed line is the best-fitting line to the cumulative distribution, whose slope indicates the b-value of the distribution.

5.4 Conclusions

In this chapter I used the catalog from Chapter 2 and the data recorded by the 9M network (Chapter 3), obtaining an improved catalog from integration of those different sets of phase arrival times. This final catalog is relocated using a specific velocity model. The relocated hypocenters are clustered according to 4 main sequences during 2008, 2009, 2015 and 2019. I then also used waveform cross correlation to detect additional earthquakes during the 2019 sequence. The main findings were:

1. The high-resolution relocation of these data clearly indicates that the four main sequences that affected the study area during the past 15 years are associated with the subsequent activation of adjacent segments of a larger fault system bordering the NE sector of the Mugello basin, namely the Ronta Fault System (Sani et al., 2009);

2. The length of the surface projection of these fault segments as derived from epicenter alignment ranges in between 2 km (2009) and 4 km (2008, 2015, 2019).
3. Hypocentral depths for all the sequences are similar, spanning the 6-11 km depth interval.
4. In general, the fault strike derived from epicenters alignment are consistent with the information derived from the fault plane solutions, which in turn indicate normal faulting along structures oriented NW-SE to NNW-SSE, i.e. along the main direction of the Apennines belt.
5. The two segments located at the SE margin of the fault system (i.e., those activated during the 2019 and 2009 sequence) dip toward SW. Moving toward NW, one then encounters the fault segment activated with the 2008 sequence, which instead dips toward NE (in agreement also with what reported by Piccinini et al., 2014, and Bonini et al., 2016). The fault segment activated with the 2015 Castiglion de' Pepoli sequence has a rather vertical setting; nonetheless, the NW tip of that fault segment, activated in concomitance of a short-duration sequence in 2017, appears to dip toward the NE.
6. The 2019, 2009 and 2008 sequences are clearly correlated with the Ronta fault system; the intersection with the topography of the fault planes imaged by the hypocenter clusters correlates remarkably well with the fault traces delineated by the surface geology (Sani et al., 2009; Bonini et al., 2016).
7. Application of a matched filter technique to 2019 data from the 9M network permitted augmenting the detections by more than a factor 3, decreasing the completeness magnitude of the catalog down to Mc~0. The hypocentral distribution from this new set of locations remains unchanged, and no new features emerge.

Chapter 6

Conclusions

The general objective of this PhD project consisted of gaining an improved knowledge about the crustal structure and seismicity within and around the Mugello basin and surrounding Northern Apennines (Italy). In order to achieve this I created a merged seismicity catalog from available sources of past recording during 2005 to 2019 (Chapter 2), and then also for 2019 to 2021 from a temporary dense network around the Mugello basin which I helped to plan, deploy and manage (Chapter 3). I used the arrival times from the local seismicity catalogs to invert for both 1D and 3D velocity models for the region (Chapter 4), and also to relocate more accurately a number of seismic sequences that occurred near the Mugello basin (Chapter 5).

The following specific objectives have been achieved:

1. Realisation of an improved seismic catalog, obtained from integration of both archive (for the period 2005-2019) and newly-acquired (2019) sets of phase arrival times, which have been inverted for hypocentral location using a specific velocity model;

2. The subsequent, double-difference relocation of this data set permitted to obtain a more complete and precise picture about the space and time distribution of the seismicity. In particular, I analysed the four main sequences that affected the study area during the past 15 years; these are associated with the activation of adjacent segments of a larger NW-striking fault system. For each individual sequence, the hypocenters are clustered along surfaces consistent with the fault plane solutions, and all indicate normal faulting along structures oriented NW-SE to NNW-SSE (Apennines direction), dipping towards either the SW or the NE directions. Some of these rupture planes have clear surface geological evidence.

3. These results confirm and integrate those obtained by previous studies (e.g., Piccinini et al., 2014; Bonini et al., 2016); in particular, it emerges that the present-day seismicity is driven by the fault system bordering the NE margin of the basin (Ronta fault system). This seems to contradict previous hypotheses which attributed the origin of the 1542 and 1919 earthquakes to normal faulting along the NE-dipping Sieve fault system (DISS Working Group, 2018), which borders the SW margin of the basin;

4. The faults associated with the distinct sequences appear to be spatially separated, as indicated by the different dips exhibited by adjacent segments (e.g, the 2008 and 2009 sequences). The length of the surface projection of these fault segments is in between 2 km and 4 km, comparable to what is expected from the magnitudes of the respective mainshocks. The presence of multiple, short-length scale fault segments, make unlikely the occurrence of large magnitude events along that particular sector of the Ronta Fault system;

5. Creation of a new 3D P- and S-wave seismic velocity model for the Northern Apennines crust using the local earthquake phase arrival times. The model broadly has seismic velocities within

the range expected for continental crust. However, I imaged small-wavelength, faster than expected P-wave anomalies in the upper crust near to and striking parallel to the Apennines. Based on their ~7 km/s P-wave velocity and their orientation and position I interpret these to be a relatively shallow crystalline basement at the core of major anticlines associated with the Apennines thrust system. The images also show a distinctive deeper increase with seismic velocity and depth consistent with the base of the crust, which deepens from ~20-25 km to ~30 km beneath the Apennines. Furthermore, the seismicity at shallower depth (<15km) around the Mugello basin and along the main divide of the northern Apennines is correlated to normal faults with extensional kinematics, whereas the deeper events along the north-eastern slope of the chain are correlated to compressional kinematic related to the thrust system originated from the Moho and involving the crustal thrust.

Taken all together, these results contribute to improving the knowledge about the main structures responsible for the present-day seismicity in the study region. These observations show that there are a number of seismic sources that may potentially produce earthquakes in the Mugello area. Several aspects should be the object of future works, and in particular:

(i) Implementation of the 3D velocity model for here obtained, for relocating the bulk of the archive seismicity;

(ii) A local refinement of the velocity models, also exploiting the correlation properties of the background noise, in order to obtain an improved image of the 3D subsurface structure at the basin scale;

(iii) utilization of the data acquired by the temporary network for guiding the planned improvements of INGV's permanent seismic monitoring system in the area.

Acknowledgments

I have been extremely lucky to have had extraordinary supervisor and co-supervisors, who deserve special mentions. Firstly, I would like to thank Dr. Gilberto Saccorotti, for his advice, guidance and patience throughout my PhD. He gave me the chance to work with him and on this exciting PhD project. I would especially like to thank him for being such a good mentor that I have never stopped learning from.
I would like to express my special thanks of gratitude to Prof. Derek Keir, for always supporting me throughout my PhD. His valuable guidance and quick feedback has helped me in completing this project. I am also gratefully thankful for his encouragement and the many occasions of discussion.
I would like to earnestly acknowledge the sincere contributions and valuable time given by Prof. Federico Sani. Working with him allowed me to expand my knowledge on the geology of the study area. His final support has been fundamental for the completion of my PhD.

I have immensely benefited from my collaboration with the INGV of Pisa, which gave me the opportunity to work in its structure, using the laboratories and instruments, and with extraordinary colleagues.

I am also grateful to Prof. Jesús M. Ibáñez of the Andalusian Institute of Geophysics, University of Granada, for his research advice and supervisions during the training activity that I held entirely on-line (due to the Covid-19 restrictions), and all the members of his research group.

I would like to thank the SEIS-UK for providing the instruments used for this project and the technical support.

I would like to thank Dr. Andrea Fiaschi, member of the Fondazione PARSEC, for his genuine help and instrumental support.

I am also grateful to Dr. Giacomo Corti for his support and enthusiasm for this project.

I grateful thank the Unione Montana dei Comuni del Mugello for logistic assistance and financial support. Site RINC is sited within a forest reserve managed by Unione dei Comuni della Valdisieve.

I address heartfelt thanks to my colleagues of the INGV of Pisa. In particular, a special thanks goes to Marco Capello, the best technician that anyone would want and mentor, to Michele D'Ambrosio and Damiano Biagini to be my perfect friends of (mis)adventures and always supportive.

I am so grateful for the support of my friends and family, with special thanks to my parents, my sister and brother, always by my side. You have my gratitude for always pushing me to go further.

Finally I would like to express my immense gratitude and love to Giovanni, for his love and constant support. None of this would have been possible without you.

Bibliography

Abers, G. A. (1994). *Three-dimensional inversion of regional P and S arrival times in the East Aleutians and sources of subduction zone gravity highs.* Journal of Geophysical Research: Solid Earth, 99(B3), 4395-4412.

Amato, A., Alessandrini, B., Cimini, G., Frepoli, A., & Selvaggi, G. (1993). *Active and remnant subducted slabs beneath Italy: evidence from seismic tomography and seismicity.* In Annals of Geophysics (Vol. 36, Issue 2). Instituto Nazionale di Geofisica e Vulcanologia, INGV. https://doi.org/10.4401/ag-4272

Anelli L., Gorza M., Pieri M., and Riva M., (1994). *Subsurface well data in the Northern Apennines (Italy).* Mem. Soc. Geol. It., 48, 461-471

Barchi M.R., Minelli G., Pialli G., (1998). *The CROP 03 profile; a synthesis of results on deep structures of the Northern Apennines.* Mem. Soc. Geol. It., 52, 383–400.

Basili R., Valensise G., Vannoli P., Burrato P., Fracassi U., Mariano S., Tiberti M.M., Boschi E., (2008). *The Database of Individual Seismogenic Sources (DISS), version 3: summarizing 20 years of research on Italy's earthquake geology.* Tectonophysics 453, 20–43. Tectonophysics 453, 20–4.

Benvenuti M., Papini M., (1997). *Depositi continentali Plio-Pleistocenici nell'area di Monte Giovi. Relazioni tra l'evoluzione idrografica e la tettonica della Valdisieve (Firenze)*. Quaternario, 10, pp. 105-120.

Benvenuti M., (2003). *Facies analysis and tectonic significance of lacustrine fan-deltaic successions in the Pliocene–Pleistocene Mugello Basin, Central Italy*. Sedimentary Geology 157, 3-4, 197-234. https://doi.org/10.1016/S0037-0738(02)00234-8

Beyreuther M., Barsch R., Krischer L., Megies T., Behr Y. and Wassermann J., (2010). *ObsPy: A Python Toolbox for Seismology.* Seismological Research Letters, 81(3), 530–533. https://doi.org/10.1785/gssrl.81.3.530

Boccaletti M., Ciaranfi N., Cosentino D., Deiana G., Gelati R., Lentini F., and Tortorici L., (1990). *Palinspastic restoration and paleogeographic reconstruction of the peri-Tyrrhenian area during the Neogene.* Palaeogeography, Palaeoclimatology, Palaeoecology, 77(1), 41-IN13.

Boccaletti M., Sani F., (1998). *Cover thrust reactivations related to internal basement involvement during Neogene-Quaternary evolution of the northern Apennines.* Tectonics, 17, pp. 112-130.

Boncio P. and Lavecchia G., (2000). *A structural model for active extension in Central Italy.* J. Geodyn., 29, 233-244. https://doi.org/10.1016/S0264-3707(99)00050-2

Bonini M., Sani F., (2002). *Extension and compression in the Northern Apennines (Italy) hinterland: evidence from the late Miocene-Pliocene Siena-Radicofani Basin and relations with basement structures.* Tectonics, 21 (3), pp. 1/1-1/35. https://doi.org/10.1029/2001TC900024

Bonini M., Sani F., Stucchi E. M., Moratti G., Benvenuti M., Menanno G., and Tanini C., (2014). *Late Miocene shortening of the Northern Apennines back-arc.* Journal of Geodynamics, 74, 1-31.

Bonini M., Corti G., Delle Donne D., Sani F., Piccardi L., Vannucci G., Genco R., Martinelli L. and Ripepe M., (2016). *Seismic sources and stress transfer interaction among axial normal faults and external thrust fronts in the Northern Apennines (Italy): A working hypothesis based on the 1916–1920 time–space cluster of earthquakes.* Tectonophysics 680, 67-89. https://doi.org/10.1016/j.tecto.2016.04.045

Bortolotti V., Principi G., Treves B., (2001). *Ophiolites, ligurides and the tectonic evolution from spreading to convergence of a Mesozoic Western Tethys segment*. G.B. Vai, I.P. Martini (Eds.), Anatomy of an Orogen: The Apennines and Adjacent Mediterranean Basins, Kluwer Academic Publisher, pp. 151-164

Bruni R., Saccorotti G., Keir D., Giunchi C. and Fiaschi A., (2019). *Mugello Temporary Seismic Deployment* [Data set]. International Federation of Digital Seismograph Networks. https://doi.org/10.7914/SN/9M_2019

Capacci C., (1920). *Osservazioni geotettoniche sul terremoto mugellano del 29 Giugno 1919.* Atti della R. Acc. dei Georg., Firenze, pp. 182-194

Carannante S., Monachesi G., Cattaneo M., Amato A., and Chiarabba C., (2013). *Deep structure and tectonics of the northern-central Apennines as seen by regional-scale tomography and 3-D located earthquakes.* J. Geophys. Res. Solid Earth, 118, 5391–5403, doi:10.1002/jgrb.50371.

Carminati E., Lustrino M. and Doglioni C., (2012). *Geodynamic evolution of the central and western Mediterranean: Tectonics vs. igneous petrology constraints.* Tectonophysics. https://doi.org/10.1016/j.tecto.2012.01.026

Chiarabba C., Jovane L., Di Stefano R., (2005). *A new view of Italian seismicity using 20 years of instrumental recordings.* Tectonophysics, 395, pp. 251-268

Chiarabba C., De Gori P., and Mele F. M., (2015). *Recent seismicity of Italy: Active tectonics of the central Mediterranean region and seismicity rate changes after the Mw 6.3 L'Aquila earthquake.* Tectonophysics, 638, 82-93.

Delle Donne D., (2005). *Tettonica attiva dell'Appennino Settentrionale nel settore compreso tra l'Appennino Pistoiese e l'alta Val Tiberina.* PhD Thesis University of Florence, 144 pp.

Devoti R., Esposito A., Pietrantonio G., Pisani A.R., Riguzzi F., (2011). *Evidence of large scale deformation patterns from GPS data in the Italian subduction boundary.* Earth and Planetary Science Letters 311, 3-4, 230-241. https://doi.org/10.1016/j.epsl.2011.09.034

Devoti R., and Riguzzi F., (2018). *The velocity field of the Italian area.* Rendiconti Lincei. Scienze Fisiche e Naturali 29, 1, 51-58. https://doi.org/10.1007/s12210-017-0651-x

Di Bona M., (2016). *A local magnitude scale for crustal earthquakes in Italy.* Bulletin of the Seismological Society of America, 106(1), 242-258. https://doi.org/10.1785/0120150155

DISS Working Group (2018). *Database of Individual Seismogenic Sources (DISS), Version 3.2.1: A compilation of potential sources for earthquakes larger than M 5.5 in Italy and surrounding areas.* http://diss.rm.ingv.it/diss/, Istituto Nazionale di Geofisica e Vulcanologia; doi:10.6092/INGV.IT-DISS3.2.1

Di Stefano R., E. Kissling, C. Chiarabba, A. Amato, and D. Giardini, (2009). *Shallow subduction beneath Italy: Three-dimensional images of the Adriatic-European-Tyrrhenian lithosphere system based on high-quality Pwave arrival times.* J. Geophys. Res., 114, B05305, doi:10.1029/2008JB005641.

Di Stefano R., Bianchi I., Ciaccio M.G., Carrara G., Kissling E., (2011). *Three-dimensional Moho topography in Italy: new constraints fromm receiver functions and controlled source seismology.* Geochem. Geoph. Geosys. 12, Q09006, http://dx.doi.org/10.1029/2011GC003649.

Finetti, I. R., Boccaletti, M., Bonini, M., Del Ben, A., Geletti, R., Pipan, M., & Sani, F. (2001). Crustal section based on CROP seismic data across the North Tyrrhenian–Northern Apennines–Adriatic Sea. *Tectonophysics*, *343*(3-4), 135-163.

Finetti I.R., Boccaletti M., Bonini M., Del Ben A., Pipan M., Prizzon A., Sani F., (2005). *Lithospheric tectono-stratigraphic setting of the Ligurian Sea-northern Apennines-Adriatic foreland from integrated CROP seismic data.* I.R. Finetti (Ed.), CROP PROJECT: Deep Seismic Exploration of the Central Mediterranean and Italy, Atlases in Geosciences, vol. 1, Elsevier, pp. 119-158 Chapter 8.

Frepoli A., and Amato A., (1997). *Contemporaneous extension and compression in the Northern Apennines from earthquake fault-plane solutions.* Geophysical Journal International, 129(2), 368-388.

Galli P., Meloni F., (1993). *Nuovo catalogo dei processi di liquefazione avvenuti in occasione dei terremoti storici in Italia.* Quaternario, 6 (2), pp. 271-292

Goldstein P., and Snoke A., (2005), *"SAC Availability for the IRIS Community"*, Incorporated Institutions for Seismology Data Management Center Electronic Newsletter.

Goldstein P., Dodge D., Firpo M., Minner Lee, (2003). *"SAC2000: Signal processing and analysis tools for seismologists and engineers, Invited contribution to "The IASPEI International Handbook of Earthquake and Engineering Seismology"*, Edited by WHK Lee, H. Kanamori, P.C. Jennings, and C. Kisslinger, Academic Press, London.

Graeber F. M., and Asch G., (1999). *Three-dimensional models of P wave velocity and P-to-S velocity ratio in the southern central Andes by simultaneous inversion of local earthquake data.* Journal of Geophysical Research: Solid Earth, 104(B9), 20237-20256.

Gutenberg B., and Richter C. F., (1944). *Frequency of earthquakes in California.* Bulletin of the Seismological Society of America, 34(4), 185-188.

Hardebeck J. L., and Shearer P. M., (2002). *A new method for determining first-motion focal mechanisms.* Bulletin of the Seismological Society of America, 92(6), 2264-2276. http://dx.doi.org/10.1785/0120010200

Hardebeck J.L. and Shearer P.M., (2009). *A New Method for Determining First-Motion Focal Mechanisms.* Bulletin of the Seismological Society of America, 92, 2264–2276. https://doi.org/10.1785/0120010200

Improta L., and Corciulo M., (2006). *Controlled Source Nonlinear Tomography: A Powerful Tool to Constrain Tectonic Models of the Southern Apennines Orogenic Wedge, Italy.* Geology, vol. 34, no. 11, p. 941. https://doi.org/10.1130/G22676A.1.

INGV Seismological Data Centre. (2006). *Rete Sismica Nazionale (RSN)*. Istituto Nazionale di Geofisica e Vulcanologia (INGV), Italy. https://doi.org/10.13127/SD/X0FXnH7QfY

ISIDe Working Group. (2007). *Italian Seismological Instrumental and Parametric Database (ISIDe).* Istituto Nazionale di Geofisica e Vulcanologia (INGV). https://doi.org/10.13127/ISIDE

Kanamori H., (1977). *The energy release in great earthquakes.* Journal of geophysical research, 82(20), 2981-2987. https://doi.org/10.1029/JB082i020p02981

Krischer L., Megies T., Barsch R., Beyreuther M., Lecocq T., Caudron C. and Wassermann J., (2015). *ObsPy: a bridge for seismology into the scientific Python ecosystem.* Computational Science & Discovery, 8(1), 014003. https://doi.org/10.1088/1749-4699/8/1/014003

Lahr J. C., (1989). *HYPOELLIPSE/version 2.0; a computer program for determining local earthquake hydrocentral parameters, magnitude, and first motion pattern.* In Open-File Report. US Geological Survey. https://doi.org/10.3133/ofr89116

Leonard, M. (2014). *Self-consistent earthquake fault-scaling relations: Update and extension to stable continental strike-slip faults.* Bulletin of the Seismological Society of America, 104(6), 2953-2965. https://doi.org/10.1785/0120140087

Lomax A., Michelini A., Curtis A., (2009). *Earthquake Location, Direct, Global-Search Methods, in Complexity* In Encyclopedia of Complexity and System Science, Part 5, Springer, New York, pp. 2449-2473, doi:10.1007/978-0-387-30440-3. (www.springerlink.com)

Luckett R., and Baptie B., (2015). *Local earthquake tomography of Scotland.* Geophysical Journal International, 200(3), 1538–1554. https://doi.org/10.1093/gji/ggu489

Maestrelli D., Benvenuti M., Bonini M., Carnicelli S., Piccardi L., Sani F., (2018). *The structural hinge of a chain-foreland basin: Early Pleistocene to recent activity of the Pede-Apennine Thrust front (Northern Italy).* Tectonophysics. 723, 117–135. https://doi:10.1016/j.tecto.2017.12.006.

Maggi C., Frepoli A., Cimini G. B., Console R., and Chiappini M., (2009). *Recent seismicity and crustal stress field in the Lucanian Apennines and surrounding areas (Southern Italy): Seismotectonic implications.* Tectonophysics, 463(1-4), 130-144. https://doi.org/10.1016/j.tecto.2008.09.032

Marroni, M., Meneghini, F., & Pandolfi, L. (2017). *A revised subduction inception model to explain the Late Cretaceous, double-vergent orogen in the precollisional western Tethys: Evidence from the Northern Apennines.* Tectonics, 36.https://doi.org/10.1002/2017TC004627

Martelli L., Ercolessi G., Molinari F. C., Calabrese L., Severi P., Bonini M., Corti G., Piccardi L., Sani F., Pondrelli S., (2017). *Carta sismotettonica della Regione Emilia-Romagna e aree limitrofe.* Ediz. Regione Emilia-Romagna, Servizio Geologico Sismico e dei Suoli. URL:https://ambiente.regione.emilia-romagna.it/it/geologia/pubblicazioni/cartografia-geo-tematica/carta-sismotettonica-della-regione-emilia-romagna-e-aree-limitrofe-edizione-2016

Martini I.P., Sagri M., (1993). *Tectono-sedimentary characteristics of late Miocene-Quaternary extensional basins of the Northern Apennines, Italy.* Earth-Sci. Rev., 34, pp. 197-233

Martini I.P., Sagri M., Colella A., (2001). *Neogene-Quaternary basins of the inner Apennines and Calabrian arc.* G.B. Vai, I.P. Martini (Eds.), Anatomy of an Orogen: The Apennines and Adjacent Mediterranean Basins, Kluwer Academic Publisher, pp. 375-400

McNamara D. E., and Buland R. P., (2004). *Ambient noise levels in the continental United States.* Bulletin of the seismological society of America 94.4: 1517-1527. https://doi.org/10.1785/012003001

McNamara D. E. and Boaz R. I., (2006). *Seismic noise analysis system using power spectral density probability density functions: A stand-alone software package*. US Geological Survey. Open-File Report 2005-1438.

Megies T., Beyreuther M., Barsch R., Krischer L. and Wassermann J.. (2011). *ObsPy – What can it do for data centers and observatories?.* Annals of Geophysics, 54(1). https://doi.org/10.4401/ag-4838

Mele F. M., and Quintiliani M., (2020). *Correzioni di stazione per il calcolo della Magnitudo Locale in Italia (aggiornate alla configurazione della Rete Sismica Nazionale di giugno 2018).* Rapp. Tec. INGV, 413, 1-60.

Menke W., 1989. *Geophysical data analysis: discrete inverse theory.* rev. edn, Academic Press, San Diego

Parker R. L. and Parker, R. L. (1994). *Geophysical inverse theory* (Vol. 1). Princeton university press.

Peterson J. R., (1993). *Observations and modeling of seismic background noise*. US Geological Survey Open-File Report 93-322.

Piana Agostinetti N., and Amato A., (2009), *Moho depth and Vp / Vs ratio in peninsular Italy from teleseismic receiver functions*, J. Geophys. Res., 114, B06303, doi:10.1029/2008JB005899.

Piccinini, D., Piana Agostinetti N., Saccorotti G., Fiaschi A., Matassoni L., Morelli M., (2014). *Orogen-parallel variability in 3D seismicity distribution, Northern Apennines (Italy): Evidence for a slab tear fault?*. Journal of Geodynamics 82, 110-117. https://doi.org/10.1016/j.jog.2014.09.005

Podvin P. and Lecomte I., (1991). *Finite difference computation of traveltimes in very contrasted velocity models: a massively parallel approach and its associated tools.* Geophysical Journal International, 105(1), 271-284. https://doi.org/10.1111/j.1365-246X.1991.tb03461.x

Pondrelli S., Morelli A., Ekstrom G., Mazza S., Boschi E., Dziewonski A.M., (2002). *European-Mediterranean regional centroid moment tensors: 1997–2000.* Phys. Earth Planet. Int., 130, pp. 71-101

Pondrelli S., Salimbeni S., Morelli A., Ekstrom G., (2006). *European-Mediterranean Regional Centroid Moment Tensor catalog: solutions for years 2003 and 2004.* Phys. Earth Planet. Int., 159 (3–4), pp. 286-303, 10.1016/j.pepi.2006.07.008

Pontoise, B., and Monfret, T. (2004). *Shallow seismogenic zone detected from an offshore-onshore temporary seismic network in the Esmeraldas area (northern Ecuador).* Geochemistry, Geophysics, Geosystems, 5(2).

Ponziani F., De Franco R., Minelli G., Biella G., Federico C., Pialli G., (1995). *Crustal shortening and duplication of the Moho in the Northern Apennines: a view from seismic refraction data.* Tectonophysics 252, 391–418.

Rawlinson N., and Sambridge M., (2003). *Seismic traveltime tomography of the crust and lithosphere.* Advances in geophysics, 46, 81-199.

Rawlinson N., Pozgay S., Fishwick S., (2010). *Seismic tomography: A window into deep Earth.* Physics of the Earth and Planetary Interiors. 178. 101-135. 10.1016/j.pepi.2009.10.002.

Ricci Lucchi F., (1986). *The Oligocene to recent foreland basins of the Northern Apennines.* Spec. Publs. Int. Ass. Sediment., 8, pp. 105-139

Ricci Lucchi F., (1987). *Semi-allochthonous sedimentation in the Apenninic thrust belt.* Sediment. Geol., 50, pp. 119-134. https://doi.org/10.1016/0037-0738(87)90030-3

Rovida A. N., Locati M., Camassi M., Lolli B., Gasperini P., (2016). *CPTI15, the 2015 version of the Parametric Catalogue of Italian Earthquakes.* Istituto Nazionale di Geofisica e Vulcanologia. http://doi.org/10.6092/INGV.IT-CPTI15

Rovida A., Locati M., Camassi R., Lolli B., Gasperini P., Antonucci A., (2021). *Catalogo Parametrico dei Terremoti Italiani (CPTI15), versione 3.0.* Istituto Nazionale di Geofisica e Vulcanologia (INGV). https://doi.org/10.13127/CPTI/CPTI15.3

Sambridge M., *Geophysical inversion with a neighbourhood algorithm—I. Searching a parameter space*, Geophysical Journal International, Volume 138, Issue 2, August 1999, Pages 479–494, https://doi.org/10.1046/j.1365-246X.1999.00876.x

Sani F., Bonini M., Piccardi L., Vannucci G., Delle Donne D., Benvenuti M., Moratti G., Corti G., Montanari D., Sedda L., Tanini C., (2009). *Late Pliocene–Quaternary evolution of outermost hinterland basins of the Northern Apennines (Italy), and their relevance to active tectonics.* Tectonophysics 476, 1-2, 336-356. https://doi.org/10.1016/j.tecto.2008.12.012

Sani F., Bonini M., Montanari D., Moratti G., Corti G., and Del Ventisette C., (2016). *The structural evolution of the Radicondoli–Volterra Basin (southern Tuscany, Italy): Relationships with magmatism and geothermal implications.* Geothermics, 59, 38-55. https://doi.org/10.1016/j.geothermics.2015.10.008

Scafidi D., Solarino S., Eva C., (2009). *P wave seismic velocity and Vp/Vs ratio beneath the Italian peninsula from local earthquake tomography.* Tectonophysics, 465, 1–23, http://dx.doi.org/10.1016/j.tecto.2008.07.013.

Shapiro S. A., Huenges E., and Borm G., (1997). Estimating the crust permeability from fluid-injection-induced seismic emission at the KTB site: Geophys. J. Internat., 131, F15–F18.

Smithson S. B., Shive P. N., and Brown S. K., (1977). *Seismic velocity, reflections, and structure of the crystalline crust.* In The Earth's crust (Vol. 20, pp. 254-270). Washington, DC: American Geophysical Union.

Talwani P. and Acree S., (1985). *Pore pressure diffusion and the mechanism of reservoir-induced seismicity.* In Earthquake prediction (pp. 947-965). Birkhäuser, Basel.

Tarantola A. and Valette B., (1982). *Inverse problems= quest for information.* Journal of geophysics, 50(1), 159-170. https://n2t.net/ark:/88439/y048722

Tarantola, A. J. N. Y. (1987). *Inverse Problem Theory Elsevier*. New York.

Tarquini S., Isola I., Favalli M., Mazzarini F., Bisson M., Pareschi M. T., Boschi E., (2007). *TINITALY/01: a new Triangular Irregular Network of Italy*, Annals of Geophysics 50, 407 - 425. http://hdl.handle.net/2122/3673

Tarquini S., Vinci S., Favalli M., Doumaz F., Fornaciai A., Nannipieri L., (2012). *Release of a 10-m-resolution DEM for the Italian territory: Comparison with global-coverage DEMs and anaglyph-mode exploration via the web*, Computers & Geosciences 38, 168-170. https://doi.org/10.1016/j.cageo.2011.04.018

Tinti S. and Mulargia F., (1985). *Effects of magnitude uncertainties on estimating the parameters in the Gutenberg-Richter frequency-magnitude law*. Bull. Seismol. Soc. Amer., 75, 1681—1697.

Vidale J. E. and Shearer P. M., (2006). *A survey of 71 earthquake bursts across southern California: Exploring the role of pore fluid pressure fluctuations and aseismic slip as drivers*, J. Geophys. Res., 111, B05312, doi:10.1029/2005JB004034.

Wells D.L., and K.J. Coppersmith, (1994). *New Empirical Relationships among Magnitude, Rupture Length, Rupture Width, Rupture Area, and Surface Displacement.* Bulletin of the Seismological Society of America, Vol. 84, No. 4, pp. 974-1002, August 1994

Wiemer S. and Wyss M., (2000). *Minimum magnitude of completeness in earthquake catalogs: Examples from Alaska, the western United States, and Japan.* Bulletin of the Seismological Society of America, 90(4), 859-869.

Wiemer S., (2001). *A software package to analyze seismicity: ZMAP*. Seismological Research Letters, 72(3), pp.373-382. https://doi.org/10.1785/gssrl.72.3.373

Supplementary materials

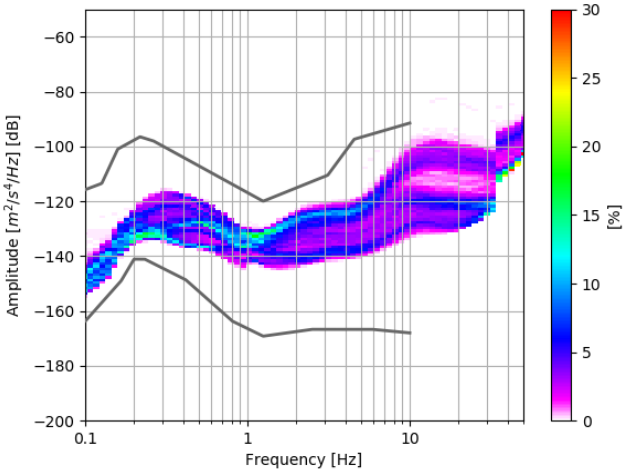
1. Station datasheets

Station ID	**RONT**
Municipality	Borgo San Lorenzo
Local Area	Le Ville (Ronta Campagna)
Latitude (° WGS84)	43.99354
Longitude (° WGS84)	11.43295
Altitude (m.s.l.m)	341
Geology	VILa (Continental Deposits)
Soil	Polygenic Conglomerates
Power	5 solar panels (4 of 36W + 1 of 100W)
UMTS coverage	-109 dB
Sensor	T4A96/D0504
Datalogger	DCM-911
Installation date	30/05/2019
Removal date	21/05/2021

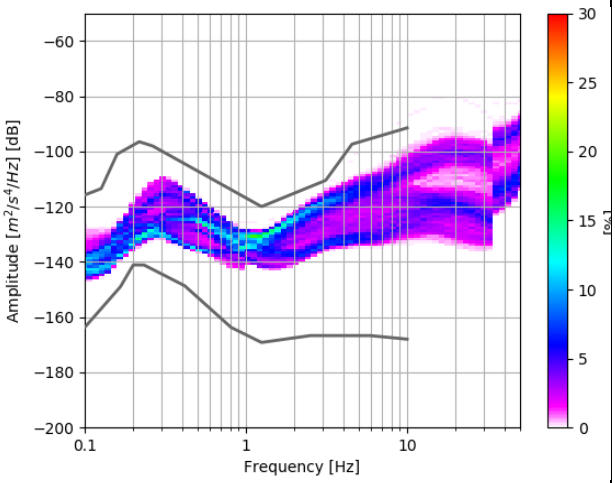

20 m
100 ft
1 : 2.000


20 m
100 ft
1 : 2.000

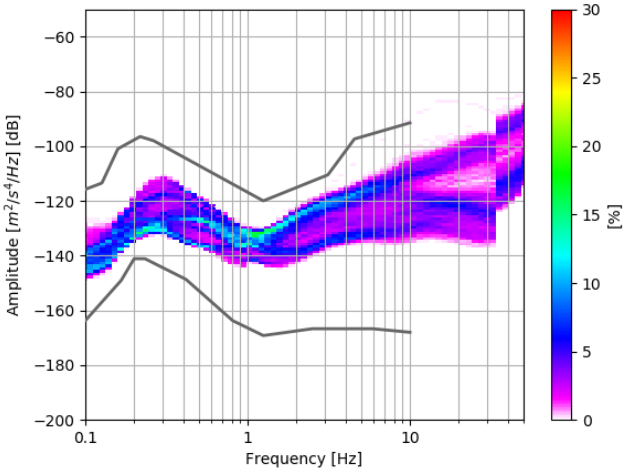



Amplitude [m²/s⁴/Hz] [dB]
Frequency [Hz]
[%]

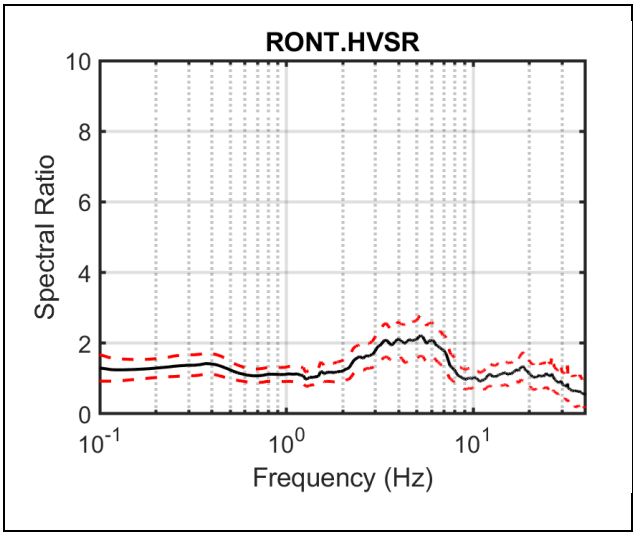
HHZ

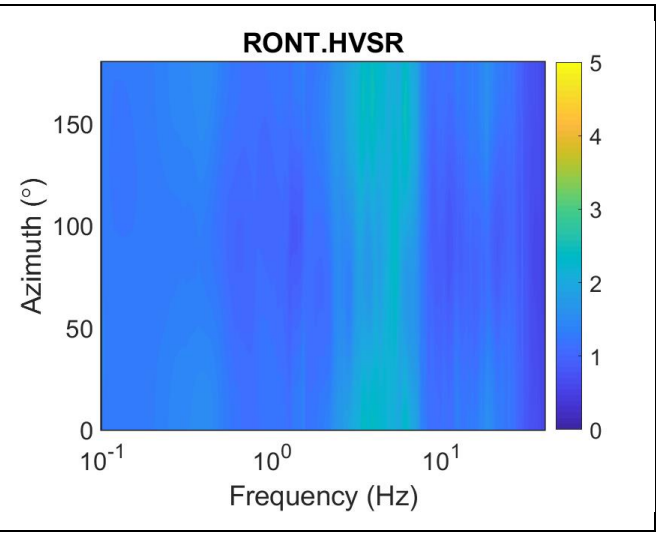

Amplitude [m²/s⁴/Hz] [dB]
Frequency [Hz]
[%]

HHE

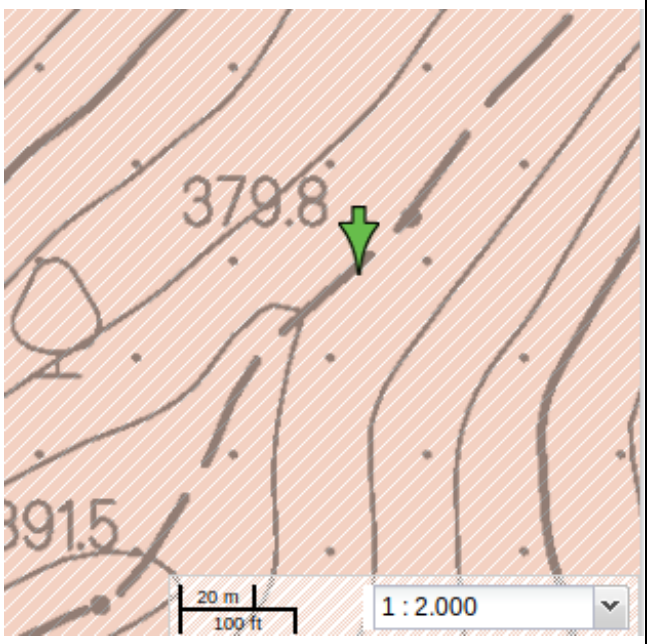
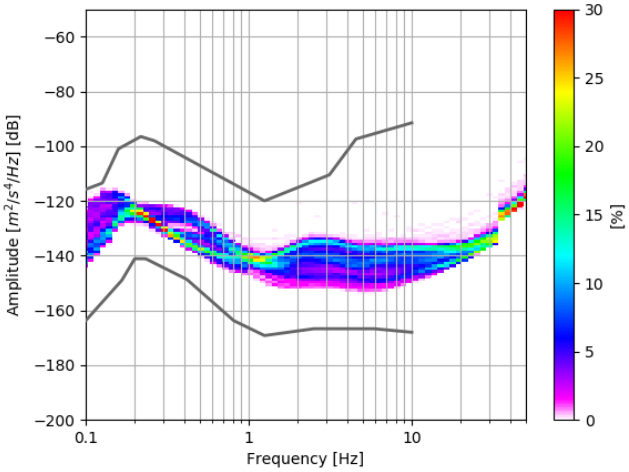
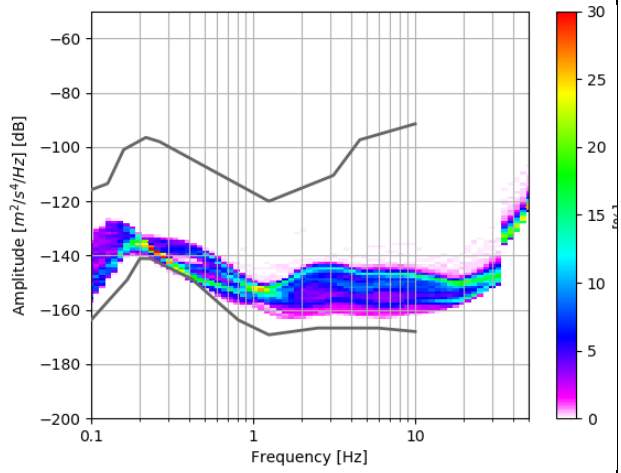
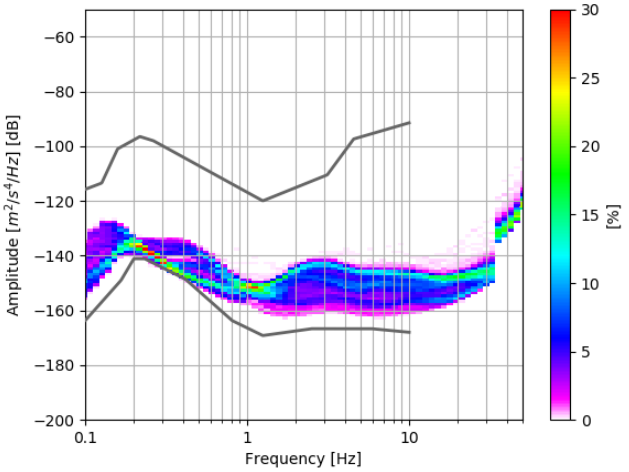

Amplitude [m²/s⁴/Hz] [dB]
Frequency [Hz]
[%]

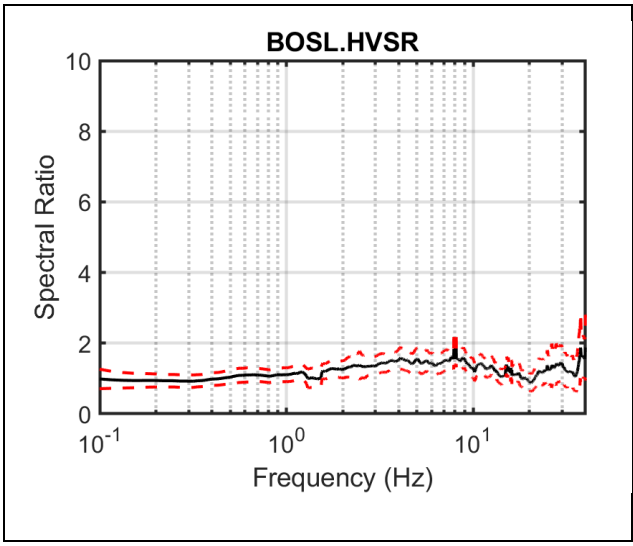
HHN

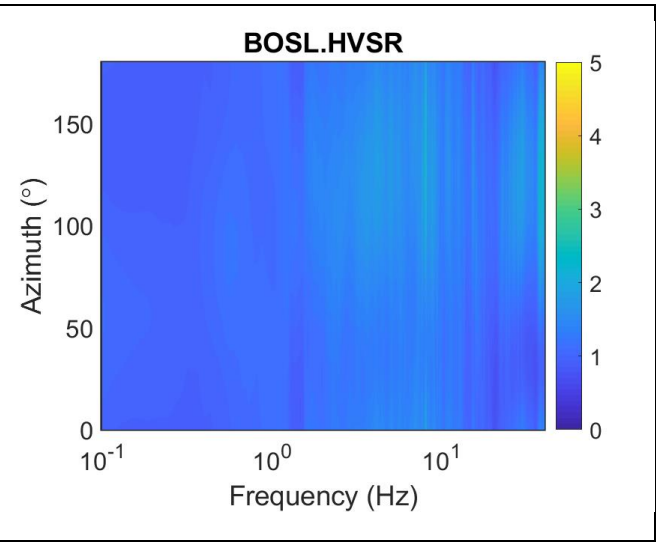




Station ID	**BOSL**
Municipality	Borgo San Lorenzo
Local Area	Borgo San Lorenzo
Latitude (° WGS84)	43.93093
Longitude (° WGS84)	11.37433
Altitude (m.s.l.m)	380
Geology	FAL4 (Membro di Lonnano, siltiti e arenarie)
Soil	Arenarie di Monte Falterona
Power	2 solar panels of 100W
UMTS coverage	-109 dB
Sensor	T4A82/D0491
Second sensor	CMG40-T 1s
Datalogger	DCM-856
Second datalogger	TAURUS Nanometrics
Installation date (first instruments)	11/05/2019 - 11/06/2019
Changing instrument date	11/06/2019

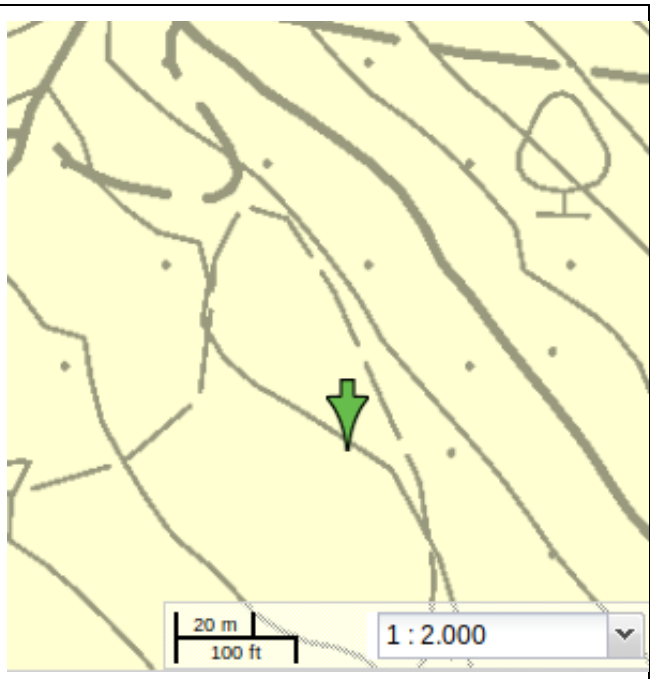
Removal date	30/05/2021
	
	 HHZ
 HHE	 HHN



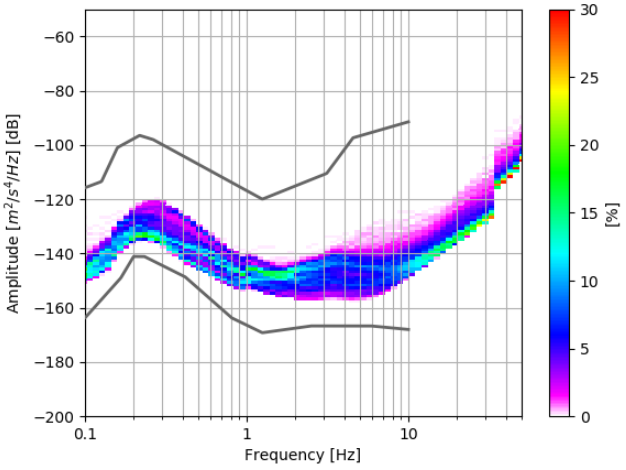


Station ID	**VISG**
Municipality	Firenzuola
Local Area	Visignano
Latitude (° WGS84)	44.18896
Longitude (° WGS84)	11.43431
Altitude (m.s.l.m)	727
Geology	FMA12 (Membro di Castel del Rio)
Soil	Formazione marnoso-arenacea
Power	2 solar panels of 150W
UMTS coverage	-89 dB
Sensor	T4A94/D0502
Datalogger	DCM-904
Installation date	12/06/2019
Removal date	30/05/2021

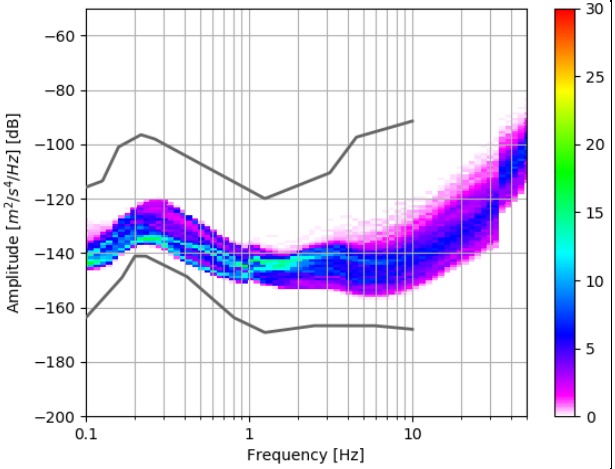

20 m
100 ft
1 : 2.000


20 m
100 ft
1 : 2.000

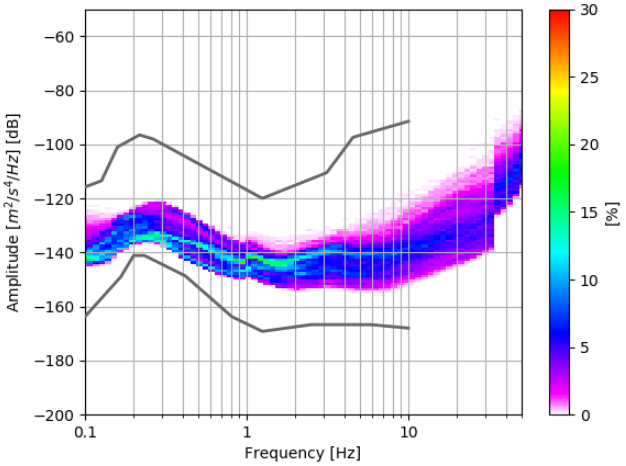



Amplitude [m²/s⁴/Hz] [dB]
Frequency [Hz]
[%]

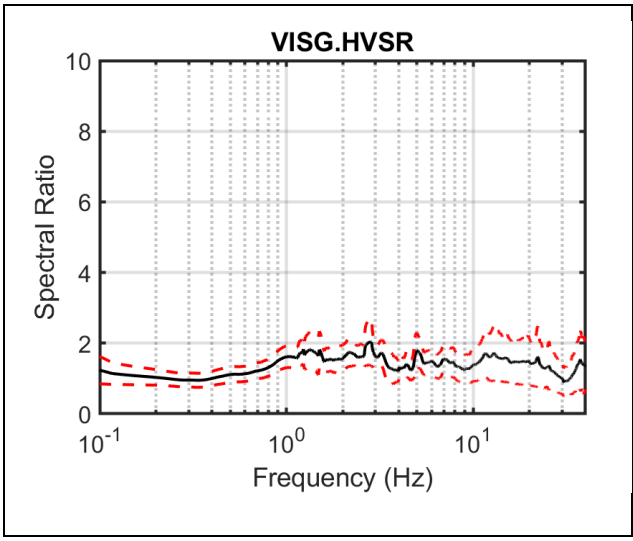
HHZ

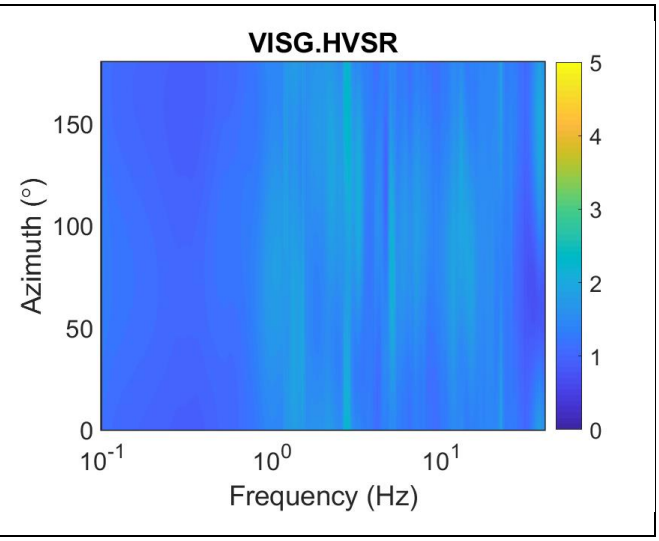

Amplitude [m²/s⁴/Hz] [dB]
Frequency [Hz]

HHE

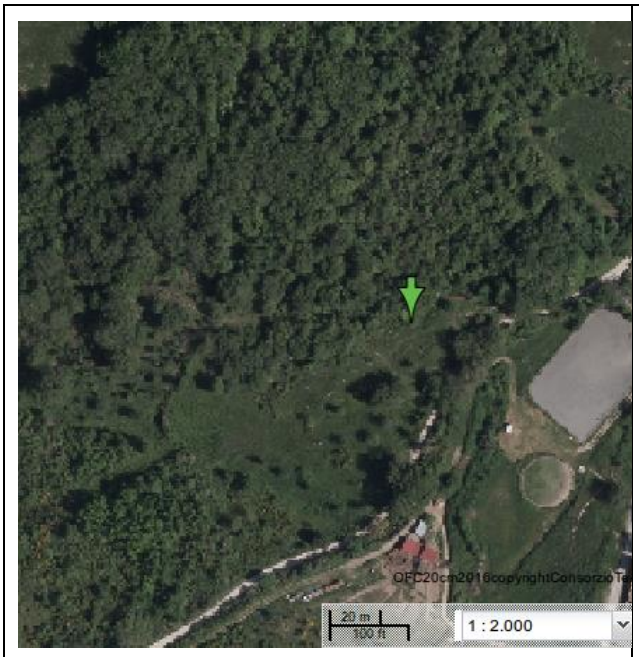

Amplitude [m²/s⁴/Hz] [dB]
Frequency [Hz]
[%]

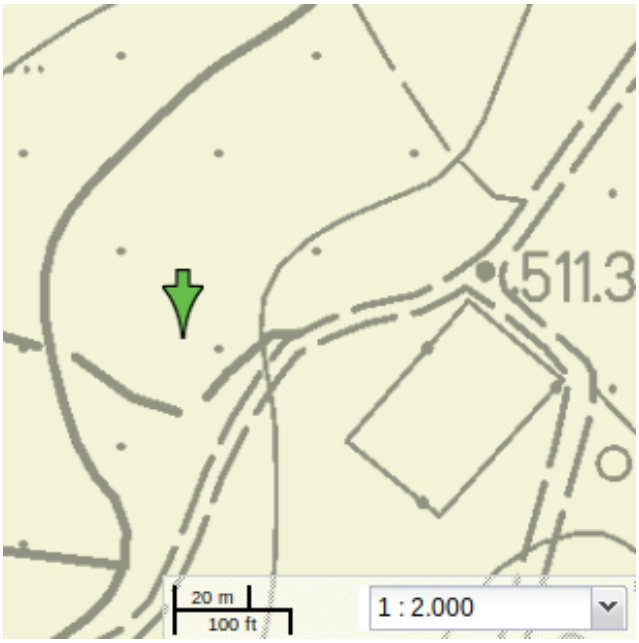
HHN



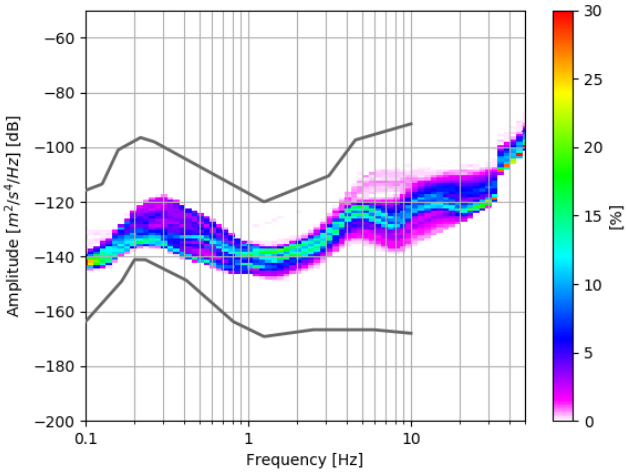


Station ID	**CRCL**
Municipality	Croci di Calenzano
Local Area	I Cavalieri del Colle, Via di Cupo
Latitude (° WGS84)	43.944353
Longitude (° WGS84)	11.237515
Altitude (m.s.l.m)	506
Geology	MLL (M. Morello Formation)
Soil	Carbonatic flysch, limestone (calcari) marnosi e marne
Power	4 solar panels 36W
UMTS coverage	-97dB
Sensor	T4902/DC30
Datalogger	EAM-2104
Installation date	20/06/2019
Removal date	21/05/2021

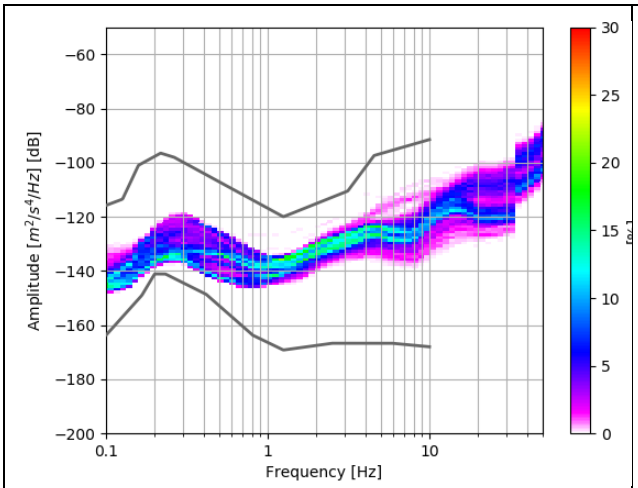

20 m
100 ft
1 : 2.000


511.3
20 m
100 ft
1 : 2.000

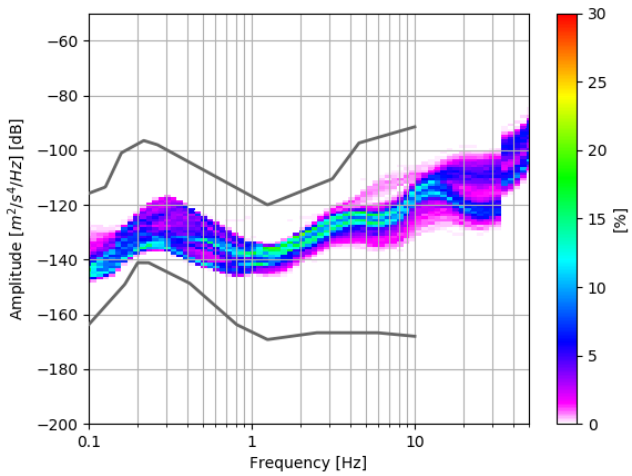



Amplitude [m²/s⁴/Hz] [dB]
−60
−80
−100
−120
−140
−160
−180
−200
0.1
1
10
Frequency [Hz]
30
25
20
15
10
5
0
[%]

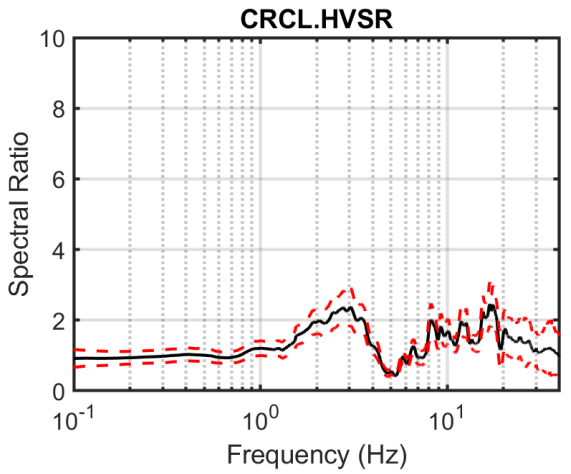
HHZ

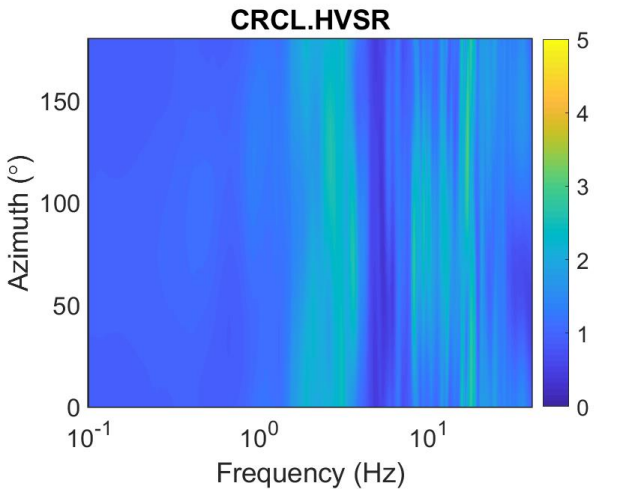


HHE

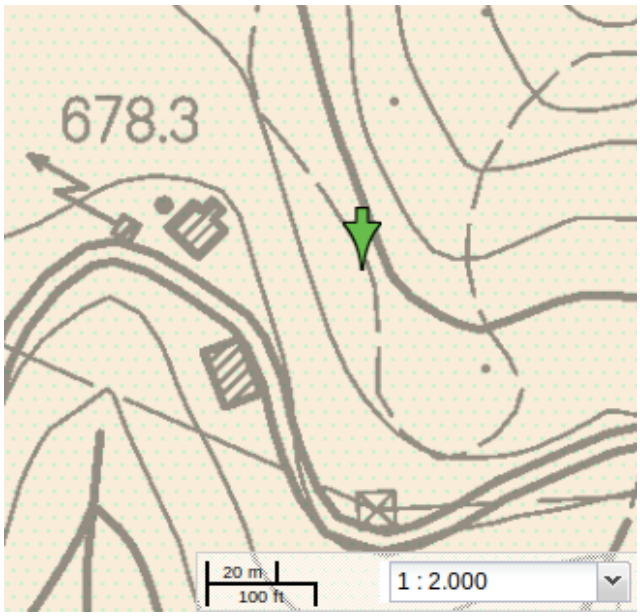
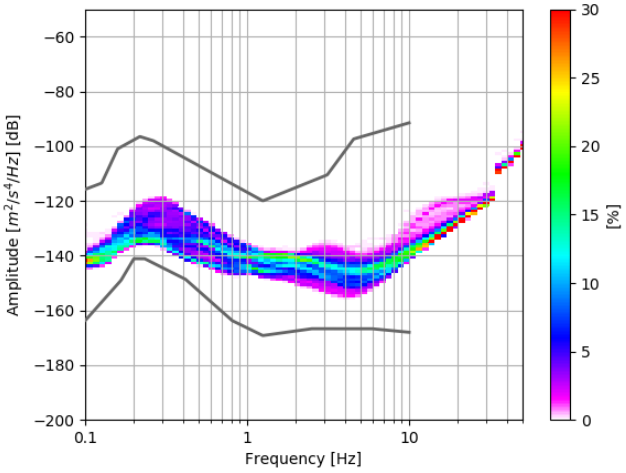


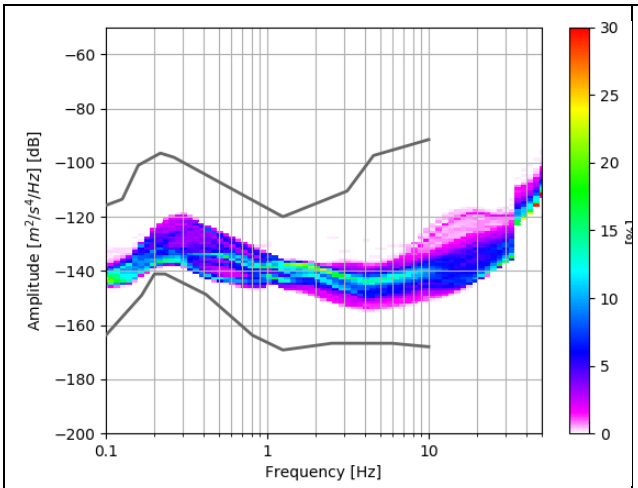
HHN



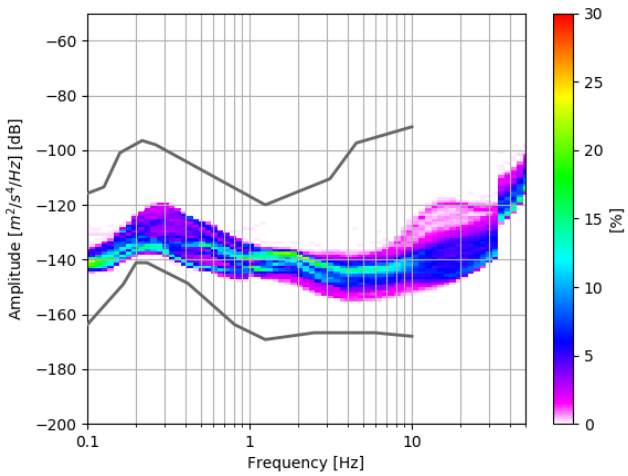


Station ID	**GAGN**
Municipality	Cavarzano
Local Area	Gagnaia
Latitude (° WGS84)	44.05697
Longitude (° WGS84)	11.11862
Altitude (m.s.l.m)	670
Geology	TCG1 (Membro a megastrati arenacei)
Soil	Torbiditi arenaceo pelitiche e silitico pelitiche
Power	4 solar panels 36W

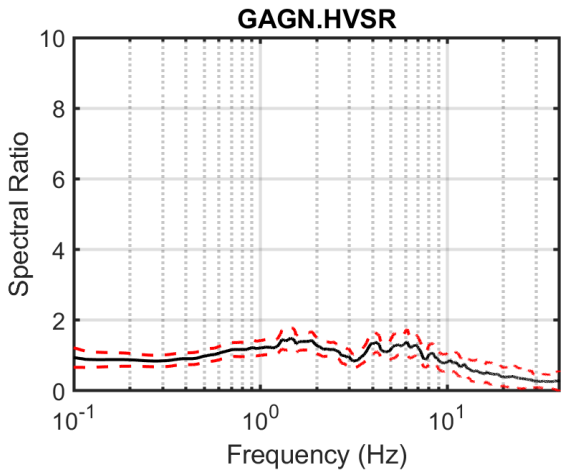
UMTS coverage	-96dB
Sensor/Digitiser	T4A90/DB65
Datalogger	DCM-935
Installation date	26/06/2019
Removal date	17/05/2021
	
	 HHZ

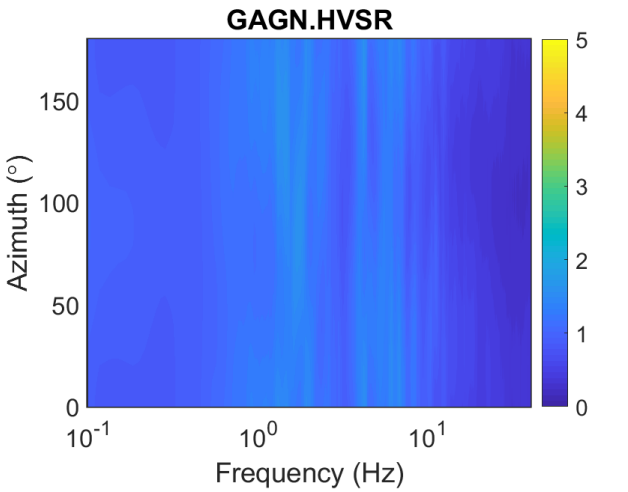


HHE

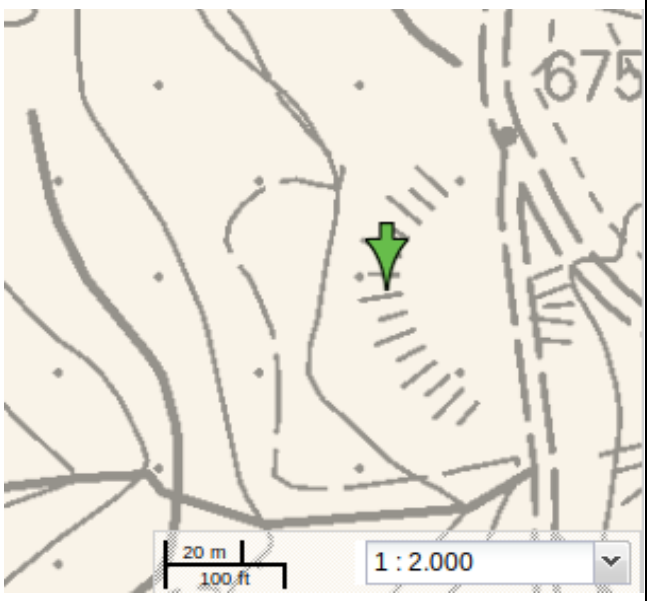
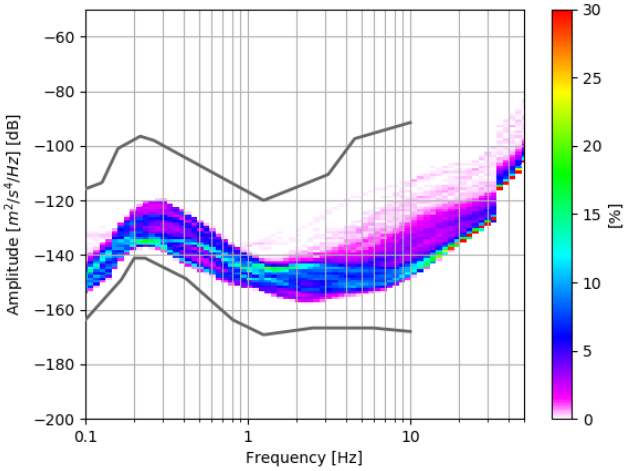


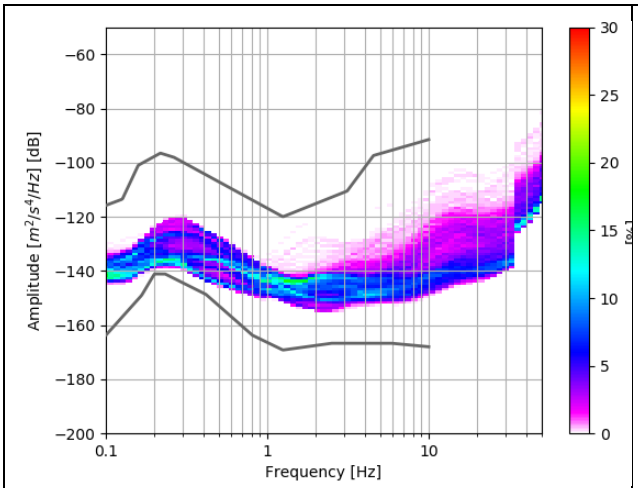
HHN



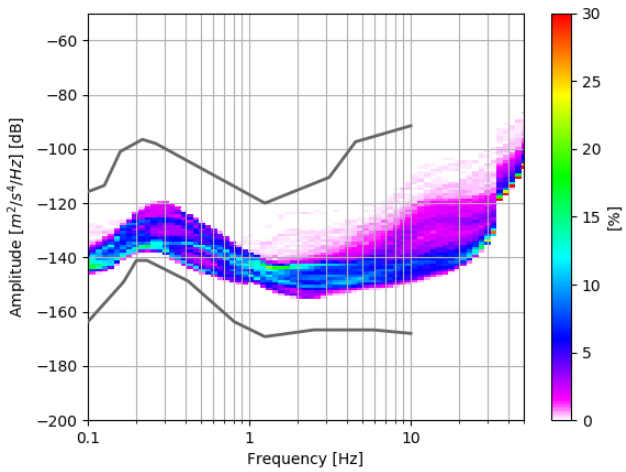


Station ID	**CFER**
Municipality	Borgo San Lorenzo
Local Area	Località Campestri, Collefertile
Latitude (° WGS84)	43.88798
Longitude (° WGS84)	11.42189
Altitude (m.s.l.m)	673
Geology	VIC (Marne di Vicchio)
Soil	Marne siltose e marne calcaree

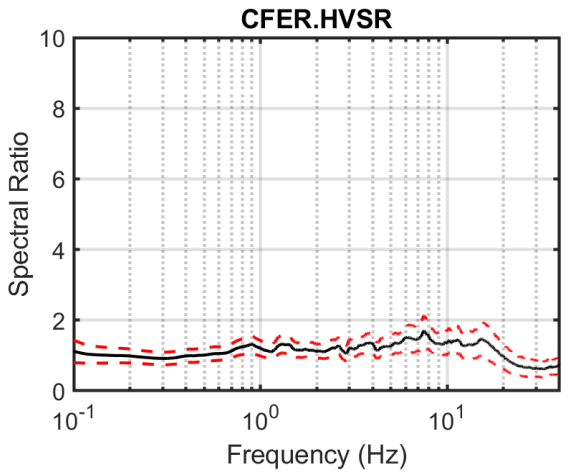
Power	4 solar panels 36W
UMTS coverage	-101dB
Sensor	T4A87/D
Datalogger	DCM-674
Installation date	27/06/2019
Removal date	18/05/2021
	
	 HHZ

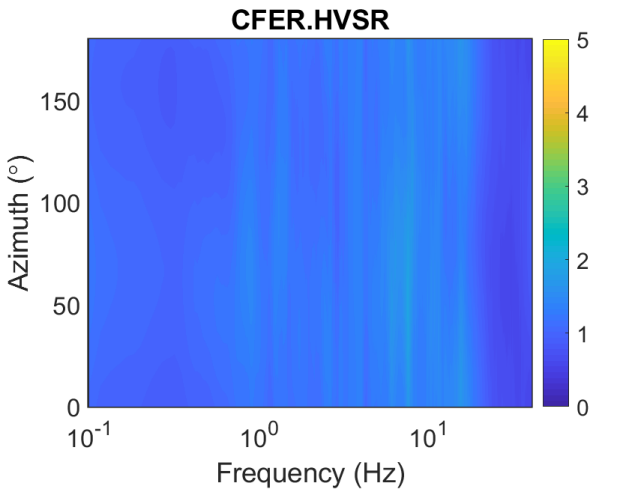


HHE

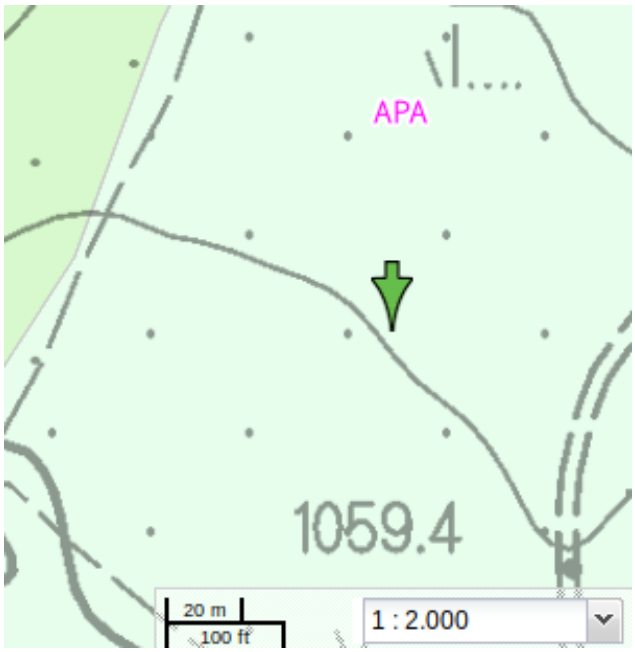


HHN

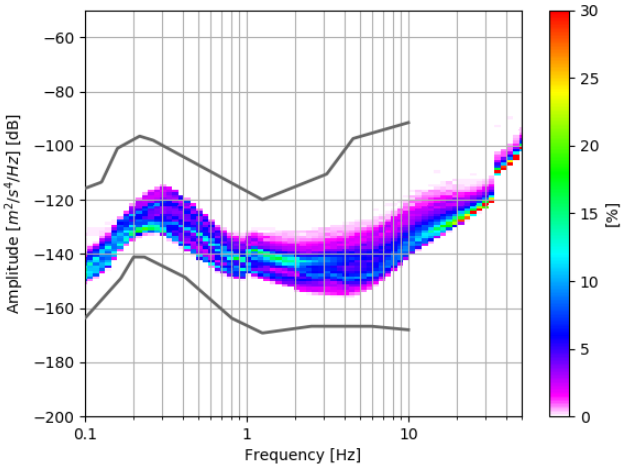




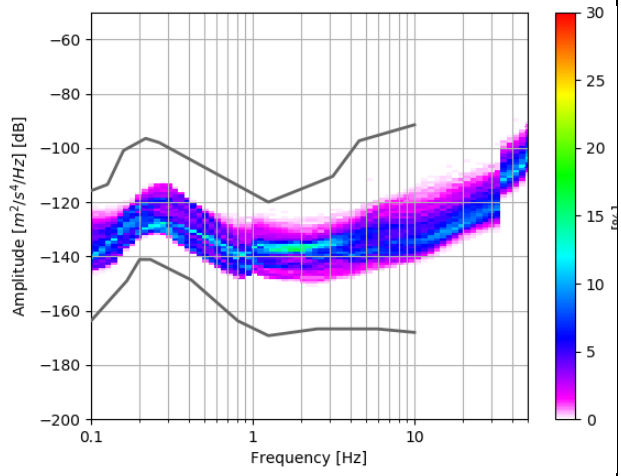
Station ID	**MBEN**
Municipality	Firenzuola
Local Area	Monte Beni
Latitude (° WGS84)	44.14831
Longitude (° WGS84)	11.3107
Altitude (m.s.l.m)	1061
Geology	APA (Argille a Palombini)
Soil	Argilliti grigie e calcilutiti

Power	4 solar panels 36W
UMTS coverage	-103dB
Sensor	T4A97/D0513
Datalogger	DCM-858
Installation date	03/07/2019
Removal date	17/05/2021
	

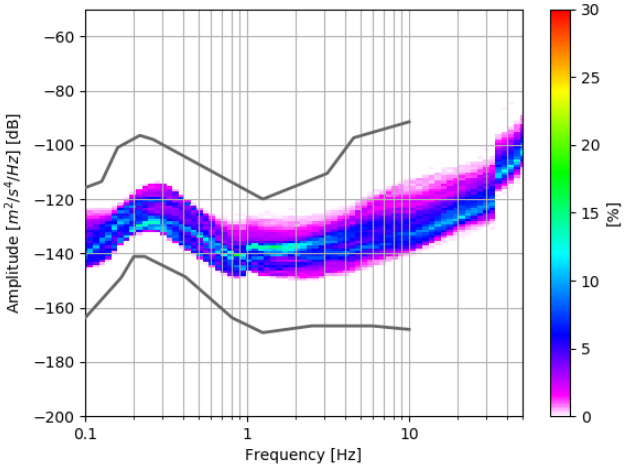



Amplitude [$m^2/s^4/Hz$] [dB]
−60
−80
−100
−120
−140
−160
−180
−200
0.1
1
10
Frequency [Hz]
30
25
20
15
10
5
0
[%]

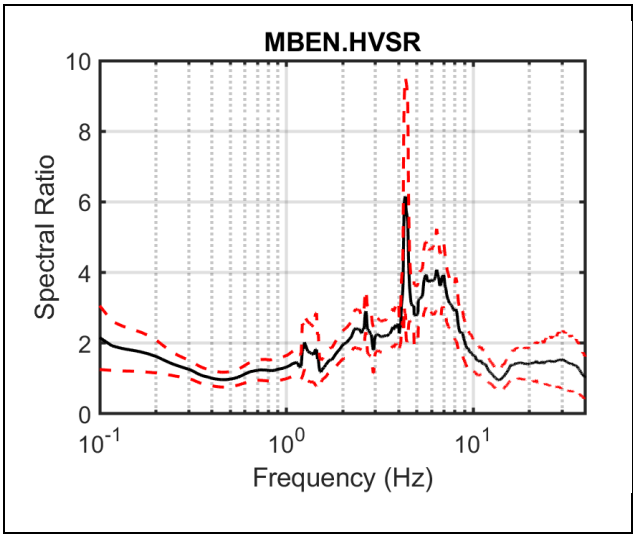
HHZ

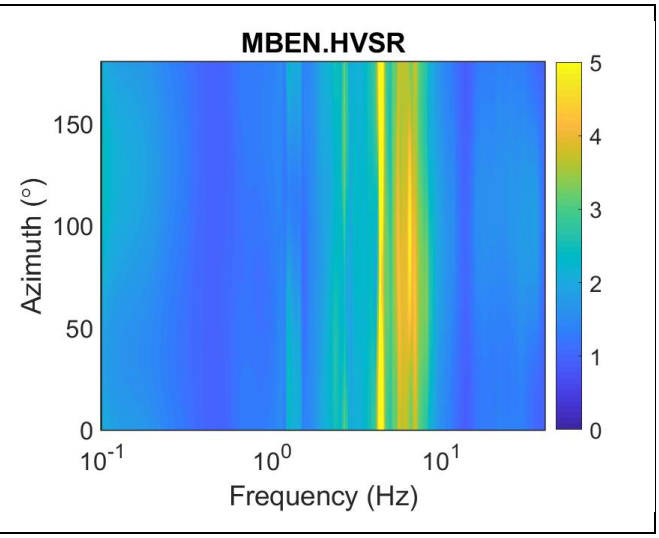

Amplitude [$m^2/s^4/Hz$] [dB]
−60
−80
−100
−120
−140
−160
−180
−200
0.1
1
10
Frequency [Hz]
30
25
20
15
10
5
0

HHE


Amplitude [$m^2/s^4/Hz$] [dB]
−60
−80
−100
−120
−140
−160
−180
−200
0.1
1
10
Frequency [Hz]
30
25
20
15
10
5
0
[%]

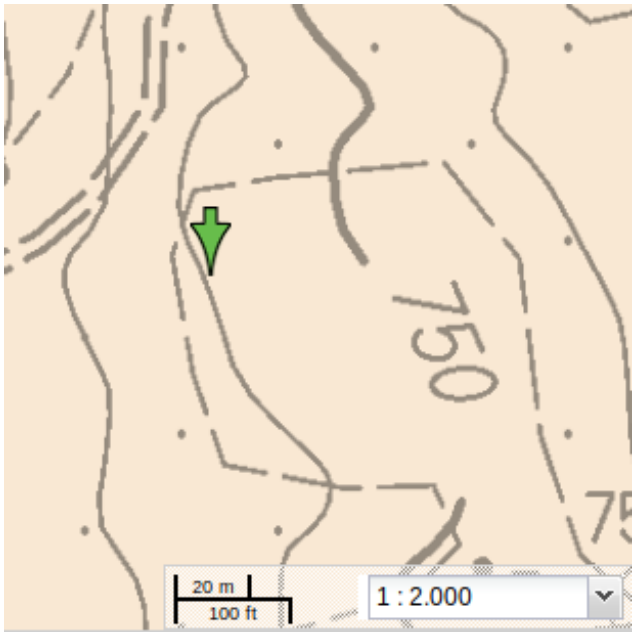
HHN



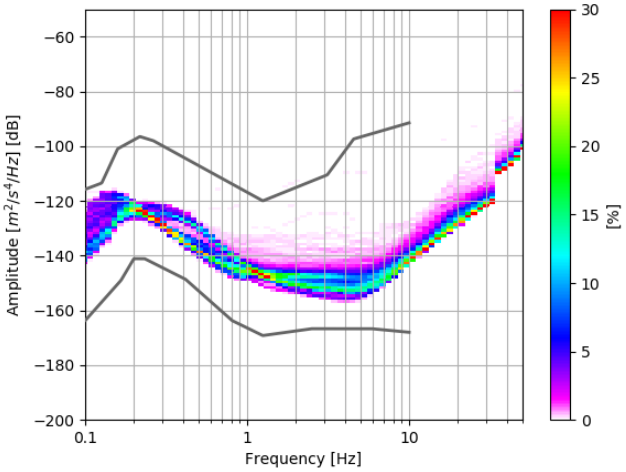


Station ID	**CASC**
Municipality	Palazzuolo sul Senio
Local Area	Ca'di Scheta, Località Lozzole
Latitude (° WGS84)	44.08059
Longitude (° WGS84)	11.53222
Altitude (m.s.l.m)	740
Geology	FM4A (Membro di Galeata)
Soil	Formazione marnoso-arenacea
Power	4 solar panels 36W
UMTS coverage	-94dB
Sensor	T4A84/D0493
Datalogger	EAM-2105
Installation date	04/07/2019
Removal date	20/05/2021

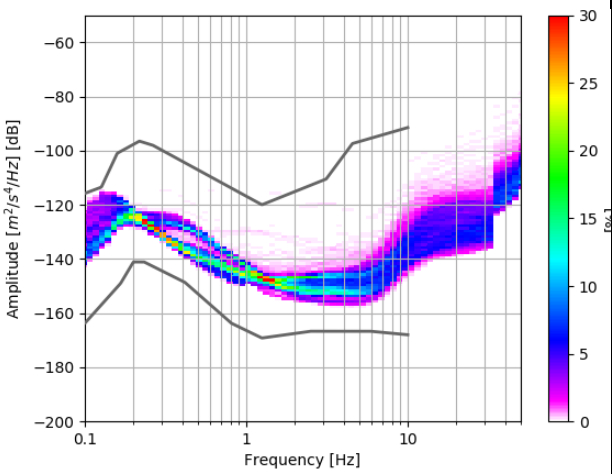

20 m
100 ft
1 : 2.000


750
20 m
100 ft
1 : 2.000

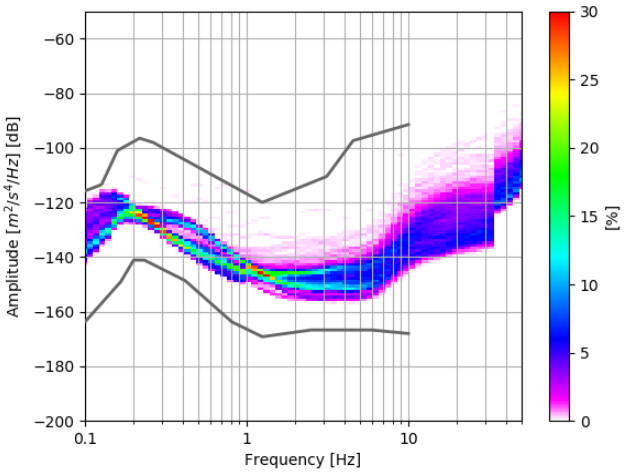



Amplitude [m²/s⁴/Hz] [dB]
Frequency [Hz]
[%]

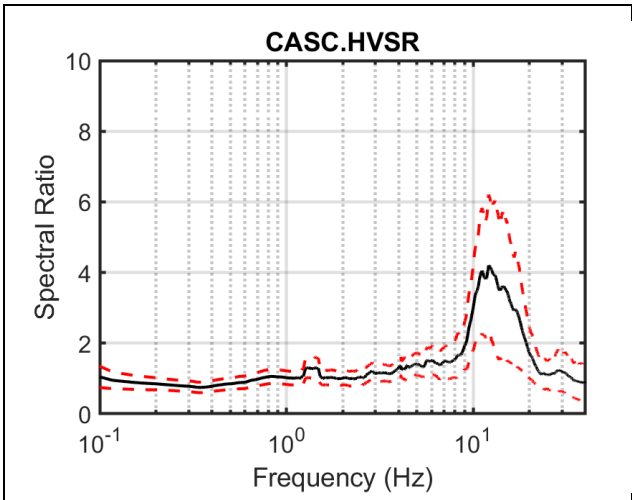
HHZ

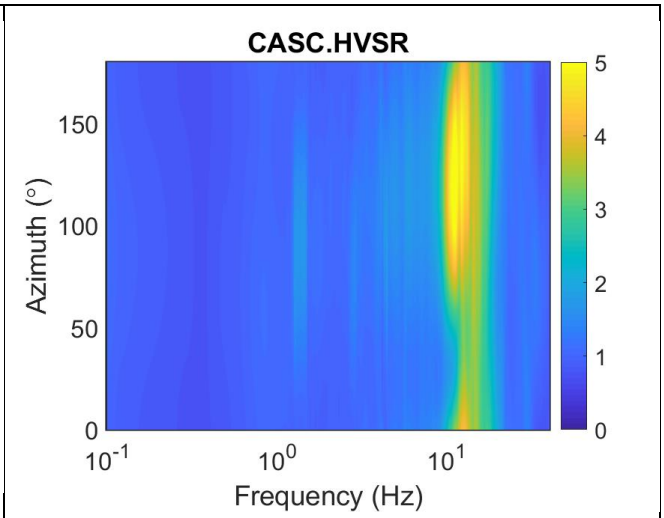

Amplitude [m²/s⁴/Hz] [dB]
Frequency [Hz]

HHE


Amplitude [m²/s⁴/Hz] [dB]
Frequency [Hz]
[%]

HHN



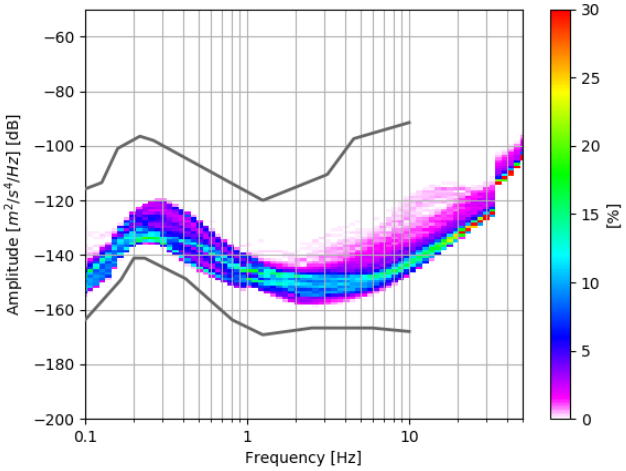


Station ID	**RINC**
Municipality	Londa
Local Area	Rincine
Latitude (° WGS84)	43.88647
Longitude (° WGS84)	11.60699
Altitude (m.s.l.m)	955
Geology	FAL3 (Membro di Montalto: membro arenaceo pelitico)
Soil	Arenarie di Monte Falterona
Power	8 solar panels 36W
UMTS coverage	-99dB
Sensor	T4A93/D0492
Datalogger	DCM-938
Installation date	10/07/2019
Removal date	

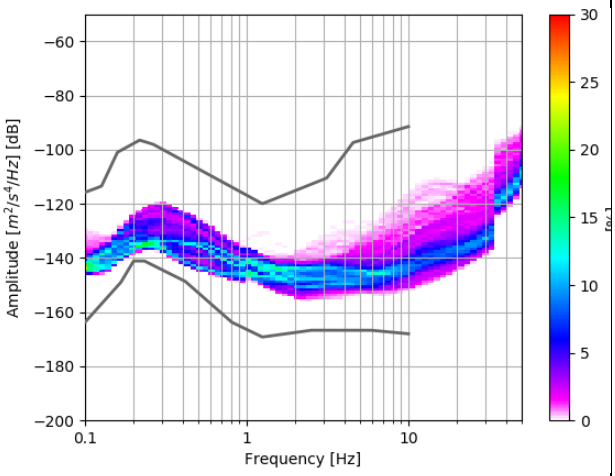

20 m
100 ft
1 : 2.000


20 m
100 ft
1 : 2.000

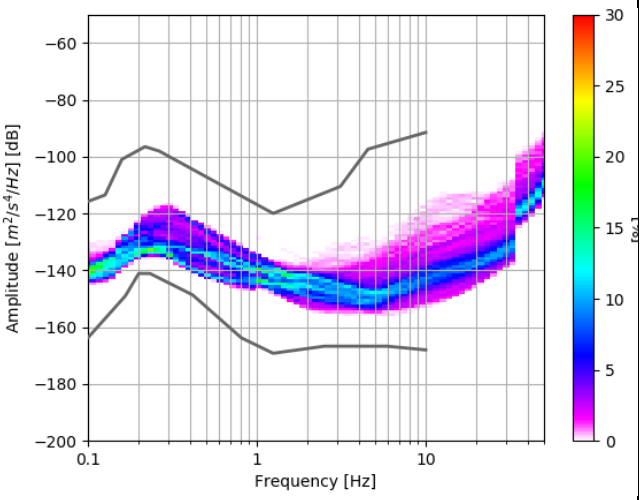



Amplitude [m²/s⁴/Hz] [dB]
Frequency [Hz]
[%]

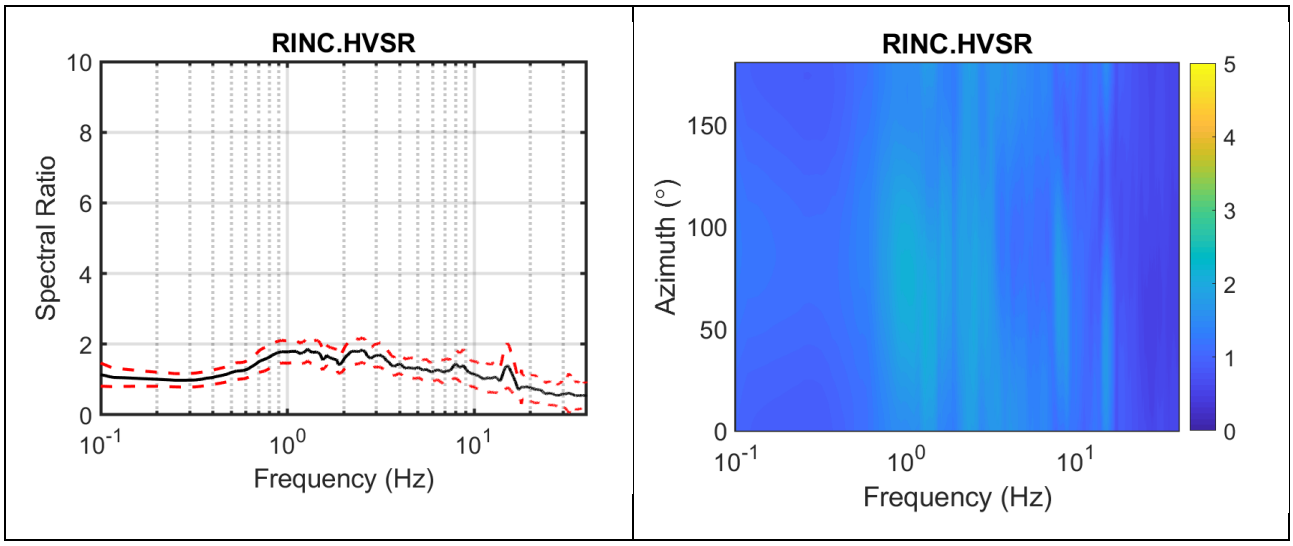
HHZ


Amplitude [m²/s⁴/Hz] [dB]
Frequency [Hz]

HHE


Amplitude [m²/s⁴/Hz] [dB]
Frequency [Hz]

HHN


RINC.HVSR
Spectral Ratio
Frequency (Hz)
RINC.HVSR
Azimuth (°)
Frequency (Hz)

2. Space-Time evolution of the sequences

Figures S1(a, b, c, d) and S2 represent, for each sequence, the temporal evolution of (a) hypocentral coordinates, (b) the distance from the first earthquake of the sequence, and (c) Vp/Vs ratio. A weak expansion of the aftershock volume is only observed for the 2019 sequence and for the early stages of the 2008 one, while both the 2009 and 2015 sequences do not depict any such behaviour. The progessive expansion of the faulting front may be interpreted in terms of a diffusive process, where fault failure is favoured by a migrating pore pressure front (e.g., Shapiro et al., 1997). Under that hypothesis, a first approximation to the description of the spatial and temporal distribution of the seismicity is given by the diffusion equation:

$r = (4 \pi \alpha t)^{0.5}$

where α is the diffusivity and r is the distance reached by the triggering front at time t. The time-distance plots in Figure S2 suggest a velocity of the triggering front up to 4000m day^{-1}, which implies a diffusivity α as high as 15 $m^2 s^{-1}$, well outside 0.1-10 $m^2 s^{-1}$ range indicated by Talwani and Acree (1985) for hydraulic diffusivity in the upper crust. A further element playing against the possible role of fluids into the seismogenic process, consists in the observation that all the analyzed sequences share very similar behaviours: the mainshock occurs at the very early stage of the sequence, and the following aftershocks closely abide Omori's law (Figure S2a). Finally, the Vp/Vs ratio does not exhibit any evident trend throughout individual sequences (Figure S1), even though its overall estimate is different between sequences: for the 2008 and the 2019 episodes it is around 1.84, whereas for the 2009 and 2015 ones it is around 1.73 and 1.70, respectively (Figure S3).

In conclusion, the above observations suggest that all the analyzed sequences have most likely been driven by a 'classical' mechanism associated with a cascade of elastic stress triggering, rather than with the diffusion of a pore pressure front (e.g., Vidale and Shearer, 2006).

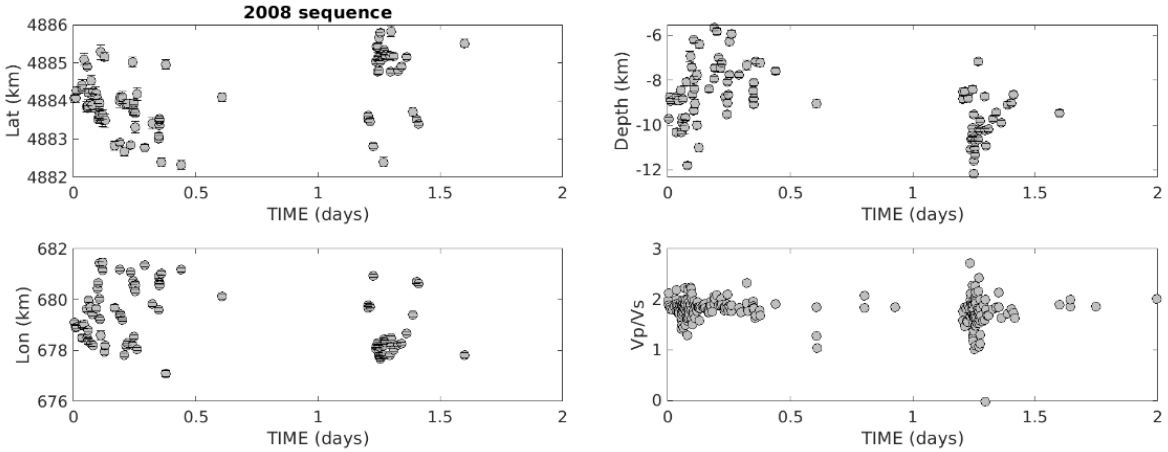


Figure S1a: Temporal evolution of hypocentral coordinates and of Vp/Vs ratio for the 2008 sequence.

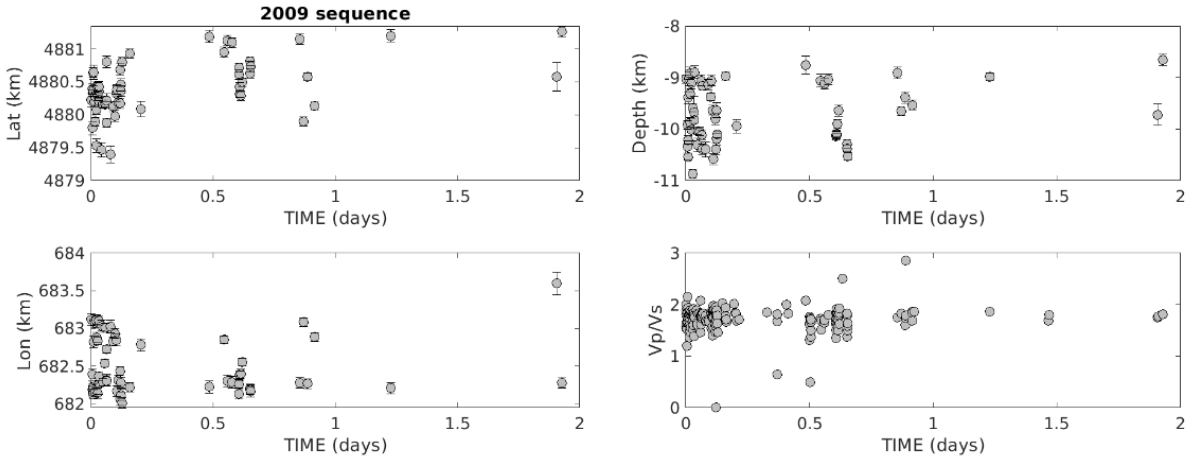


Figure S1b: Temporal evolution of hypocentral coordinates and of Vp/Vs ratio for the 2009 sequence.

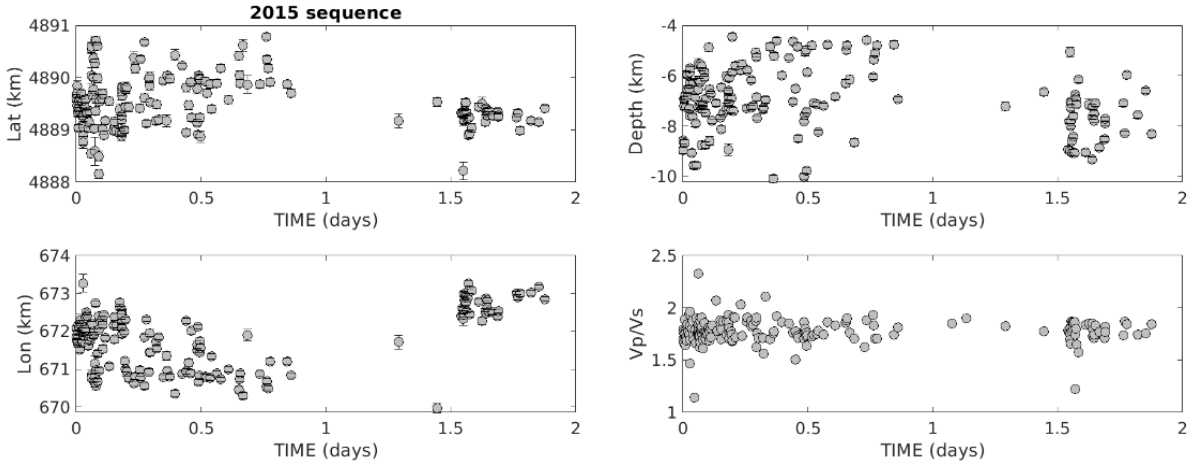


Figure S1c: Temporal evolution of hypocentral coordinates and of Vp/Vs ratio for the 2015 sequence.

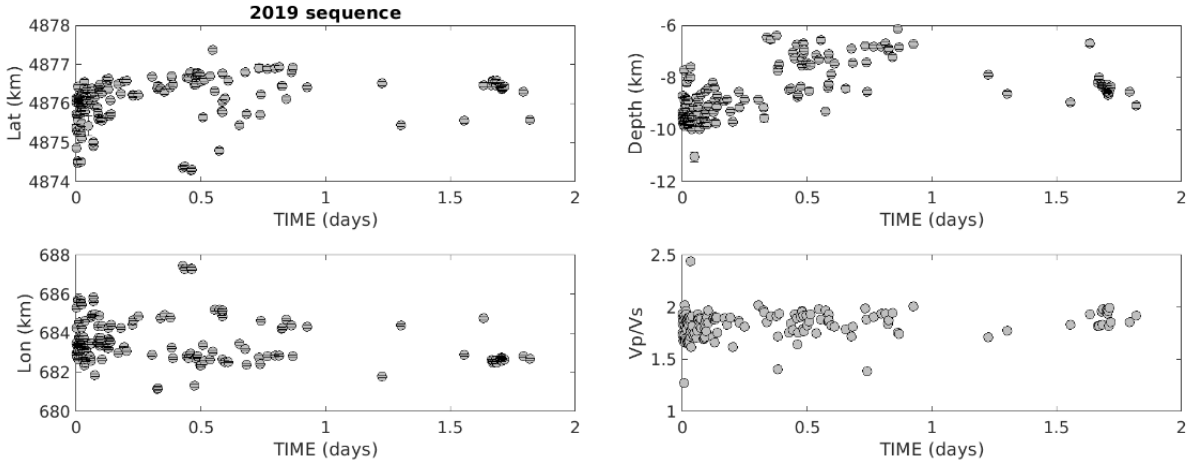


Figure S1d: Temporal evolution of hypocentral coordinates and of Vp/Vs ratio for the 2019 sequence.

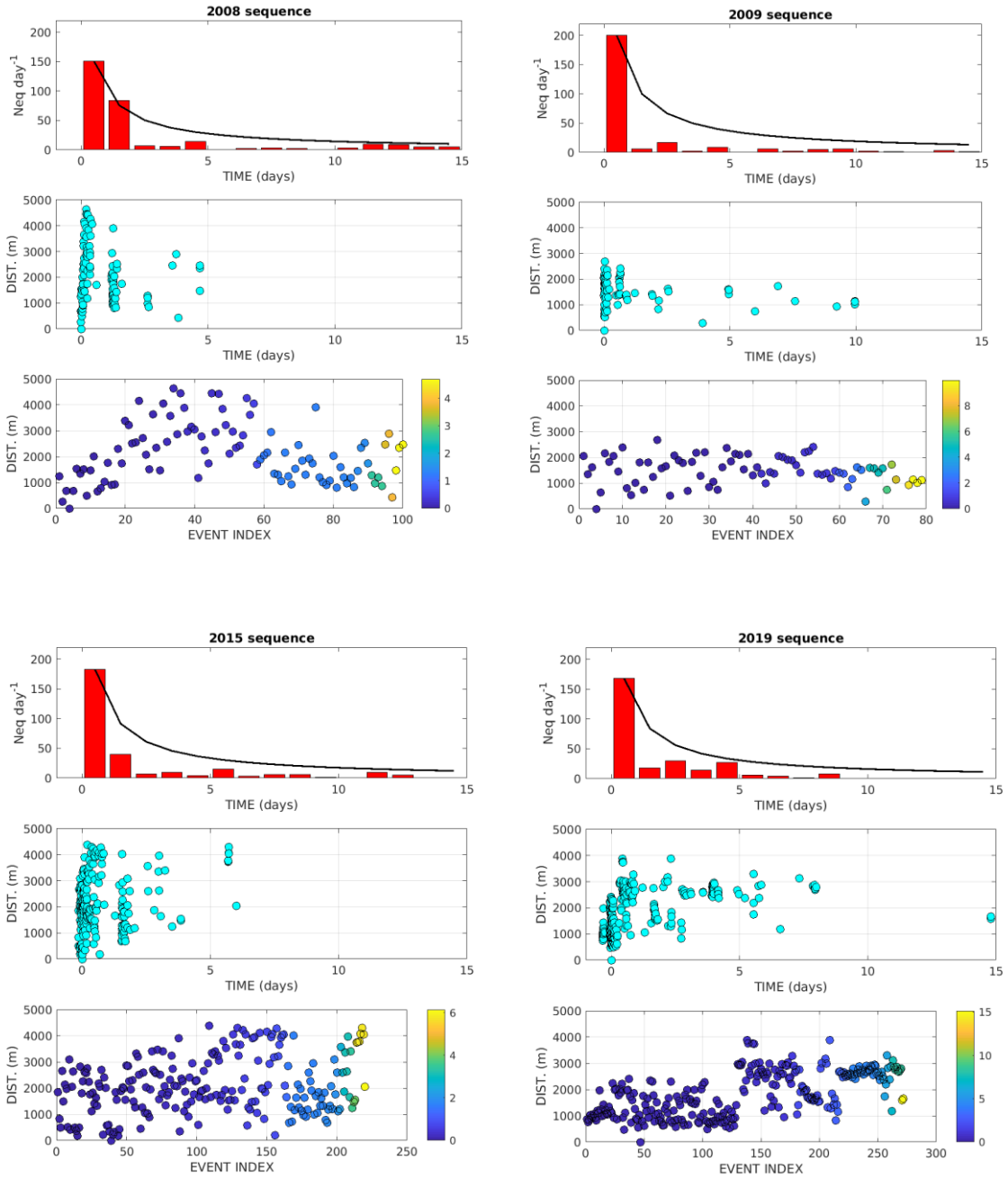


Figure S2: For each sequence, on the top panels the daily occurrence rate of earthquakes compared with the Omori's law (black line); in the middle, the temporal evolution of the distances of the events from the first earthquake of the sequence; on the bottom panels, the same as in the middle but in respect to the event index.

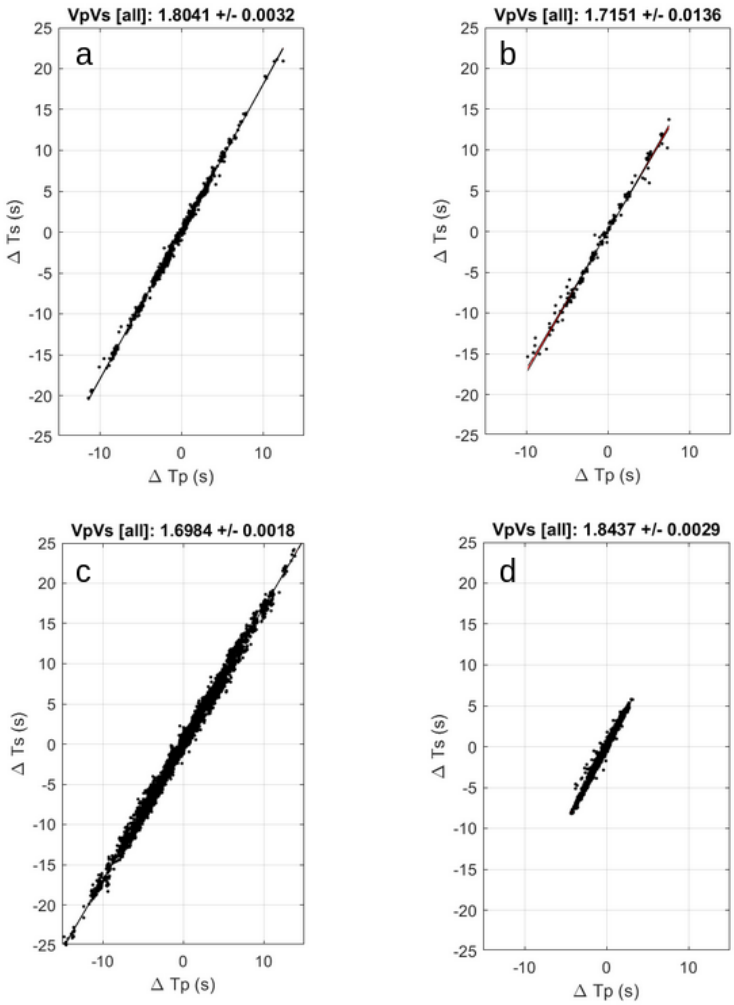


Figure S3: The resulting Vp/Vs ratio from the modified Wadati diagram, for each sequence a) 2008, b) 2009, c) 2015, d) 2019.